

The Sr-isotopic stratigraphy of the Eastern Limb of the Bushveld Complex.

By

Thapelo Sidwell Motaung

Dissertation submitted in accordance with the requirements for the degree:

Master of Science

In

Geology

Faculty of Natural and Agricultural Sciences

University of the Free State

Bloemfontein, South Africa

UNIVERSITY OF THE
FREE STATE
UNIVERSITEIT VAN DIE
VRYSTAAT
YUNIVESITHI YA
FREISTATA



UFS·UV
NATURAL AND
AGRICULTURAL SCIENCES
NATUUR- EN
LANDBOUWETENSKAPPE
GEOLOGY
GEOLOGIE

Declaration

I, Thapelo Sidwell Motaung, declare that this dissertation, hereby submitted in fulfilment for the qualification of Master of Science degree in Geology, in the faculty of Natural and Agricultural Sciences, Department of Geology, University of the Free State, is my own unaided work. It has not been submitted for any other University or tertiary institution's degree or examination. I also declare that all sources that are cited or quoted are indicated and acknowledged in the list of references. I further relinquish copyright of the dissertation in favour of the University of the Free State.

A handwritten signature in black ink, appearing to read "Thapelo Sidwell Motaung". The signature is written in a cursive style with some variations in letter height and stroke thickness.

Thapelo Sidwell Motaung

Signed on: Thursday, 26 October 2021

Dedication

To my mother Mamodibedi Annah Motaung and my aunt Maseaka Sarah Mokoena.
Also dedicated to my late grandparents from my maternal side (Tebejane Tsoke and
Madisebo Motaung), stepfather Nelson Ramovha and the entire Motaung family.

Acknowledgements

Firstly, I would like to thank Professor Frederick Roelofse and Ms Justine Magson for nominating me to take on this project. This dissertation would not have been possible without them, so I hereby thank and acknowledge their contributions towards the understanding and completion of the dissertation. Their guidance and care throughout the duration of this dissertation is also acknowledged.

The assistance offered by Luvuyo Ngubeni, Thembane Mangange, Mafete Malatji and Teboho Mohapeloa at the core shed situated on the premises of the University of the Free State is also thanked. They helped with unloading and loading of the core boxes during the sampling stage of this project. Mr Radikgomo is also thanked for the preparation of thin sections while Mr Pelele Lehloenya is also thanked for the preparation of fusion discs and his advice throughout the dissertation as per my consultations with him.

Ms Megan Purchase is also thanked for helping with XRF analysis at the University of the Free State. Gratitude is extended to Ms Diana Faseka for organizing accommodation for me at the University of Johannesburg during my two visits for Electron Microprobe and in-situ strontium analysis. Dr Christian Reinke is also appreciated for his help and advice with the Cameca SX-100 Microprobe, and for carbon coating at the University of Johannesburg. Ms Henriette Ueckermann is also thanked for her help and guidance during the use of the Nu Plasma II MC-ICPMS linked with 193 nm ArF RESOlution SE excimer laser housed at University of Johannesburg's Spectrum Analytical Facility.

The support of the Department of Science and Innovation through its funding agency, the National Research Foundation, and the Centre of Excellence for Integrated Mineral and Energy Resource Analysis (DSI-NRF CIMERA) towards this research is hereby acknowledged.

I would like to thank Katileho Tladi and Lindubuhle Mngomezulu for offering their laptops during the time my laptop had crashed. I would also like to thank my mother Mamodibedi Motaung and my aunt Maseaka Mokoena for their continued support throughout the duration of my dissertation. I also acknowledge my entire family for their love, care and support. My friends, Dimakatso Mokoena, Velapi Zwane, Busisiwe Mbongo, Lungile Skhosana, Mamonare Mohapi, Thabang Sekhoto and

Thoriso Lekoetje are also acknowledged for their support. Opinions expressed and conclusions arrived at, are those of the author(s) and are not necessarily to be attributed to the CoE, DSI or NRF.

Abstract

Data on the modal mineralogy, whole-rock geochemistry, mineral chemistry and Sr-isotopic compositions of plagioclase from the broadly pyroxenitic Lower Critical Zone to the gabbroic Upper Zone in the Eastern Limb of the Bushveld Complex are presented in this study, covering a stratigraphic interval of approximately 5000 m. The data were determined using transmitted light microscopy, X-Ray Fluorescence Spectrometry (XRF), Electron Probe Micro-Analyzer (EPMA) and Laser Ablation Multi-Collector Inductively Coupled Plasma Mass Spectrometry (LA-MC-ICPMS) to produce a continuous and relatively high-resolution profile of variations in mineral chemistry, whole-rock major and trace elements and Sr-isotopic composition of plagioclase.

The results show Sr-isotopic trends that are similar to those observed in the Western Limb, with the first isotopically heterogeneous stage named the “Integration Stage”, characterised by fluctuating initial $^{87}\text{Sr}/^{86}\text{Sr}$ compositions from the Lower Critical Zone (~0.7051) to the Lower Main Zone (~0.7084). These variations are attributed to repeated influxes of compositionally distinct magmas. The Lower / Upper Critical Zone boundary is characterized by a sharp increase in initial $^{87}\text{Sr}/^{86}\text{Sr}$ ratios from 0.7054 to 0.7062 while the Critical Zone / Main Zone boundary is characterized by a sharp increase from 0.7065 to 0.7080.

The isotopically homogeneous “Differentiation Stage” includes the Upper Main and Upper zones. This interval is characterized by relatively uniform initial $^{87}\text{Sr}/^{86}\text{Sr}$ composition of ~0.7073. Limited variation in Sr-isotopic compositions suggests that this stratigraphic interval was formed through fractional crystallization with limited or no injections of new magma. The last major addition of magma into the Bushveld magma chamber is recorded by fluctuations in plagioclase An% and initial $^{87}\text{Sr}/^{86}\text{Sr}$ ratios at the level of the Pyroxenite Marker, which occurs at the boundary between the Lower and Upper Main zones. There is a decrease in initial $^{87}\text{Sr}/^{86}\text{Sr}$ ratios at the level of the Pyroxenite Marker, from 0.7079 to 0.7075.

Within the “Integration Stage” where significant variations in initial $^{87}\text{Sr}/^{86}\text{Sr}$ ratios of plagioclase are recorded, there is limited variation in plagioclase An% compared to the “Differentiation Stage”, which is characterized by a dominantly normal differentiation trend shown by decreasing plagioclase An% with increasing

stratigraphic height and limited variation in initial $^{87}\text{Sr}/^{86}\text{Sr}$ ratios of plagioclase. This trend between plagioclase An% and initial $^{87}\text{Sr}/^{86}\text{Sr}$ ratios of plagioclase is also observed in the Western and Northern Limbs of the Bushveld Complex.

Inter and intra-crystal initial $^{87}\text{Sr}/^{86}\text{Sr}$ disequilibrium is locally observed in the Lower Main and Upper Critical zones and is limited in the Upper Main and Upper Zones. This disequilibrium supports a model of petrogenesis which suggests that the Critical and Lower Main Zones formed through intrusion of variably contaminated crystal mushes derived from a sub-compartmentalized, sub-Bushveld staging chamber that underwent different degrees of contamination with crustal rocks of the Kaapvaal craton. The Upper Main and Upper Zones revealed uniform initial $^{87}\text{Sr}/^{86}\text{Sr}$ compositions with a decreasing plagioclase An% trend, suggesting normal fractionation as the main petrogenetic process.

Table of Contents

Declaration	i
Dedication	ii
Acknowledgements	iii
Abstract	v
List of Figures.....	ix
List of Tables	xiii
1. INTRODUCTION.....	1
1.2 Geological overview and stratigraphy of the Bushveld Complex.....	2
1.2.1 Geological setting of the Bushveld Complex.....	2
1.2.2 The Rustenburg Layered Suite (RLS).....	4
1.2.3 Lithostratigraphic units of the Rustenburg Layered Suite	6
1.3 Previous isotopic work on the Bushveld Complex.....	9
1.4 Some topics of continued debate	12
1.5 Purpose of the study	13
2. Methodology.....	14
2.1 Sampling	14
2.2 Petrography	16
2.3 Whole-rock major and trace element geochemistry	18
2.4 Mineral chemistry	19
2.5 Strontium-isotopic determinations.....	22
3. RESULTS.....	24
3.1 Petrography	24
3.1.1 Macroscopic descriptions.....	24
3.1.1.3 Pyroxenite Marker sample	26
3.1.2 Microscopic descriptions.....	31
3.2 Whole-rock major and trace element geochemistry	40

3.2.1 Whole-rock major element geochemistry	40
3.2.2 Whole-rock trace element geochemistry.....	50
3.3 Plagioclase mineral chemistry.....	63
3.4 Sr-isotopic compositions of plagioclase	69
4. DISCUSSION	78
4.1 Variations in whole-rock geochemistry and plagioclase mineral chemistry....	78
4.2 Variations in the Sr-isotopic composition of plagioclase	79
4.3 Comparison of the Sr-isotopic stratigraphy of the Eastern Limb with the Western Limb.....	82
4.4 A petrogenetic model for the Eastern Limb of the Bushveld Complex	84
5. Summary.....	85
6. Conclusion	87
7. References.....	89
8. Appendices	96
Appendix A1: Whole-rock major element data in weight% of samples from the LCZ to the UZ, with LOI and Mg#..	96
Appendix A2: Whole-rock trace element data in ppm of samples covering the LCZ to the UZ	100
Appendix B: The major element composition of plagioclase per analysed spot in weight %, including the calculated anorthite content (An%) of plagioclase.....	103
Appendix C: The Sr-isotopic composition of plagioclase per analysed point, with depths reported in metres (m) from the Lower Critical Zone to the Upper Zone.	120

List of Figures

Figure 1: Overview of the Bushveld Complex (modified after Grobler et al., 2019)	2
Figure 2: General geology of the Eastern Limb of the Bushveld Complex (modified after Cameron & Abendroth, 1957), showing the positions of the boreholes forming the focus of this study.....	5
Figure 3: Stratigraphic and isotopic summary showing the mineralogical variation, Sr-isotopic variations, and the location of major unconformities of the RLS (Kruger, 2005).	6
Figure 4: Photograph showing the 58 samples collected for this study. Sample positions are shown in Figure 5.....	15
Figure 5: Schematic representation of the four studied boreholes.	16
Figure 6: Photograph showing the thin sections prepared from samples collected for this study.	17
Figure 7: The Olympus BX51 petrographic microscope used for the petrographic examination of samples for this study.	18
Figure 8: The Cameca SX-100 Microprobe, equipped with four wavelength dispersive spectrometers at the University of Johannesburg.	20
Figure 9: A selection of backscattered electron (BSE) images showing selected unaltered plagioclase crystals that were analysed by EPMA, including the positions of spots analysed.	21
Figure 10: The Nu Plasma II MC-ICPMS linked with 193 nm ArF RESOlution SE excimer laser housed at the Spectrum Analytical Facility of the University of Johannesburg.	23
Figure 11: Photographs of selection of samples from the UZ: A) Magnetite gabbronorite; B) Magnetite gabbro; C) Gabbro; D) Gabbronorite with a magnetitite layer; E) Olivine gabbronorite.....	25
Figure 12: Photographs of selection of samples from the UMZ: A) Gabbronorite; B) Gabbro; C) Anorthosite.	26

Figure 13: Photograph showing the sample taken from the Pyroxenite Marker 27

Figure 14: Photographs of selection of samples from the LMZ: A) Gabbronorite; B) Gabbro; C) Spotted anorthosite 28

Figure 15: Photographs of selection of samples from the UCZ: A) Anorthosite; B) Gabbronorite; C) UG3 chromitite with underlying anorthosite; D) Norite; E) Pyroxenite 30

Figure 16: Photographs of selection of samples from the LCZ: A) LG5 and LG6 chromitites; B) Pyroxenite 31

Figure 17: Cross-polarized transmitted light photomicrographs of: (A) Plagioclase crystals aligned in a parallel to sub-parallel orientation in gabbronorite, defining igneous layering that has been observed in most studied samples. Sample is from depth of 711.43 m; (B) Bent and wedge-shaped twin lamellae in the plagioclase of the olivine gabbronorite from a depth of 1 104.46 m; (C) Plagioclase in magnetite gabbronorite that has been altered along the rims and within the crystal, to sericite, from depth of 812.53 m; (D) Magnetite enclosed by biotite in the magnetite gabbronorite from depth 911.78 m, with biotite altered to chlorite; (E) Intercumulus plagioclase, olivine and clinopyroxene in the magnetite gabbronorite from depth of 418.31 m; (F) Inverted pigeonite surrounded by magnetite and biotite in the magnetite gabbronorite from depth 911.78 m 34

Figure 18: Cross-polarized transmitted light photomicrographs of: (A) Orthopyroxene crystal enclosing lath-shaped plagioclase crystals, exhibiting subophitic texture contained in the gabbro from depth of 1 447.51 m; (B) Intergranular texture shown by cumulus plagioclase and clinopyroxene of the gabbronorite from the depth of 1 616.47 m; (C) Polysynthetic twinned plagioclase with intergranular orthopyroxene and clinopyroxene in the gabbronorite from the depth of 1 695.81 m; (D) Inverted pigeonite and plagioclase contained in the gabbro from the depth of 1 349.35 m; (E) Unusual olivine encountered in the gabbro from the UMZ at 1 447.51 m; (F) Clinopyroxene twinning contained in the gabbro from the depth of 1 349.35 m in the UMZ 35

Figure 19: Cross-polarized transmitted light photomicrographs of: (A) Clinopyroxene, orthopyroxene and olivine crystals in the pyroxenite at the level of the Pyroxenite Marker; (B) Plagioclase, orthopyroxene and inverted pigeonite crystals observed in the pyroxenite at the level of the Pyroxenite Marker; (C) Clinopyroxene, inverted pigeonite crystals and a plagioclase crystal showing pinch and swell texture in the gabbronorite at 2 076.38 m; (D) Clinopyroxene crystals of the gabbronorite from the depth of 1 978.02 m exhibiting twinning; (E) Orthopyroxene and plagioclase crystals showing ophitic texture in the gabbronorite from the depth of 3 525.27 m; (F)

Orthopyroxene oikocryst enclosing clinopyroxene and plagioclase chadacrysts in the gabbronorite from the depth of 1 782.05 m 36

Figure 20: Cross-polarized transmitted light photomicrographs of: (A) Dominant pyroxene with interstitial plagioclase and clinopyroxene showing intergranular texture in the pyroxenite from the depth of 4 654.76 m in the UCZ; (B) Orthopyroxene and lath-shaped plagioclase crystals exhibiting ophitic texture in the gabbronorite at the depth of 3 972.90 m in the UCZ; (C) Massive texture shown by the dominant mineral chromite with traces of plagioclase and clinopyroxene in the UG3 chromitite; (D) Poikilitic texture shown by clinopyroxene enclosing orthopyroxene crystals in the pyroxenite at the depth of 4 991.09 m in the LCZ 37

Figure 21: Variations in modal mineralogical composition with depth. Plagioclase, orthopyroxene and clinopyroxene are the dominant minerals in the stratigraphic profile. Magnetite and olivine occur mostly in the sampled UZ, while inverted pigeonite occurs mostly in the sampled LMZ. Quartz and biotite occur as minor minerals throughout the stratigraphic profile. Chromite is confined to the sampled CZ, where it locally forms chromitites..... 39

Figure 22: Binary variation diagrams of selected whole-rock major elements versus MgO. 41

Figure 23: Variation of whole-rock major elements with depth across the studied interval..... 45

Figure 24: Variation of whole-rock Mg# with depth compared to variations in the modal mineralogical composition. 49

Figure 25: Binary variation diagrams of selected whole-rock trace elements vs. MgO. 53

Figure 26: Variation in whole-rock trace elements with depth, compared with modal mineralogical variations. 58

Figure 27: Plagioclase compositions encountered in this study presented in the feldspar ternary diagram. 63

Figure 28: Variation of plagioclase anorthite content (An%) with depth compared to variations in the modal mineralogical composition. 65

Figure 29: The average An content (An%) of samples versus depth, with error bars representing standard deviation, and a modal mineralogy graph showing varying mineral components in the samples..... 68

Figure 30: The initial $^{87}\text{Sr}/^{86}\text{Sr}$ composition of analysed spots plotted against depth, with modal mineralogy graph showing varying mineral compositions of samples throughout the stratigraphy. Different colours show coexisting plagioclase in a single sample. Circles represent analysed core domains while triangles represent rims. Error bars represent 2SE. 70

Figure 31: The variation in the average initial $^{87}\text{Sr}/^{86}\text{Sr}$ compositions of plagioclase with depth, compared to the variation in modal mineralogical composition. Error bars indicate 2 standard deviations..... 77

Figure 32: Comparison of variations in initial $^{87}\text{Sr}/^{86}\text{Sr}$ compositions and anorthite (An%) content of plagioclase across the stratigraphy: (A) Karykowski et al. (2017) and (B) this study. 81

Figure 33: Comparison of initial $^{87}\text{Sr}/^{86}\text{Sr}$ compositions of the Western Limb and the Eastern Limb from: (A) Kruger (2005) and (B) this study, respectively. 82

Figure 34: Variations in: A) Modal mineralogy; B) Whole-rock Mg#; C) Plagioclase An% and D) Plagioclase Sr_i. 86

List of Tables

Table 1: Ages of the various components of the BC. Ages were acquired from different authors: ¹Harmer & Armstrong (2000); ²Kruger (1989); ³Mapeo et al. (2004); ⁴de Waal et al. (2001), and ⁵Zeh et al. (2015). 3

Table 2: Samples showing inter- and intra-crystal initial $^{87}\text{Sr}/^{86}\text{Sr}$ variation..... 73

1. INTRODUCTION

The Bushveld Complex (BC) hosts the largest ($66\,000\text{ km}^2$) layered mafic intrusion on Earth and is situated in South Africa (McDonald & Holwell, 2011). It also hosts the world's largest deposits of Platinum Group Elements (PGEs), chromium (Cr) and vanadium (V) (Kruger, 2005). The mafic to ultramafic Rustenburg Layered Suite (RLS) is the most voluminous magmatic suite of the BC (Karykowski *et al.*, 2017) and it has received a lot of attention from researchers in the past. Past research on the BC mainly focused on mineral chemistry, formation mechanisms (Latypov *et al.*, 2018), correlating zones of mineralization (e.g. Merensky Reef and Platreef) (Yudovskaya *et al.*, 2017), and whole-rock geochemical and isotopic variations within and between stratigraphic units (Kruger & Marsh, 1982; Sharpe, 1985; Eales *et al.*, 1990; Kruger, 1990; Lee & Butcher, 1990).

The first in-situ strontium (Sr)-isotopic study on the BC was recently conducted by Chutas *et al.* (2012) using the micro-drilling technique. Several authors like Eales *et al.* (1990), Yang *et al.* (2013), Seabrook *et al.* (2005), Chutas *et al.* (2012), Roelofse & Ashwal (2012) and Roelofse *et al.* (2015) recognized the presence of Sr-isotopic disequilibrium between individual plagioclase crystals and coexisting orthopyroxene in the BC. These studies provided information about the differentiation mechanisms of the magmas responsible for the emplacement of the BC and the interaction between mantle-derived magmas and the crustal rocks they intruded prior to the formation of the BC.

This study aims to provide a continuous and relatively high-resolution profile of variations in mineral chemistry, whole-rock major and trace elements and Sr-isotopic composition of plagioclase throughout the Upper Zone (UZ) down to the Lower Critical Zone (LCZ) from four boreholes, *viz.* BH7772, BH7771, BH8172 and BH6958 drilled on the Eastern Limb of the BC. The boreholes were donated by Impala Platinum towards the International Continental Scientific Drilling Programme (ICDP) project on the BC. Apart from providing a basic dataset as a framework for future work on these drill cores, the results obtained in this study will also be used to compare the variations in the Sr-isotopic composition of the Eastern Limb with that of the Western and Northern Limbs.

1.2 Geological overview and stratigraphy of the Bushveld Complex

1.2.1 Geological setting of the Bushveld Complex

The 2055.91 Ma (Zeh *et al.*, 2015) RLS of the BC covers an area of ~66 000 km² (McDonald & Holwell, 2011) and has a thickness of about ~9 km (Kruger, 2005). It consists of five different limbs, namely the Eastern Limb, Western Limb, Far Western Limb, Northern Limb and the South-Eastern (or Bethal) Limb which is only known from borehole-core data (Kinnaird *et al.*, 2005) and which were intruded into the Transvaal Supergroup (Figure 1).

The BC consists of five major magmatic suites: the bimodal Rooiberg volcanic suite, the mafic-ultramafic RLS, a suite of mafic sills and intrusions, including the satellite intrusions of the BC; the Rashoop Granophyre Suite, and the Lebowa Granite Suite (Kruger, 2005). The ages of the suites are presented in Table 1 below.

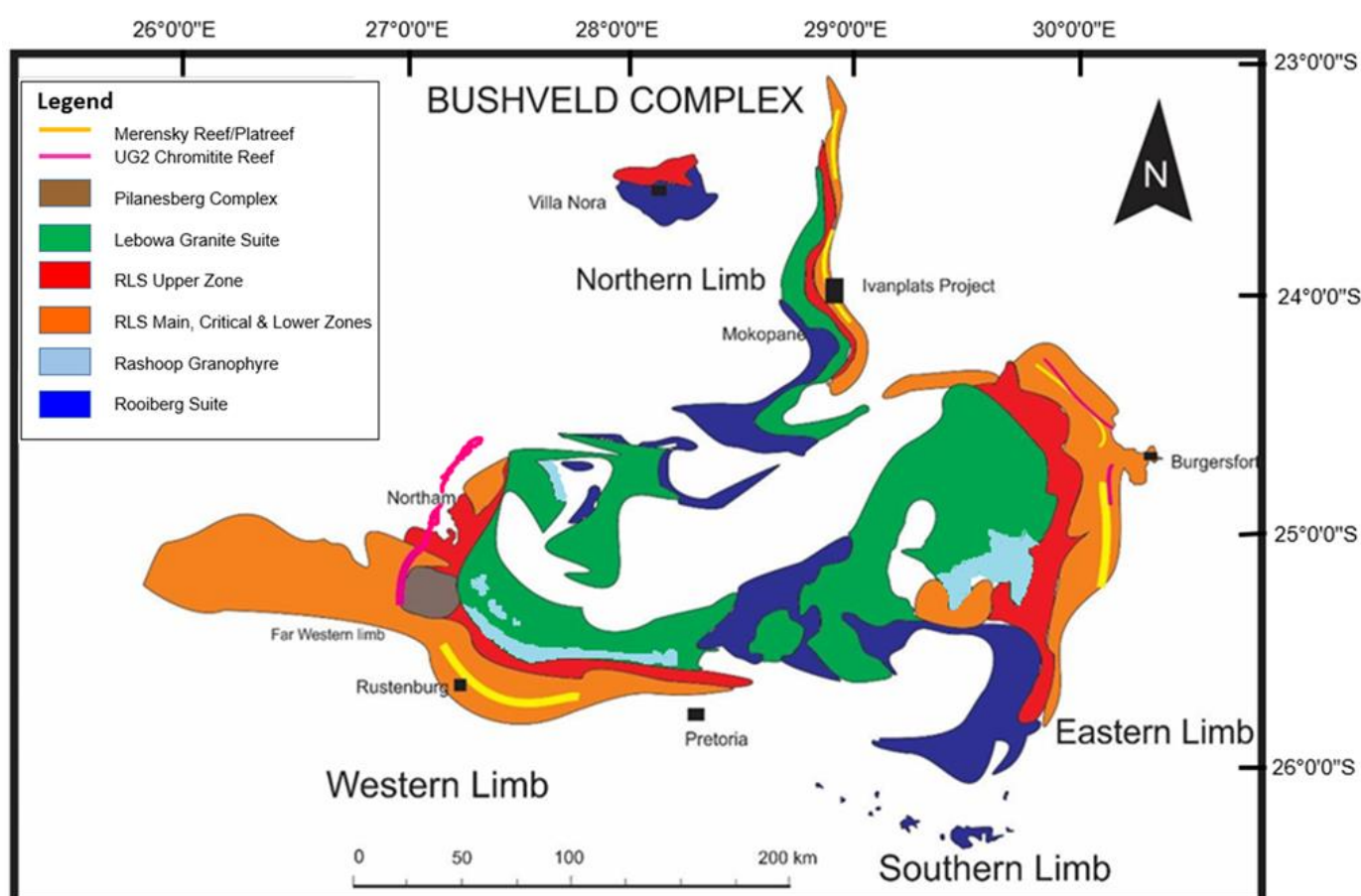


Figure 1: Overview of the Bushveld Complex (modified after Grobler *et al.*, 2019).

Table 1: Ages of the various components of the BC. Ages were acquired from different authors: ¹Harmer & Armstrong (2000); ²Kruger (1989); ³Mapeo *et al.* (2004); ⁴de Waal *et al.* (2001), and ⁵Zeh *et al.* (2015).

Lithostratigraphic unit		Age (Ma ± 95%)
Lebowa Granite Suite	Makhutso Granite Nebo Granite Steelepoort Park Granite	2053.4 ± 3.9 ¹ 2054.2 ± 2.8 ¹ 2057.5 ± 4.2 ¹
Rustenburg Layered Suite	Critical Zone (SHRIMP) Critical Zone (IDTIMS) Centre of RLS (CA-ID-TIMS)	2054.4 ± 2.8 ¹ 2054.5 ± 1.5 ¹ 2054.89 ± 0.37 ⁵
Rashoop Granophyre Suite	Rooikoppies Porphyry	2061.8 ± 5.5 ¹
Rooiberg Suite	Kwaggasnek Formation	2057.3 ± 2.8 ¹
Satellite Intrusions	Molopo Farms Mashaneng Complex Uitkomst Complex	2044 ± 24 ² 2054 ± 2 ³ 2044 ± 8 ⁴ (2055 ± 45/-17) ⁴

1.2.2 The Rustenburg Layered Suite (RLS)

As the world's largest PGE, Cr and V repository (Kruger, 2005), the RLS is composed of mafic to ultramafic layered rocks with a thickness of ~9 km (Roelofse *et al.*, 2015). The RLS is underlain by rocks of the Transvaal Supergroup (Ashwal *et al.*, 2005) and Archean granite-gneiss basement (Karykowski *et al.*, 2017). The RLS is exposed in four Limbs of the BC, the Western; Far Western; Eastern and Northern Limbs, while it is only known from borehole-core data in the Southern Limb (Eales & Cawthorn, 1996). The PGE-bearing Merensky Reef (MR), Upper Group 2 (UG-2) chromitite and Platreef are contained in the Critical Zone (CZ) of the RLS (Cameron, 1980).

The bow-shaped Western Limb is 200 km long and dips in an easterly direction. It extends from Thabazimbi in the north, to the north of Pretoria in the south (Eales & Cawthorn, 1996). The Far Western Limb extends from the west of the Pilanesberg Complex towards the border of Botswana in the west (Roelofse, 2010).

The Thabazimbi Murchison lineament separates the Northern Limb from the rest of the BC (Yudovskaya *et al.*, 2017). The Northern Limb extends over an area of about 7275 km² (van der Merwe, 1976) and is underlain by sediments of the Transvaal Supergroup in the south and by Archean granite-gneisses in the north (Yudovskaya *et al.*, 2017).

The Eastern Limb (Figure 2), which is the focus of this study, occurs as a 200 km long, bow-shaped body which dips in a westerly direction. It extends from Chuniespoort in the north to Stoffberg in the south (Roelofse, 2010).

The Southern Limb was identified based on a gravity high and is known only from borehole-core information (Eales & Cawthorn, 1996).

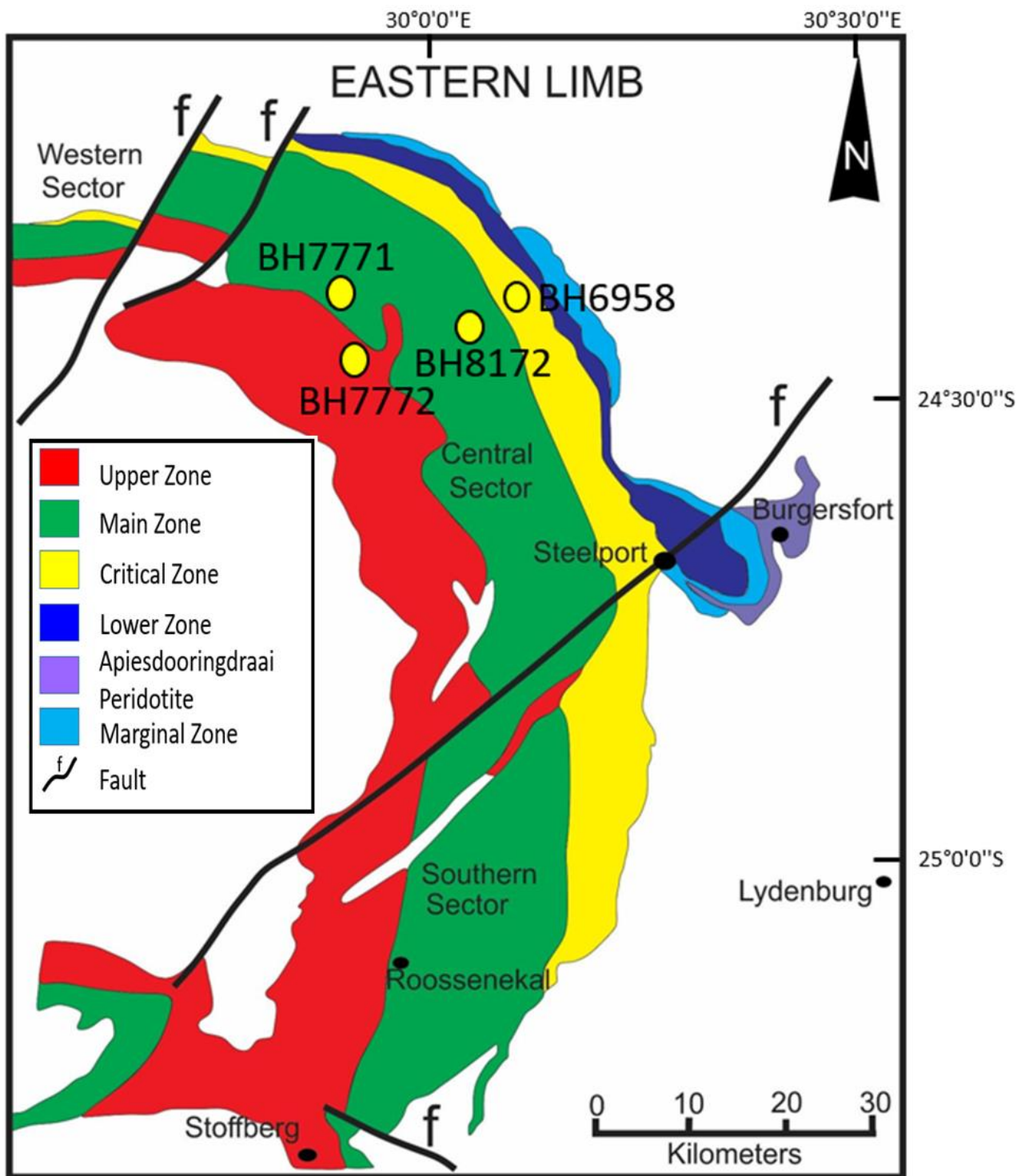


Figure 2: General geology of the Eastern Limb of the Bushveld Complex (modified after Cameron & Abendroth, 1957), showing the positions of the boreholes forming the focus of this study.

1.2.3 Lithostratigraphic units of the Rustenburg Layered Suite

The RLS is vertically subdivided into five major zones: the Marginal, Lower, Critical, Main and Upper Zones (Figure 2 & 3) (Hall, 1932). The subdivisions are based on changes in mineralogy and isotopic signatures (Karykowski *et al.*, 2017). Wilson (2011), through results from drilling and field work, discovered that the Marginal Zone is underlain by an ultramafic succession called the Basal Ultramafic Sequence (BUS).

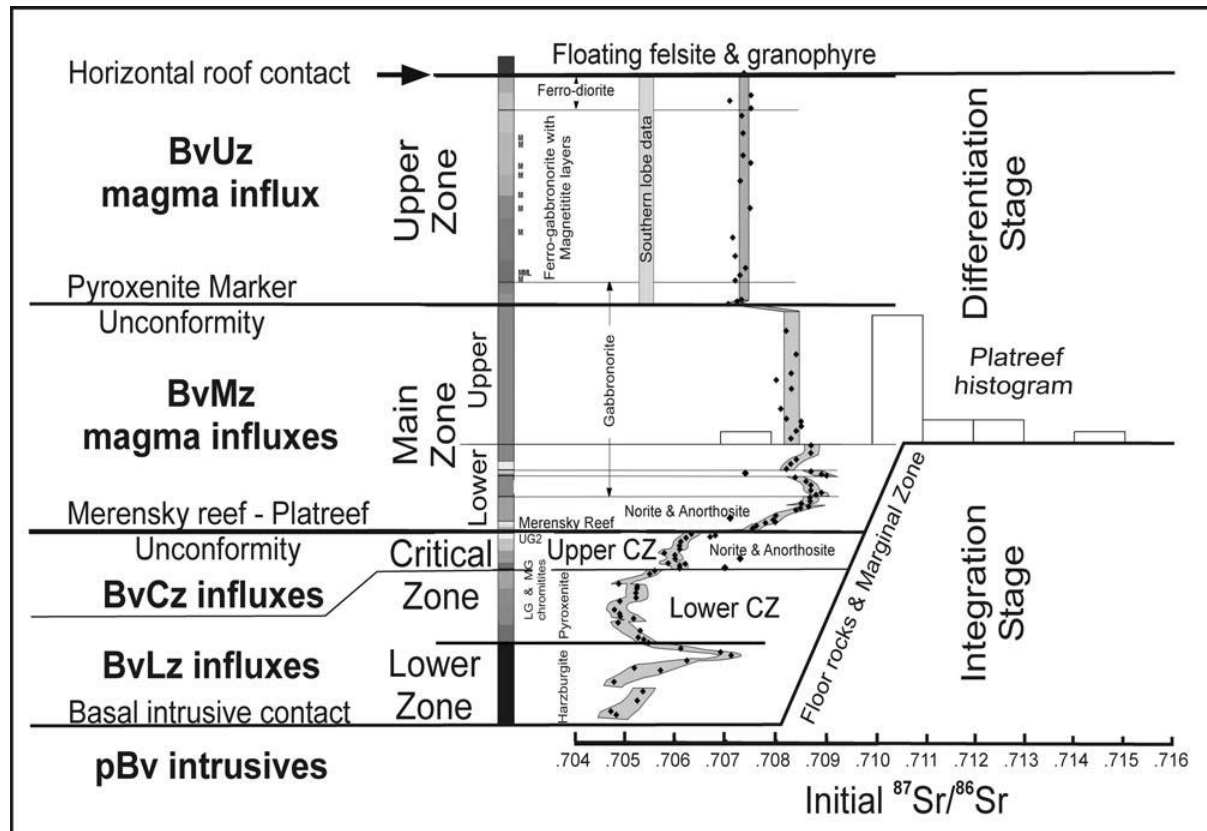


Figure 3: Stratigraphic and isotopic summary showing the mineralogical variation, Sr-isotopic variations, and the location of major unconformities of the RLS (Kruger, 2005).

1.2.3.1 Marginal Zone (MZ)

The Marginal Zone in the Western and Eastern Limbs comprises of varying suites of intrusives (gabbronorite, norite, pyroxenite, harzburgite), which form either sills in the floor or a contact layer at the base of the main Bushveld layered body (Maier *et al.*, 2021). The Marginal Zone is poorly developed in the Northern Limb of the BC (Grobler *et al.*, 2019). It occurs as a package of ~800 m thick, medium-grained, unlayered noritic rocks (Eales & Cawthorn, 1996). It forms the basal part of the RLS,

which formed as sills that intruded Transvaal metasedimentary rocks. The accessory minerals in this zone include clinopyroxene, quartz, biotite and hornblende (Kinnaird, 2005).

1.2.3.2 Lower Zone (LZ)

The Lower Zone (LZ), which is not always present, is an ultramafic succession that ranges from 800-1700 m in thickness. The thickness and distribution of the LZ is dependent on the topographical characteristics of the floor and its structure (Hulbert & von Grunewaldt, 1982; Yudovskaya *et al.*, 2013). In the Eastern Limb, the LZ succession is hosted in the Olifants River Trough (Hulbert, 1983) and the Clapham Trough. The LZ of the BC in the Olifants River Trough is subdivided into a harzburgite subzone that alternate with hard layers of orthopyroxenite (Scoon & Viljoen, 2019), which were described as bronzitite layers by Cameron (1978). The rocks have varying amounts of intercumulus plagioclase, clinopyroxene, biotite and chromite (Eales & Cawthorn, 1996). A distinguishing feature in this zone is the absence of chromitites (Roelofse, 2010).

1.2.3.3 Critical Zone (CZ)

The Critical Zone (CZ) is subdivided into the Lower Critical Zone (LCZ) and the Upper Critical Zone (UCZ). It is economically significant (Kinnaird *et al.*, 2005) as it hosts the Merensky Reef (MR), Upper Group 2 (UG-2) chromitite and 13 major chromitite layers (Maier *et al.*, 2021).

The 800 m thick LCZ consists of orthopyroxenitic rocks (Maier *et al.*, 2000) whereas the 400 m thick UCZ is composed of partial or complete cyclic units consisting of a basal layer of ultramafic cumulates, chromitite, harzburgite, and pyroxenite, through norite to anorthosite towards the top (Kinnaird *et al.*, 2005). The UCZ is characterized by the first occurrence of cumulus plagioclase at its base (Roelofse, 2012), resulting in the occurrence of norites and anorthosites (Maier *et al.*, 2000). The LCZ/UCZ boundary occurs at the base of the Middle Group 3 (MG3) chromitite (Kinnaird *et al.*, 2005).

1.2.3.4 Main Zone (MZ)

The UCZ/LMZ boundary is located at the top of the giant mottled anorthosite layer, and it consists of a thick succession of norites and gabbronorites devoid of olivine or chromium spinel (Boorman *et al.*, 2004). The 3 km thick Main Zone (MZ) is the

thickest zone of the RLS and consists mostly of gabbronorites that do not contain olivine or chromite (Kinnaird *et al.*, 2005). The cumulus minerals in the MZ include plagioclase, augite, orthopyroxene and pigeonite (Eales & Cawthorn, 1996). The MZ is visually not well layered but shows distinct cryptic layering when compared to the CZ (Mitchell, 1990).

The MZ is host to a prominent orthopyroxenite layer referred to as the “Pyroxenite Marker”. The Pyroxenite Marker occurs near the top of the MZ in the Eastern and Western Limbs (Cawthorn *et al.*, 1991). The Pyroxenite Marker is believed to have formed due to localized super cooling and the suppression of plagioclase crystallization (Maier *et al.*, 2001). Sharpe (1985) observed a reversal in mineral compositions and a break in Sr-isotopic composition at the level of the Pyroxenite Marker, attributing these observations to a major influx of primitive magma into the RLS at the level of the Pyroxenite Marker, which is considered the level at which the last major influx of magma into the RLS occurred (Mangwagape *et al.*, 2016). The Pyroxenite Marker is considered to be the LMZ/UMZ boundary. In the Northern Limb, the Pyroxenite Marker is absent, with a troctolite unit occurring at approximately the same stratigraphic level instead (Mangwagape *et al.* 2016).

1.2.3.5 Upper Zone (UZ)

The Upper Zone (UZ) is a 2-3 km thick unit that hosts about 25 magnetitite layers in four groups (Kinnaird *et al.*, 2005). The first occurrence of cumulus magnetite is observed at the base of the UZ (Kruger, 1990). The rocks occurring in this zone include magnetite gabbros, anorthosites and olivine diorites (McDonald *et al.*, 2005). The placement of the boundary between the MZ and UZ is controversial, and authors like Kruger (1990) suggest that it should be placed at the level of the Pyroxenite Marker. The UZ is subdivided into three subzones. Subzone A is characterized by the introduction of cumulus magnetite whereas Subzone B and Subzone C are characterized by the appearance of olivine and apatite, respectively (Maier *et al.*, 2013).

1.3 Previous isotopic work on the Bushveld Complex

As the largest layered mafic intrusion and host of PGEs (McDonald & Holwell, 2011), the BC has attracted a great deal of research interest. The research that has been conducted in the Complex mainly focused on three Limbs, the Eastern, Western and the Northern Limbs. Much of the research conducted on the Complex focused on formation mechanisms of the Complex (e.g. Latypov *et al.*, 2016 and references therein), correlating zones of mineralization (e.g Merensky Reef and Platreef) (e.g. Yudovskaya *et al.*, 2017) and determining the origin and formation of the PGE-rich horizons (e.g. Cawthorn, 2005 and references therein).

Several studies on the BC focussed on the Sr-isotopic stratigraphy of the different limbs. One of the early isotopic studies performed on the BC was that of Sharpe (1985), who conducted isotopic work on the Eastern Limb of the BC. He discovered that all Bushveld marginal rocks have higher R_0 (initial $^{87}\text{Sr}/^{86}\text{Sr}$ ratio) values than expected, suggesting that these high values may have been caused by contamination on a local or regional scale, or rubidium (Rb) mantle enrichment. Regional contamination was suggested to be the most probable mechanism, especially for the MZ, as R_0 values are up to 0.7086, exceeding those of possible local contaminants like the Rooiberg felsites ($R_0 < 0.708$). The R_0 values remain fairly constant through the MZ, with fluctuations encountered 300 – 500 m below the Pyroxenite Marker. At the same interval below the Pyroxenite Marker, a decrease in R_0 is encountered to 0.708, followed by a major decrease to 0.7073 within a 25 m interval centered on the Pyroxenite Marker. The R_0 then remains constant at ~0.7073 above the Pyroxenite Marker (Sharpe, 1985) (Figure 3).

Several studies have been conducted to investigate the Sr-isotopic composition of plagioclase in the Merensky pyroxenite. The plagioclase in the Merensky pyroxenite from Amandelbult has a MZ-like Sr isotopic signature of $\text{Sr}_i = 0.7075$ (Field, 1987) whereas the plagioclase in the Merensky pyroxenite from Rustenburg (Kruger & Marsh, 1982), Atok (Lee & Butcher, 1990) and Union Section (Eales *et al.*, 1986) has a CZ signature of $\text{Sr}_i = 0.7064$.

Eales *et al.* (1990) conducted a study on the UG1 Footwall (UG1FW) which occurs between the MG4 and UG1 chromitites of the UCZ in the Western Limb of the BC. The initial $^{87}\text{Sr}/^{86}\text{Sr}$ ratios from one sample to another vary in an unpredictable

manner, indicating that the UG1FW did not form from a single, homogenous melt. The plagioclase and orthopyroxene crystals within the same sample were also analysed separately and they had isotopic signatures that varied significantly. The model of formation that was adopted by the authors entails that a hotter, more primitive liquid was periodically injected and mixed with a cooler, more evolved, supernatant liquid.

Lee and Butcher (1990) conducted a Sr-isotopic study on samples taken from the Atok Section at Lebowa Platinum Mines in the Eastern Limb of the BC. The study was conducted on the Merensky and Bastard Reefs, and it was discovered that both units resemble a well-defined cyclic pattern of variation. From the middle of the Merensky Reef there is an increase in $^{87}\text{Sr}/^{86}\text{Sr}$ from 0.7065 ± 2 (norite), through 0.7069 ± 2 (leuconorite), up to 0.7074 ± 2 (poikilitic anorthosite). The base of the Bastard Reef is characterized by a pyroxenite with an extraordinarily high $^{87}\text{Sr}/^{86}\text{Sr}$ ratio of 0.7090 ± 2 and it contains visible metal sulphides. 0.4 m above the base of the Bastard Reef, the pyroxenite exhibits a reversal in the initial $^{87}\text{Sr}/^{86}\text{Sr}$ profile back to 0.7062 ± 2 , making the pyroxenite indistinguishable from the pyroxenite at the base of the Merensky Reef. The variation in initial $^{87}\text{Sr}/^{86}\text{Sr}$ from the middle portion of the Bastard Reef Unit (norite) to the upper poikilitic anorthosite had a similar trend to that of the Merensky Reef described above, increasing from 0.7063 ± 2 (norite) to 0.7078 ± 1 (poikilitic anorthosite). The Merensky and the Bastard Reef units have been interpreted as cyclic units that formed through repeated injection of new magmas which had similar geochemical signatures (Lee & Butcher, 1990).

Kruger (1994, 2005) conducted a study on the Sr-isotopic stratigraphy of the Western Limb of the BC, where it was suggested that the evolution of the magma chamber occurred in two stages, namely, Integration Stage and a Differentiation Stage (Figure 3). The Integration Stage covers the LZ to the LMZ, while the Differentiation Stage covers the UMZ to the UZ. The Integration Stage is characterized by the repeated influx of magmas of contrasting isotopic composition and shows a sharp isotopic discontinuity at the boundary between the CZ and MZ. The Differentiation Stage is characterized by large-scale fractional crystallization with minimal addition of new magma and the isotopic trend is uniform except for the major deflection at the Pyroxenite Marker (Kruger, 1994 & 2005).

Coexisting plagioclase and orthopyroxene cumulates within the Merensky and Bastard units were found to exhibit a Sr-isotopic disequilibrium. The plagioclase exhibits a MZ-like Sr isotopic signature while the orthopyroxene resembles a CZ-like signature (Seabrook *et al.*, 2005). A similar disequilibrium was observed by Roelofse & Ashwal (2012) between coexisting plagioclase and orthopyroxene crystals from the MZ. Both studies point to the importance of the mixing of minerals from isotopically dissimilar magmas in the Critical and Main Zones of the BC.

Tegner *et al.* (2006) conducted an investigation in the Main and Upper zones of the BC where the initial $^{87}\text{Sr}/^{86}\text{Sr}$ ratios are near-constant (0.7073 ± 0.0001) above the Pyroxenite Marker. This ratio implies that the units crystallized from a homogeneous magma without injection of new magmas or assimilation.

Yang *et al.* (2013) conducted a Sr-isotopic study on plagioclase in the UCZ of the RLS. They discovered that there was Sr-isotopic disequilibrium in cores and rims of plagioclase grains in the UG1 unit and its noritic footwall, in the Merensky pyroxenite and in the Bastard anorthosite. The cores of different plagioclase grains in the Merensky Reef, footwall anorthosite and footwall norite also exhibited Sr-isotopic disequilibrium. Slumping of semi-consolidated crystal slurries at the top of the CZ during subsidence of the center of the intrusion is suggested to be the mechanism responsible for the formation of these rock intervals.

Roelofse *et al.* (2015) conducted a Sr-isotopic study on samples from the MZ and UZ of the BC. The data presented by Roelofse *et al.* (2015) show that co-existing plagioclase may have formed from multiple magmas that had different isotopic signatures. The model of formation suggested in this study is the intrusion of different crystal mushes originating from a sub-Bushveld staging chamber that was contaminated by crustal rocks of the Kaapvaal craton.

According to a study by Mangwegape *et al.* (2016), the plagioclase in the LMZ of the Northern Limb of the BC is characterized by significant variations in Sr-isotopic compositions and limited differentiation suggesting that it was constructed through repeated influxes of magmas. The UMZ and UZ are characterized by rather constant Sr-isotopic compositions of plagioclase and normal differentiation, suggesting that these zones formed in response to fractional crystallization. The average $^{87}\text{Sr}/^{86}\text{Sr}$ ratio of the plagioclase in the LMZ recorded a value of 0.7088, with individual spots

ranging from 0.7075 to 0.7106. In comparison to the LMZ, the UMZ plagioclase has an average $^{87}\text{Sr}/^{86}\text{Sr}$ ratio of 0.7078, while individual spots exhibit a narrower range, ranging from 0.7069 to 0.7087. The average $^{87}\text{Sr}/^{86}\text{Sr}$ ratio of plagioclase in the UZ is 0.7073 with individual spots ranging from 0.7063 to 0.7079.

Wilson *et al.* (2017) conducted an in-situ Sr-isotopic investigation on plagioclase in the lower part of the eastern BC. The $^{87}\text{Sr}/^{86}\text{Sr}_i$ ranges from 0.7042 to 0.7076, and the ultramafic cumulates of the Basal Ultramafic Sequence (BUS) have the lowest values while norites of the MZ have the highest values. The MZ norites formed through fractionation of melts that accumulated at the top of the BUS and contamination by metapelites that formed on the roof of the early sub-chamber. It was suggested that the lower part of the Eastern Limb of the BC was affected by crustal contamination originating from both the lower crust of the Kaapvaal Craton and the enclosing sediments, through consideration of the REE patterns, trace element modelling and Sr-isotopic compositions.

An in-situ Sr-isotopic study of plagioclase was conducted for the complete stratigraphic profile of the BC by Karykowski *et al.* (2017). The elevated Sr-isotopic compositions encountered were explained as being the result of the interaction between parental magma and fluids originating from underlying dolomites of the Transvaal Supergroup. The initial in-situ $^{87}\text{Sr}/^{86}\text{Sr}$ ratios of plagioclase in the LZ ranges between 0.7037 and 0.7077. The interstitial plagioclase within the LCZ pyroxenites have in-situ $^{87}\text{Sr}/^{86}\text{Sr}$ ratios between 0.7040 and 0.7061 while the cumulus plagioclase in the UCZ have values ranging between 0.7051 and 0.7066. The in-situ $^{87}\text{Sr}/^{86}\text{Sr}$ ratios for plagioclase in the MZ ranges from 0.7081 to 0.7097 while the UZ plagioclase have values between 0.7067 and 0.7084 (Karykowski *et al.*, 2017). Interstitial plagioclase from the LZ shows complex zonation patterns, which may be indicative of multiple injections of primitive magmas that had varying Sr_i ratios during the emplacement of this unit (Karykowski *et al.*, 2017).

1.4 Some topics of continued debate

Even though the BC has been researched for more than 150 years, several recent debates and controversies have arised, outlining uncertainties in the understanding of this layered intrusion. The formation of the Upper and Upper Main Zones in a closed system has been debated for several years. A closed-system crystallisation

means that the magma evolves and cools progressively in the magma chamber, without any magma replenishment (Fisher & Yuan, 2016). It has been suggested that the Upper and Upper Main Zones formed through differentiation of a single magma body due to the consistent initial strontium isotope ratios (0.7073 ± 0.0002) of the host rocks (Tegner *et al.*, 2006). This model is not in agreement with a model proposed by Cawthorn & Walraven (1998), which states that up to 40% of the magma may have been erupted. The latter model is proposed due to significant loss of incompatible elements such as K and Zr. The compositional reversals and isotopic differences between cumulus minerals indicate that the Upper and Upper Main Zones experienced an influx of magma pulses (Tanner *et al.*, 2014).

Latypov (2009) proposed that the liquid that was responsible for magma evolution was crystal-free but recent studies suggest that most magma can carry up to 55 vol% of crystals (Marsh, 2013). The thick anorthosite layers are believed to have formed through the emplacement of plagioclase mush (Raedeke & McCallum, 1982). Due to magnetic susceptibility and non-cotectic proportions of plagioclase, Ashwal *et al.*, (2005) and Roelofse & Ashwal (2012) suggest that this emplacement may have occurred in the Upper, Upper Main and Lower Main Zones, with an existing sub-Bushveld magma chamber, progressively feeding the actual Bushveld chamber with evolved magma.

1.5 Purpose of the study

Detailed Sr-isotopic stratigraphy studies have been conducted in the Western and Northern Limbs of the BC by Kruger (1994) and Mangwegape *et al.* (2016), respectively. Similar studies are necessary in the Eastern Limb at a scale that is comparable to those of the limbs mentioned. This study aims to provide a continuous and relatively high-resolution profile of variations in mineral chemistry, whole-rock major and trace elements, and Sr-isotopic composition of plagioclase throughout the UZ to the LCZ in the Eastern Limb of the BC. The data provided in this study will also be used to understand the extent and nature of magmatic replenishment events within the Eastern Limb of the BC. This study will also provide the ICDP project on the Bushveld Complex (BVDP) with basic petrological and geochemical data that may be used as a framework for future work on the drill cores donated by Impala Platinum towards the project.

2. Methodology

2.1 Sampling

Sampling was conducted at the core storage facility of the University of the Free State where fifty-eight (58) drill core samples (Figure 4) were collected from boreholes BH7772, BH7771, BH6958 and BH8172 (Figure 2 & 5) at an average sampling interval of ~100 m. The boreholes are from the Eastern Limb of the BC, covering ~5 000 m of the stratigraphy from the UZ to the LG5 chromitite in the LCZ.

The 1 337 m deep BH7772 is located at 24°30'32.98"S 29°53'40.15"E and it covers the UZ in the first 1 220 m of the borehole, with the remainder of the borehole representing the UMZ. BH7771 is 2 696.38 m deep and it covers the MZ for the first ~2 620 m and the upper parts of the UCZ from ~2 620 m to 2 696 m. The geographical coordinates of BH7771 are 24°27'47.48"S 29°52'19.83"E. The 919.64 m deep BH8172, located at 24°29'47.50"S 30°2'7.91"E, covers the LMZ to UCZ at the level of the Merensky Footwall. The 780.94 m deep BH6958, located at 24°29'6.92"S 30°4'1.24"E, covers the CZ from the level of the Merensky Footwall to the pyroxenite ~9 m below the LG5 chromitite.

Of the 58 samples, 14 are from BH7772, 29 are from BH7771, 14 are from BH6958 and 1 is from BH8172. The samples were labelled TM 1.1 to TM 1.48. The collected samples were halved using an automatic core cutter. The archive halves were returned to the core boxes for future investigations.



Figure 4: Photograph showing the 58 samples collected for this study. Sample positions are shown in Figure 5.

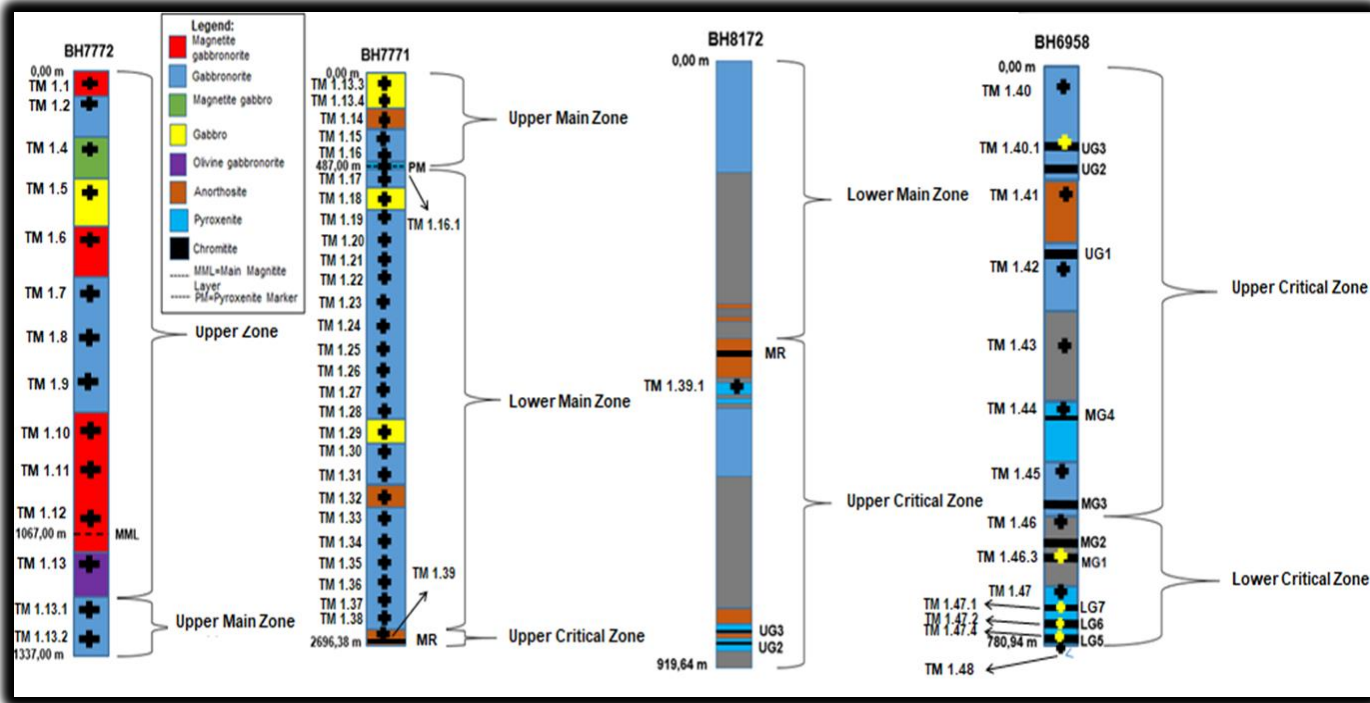


Figure 5: Schematic representation of the four studied boreholes.

2.2 Petrography

Fifty-eight (58) polished thin sections (Figure 6) were produced and studied using transmitted light microscopy. An Olympus BX51 petrographic microscope (Figure 7) was utilized to determine the modal mineralogical compositions of samples through visual estimation, while photomicrographs were captured with an Olympus SC20 camera attached to the microscope. The polished thin sections were also used to describe the textural relationships between minerals within the rocks.



Figure 6: Photograph showing the thin sections prepared from samples collected for this study.



Figure 7: The Olympus BX51 petrographic microscope used for the petrographic examination of samples for this study.

2.3 Whole-rock major and trace element geochemistry

Sample preparation for whole-rock major and trace element geochemistry started with crushing and milling of samples with a jaw-crusher and swing mill, respectively, to produce fine powders. Each powdered sample was dried by heating 10 g of the powder to 110°C overnight and the loss on ignition (LOI) was gravimetrically determined after heating of the sample to 1000°C for 4 hours. An aliquot of 0.28 g of powdered sample was mixed with a flux containing 0.2445 g La₂O₃, 0.705 g Li₂B₄O₇, 0.5505 g Li₂CO₃ and 0.02 g NaNO₃. The mixture was heated for 5 minutes in a Pt crucible, with the resultant melt subsequently poured into a mould and pressed to form a fusion disc.

For trace element and Na₂O determinations, 8 g of sample powder was added to 3 g of Hoechst wax (C₆H₈O₃N₂) and mixed for 20 minutes to form a homogeneous mixture using a Turbula mixer. Pressed pellets were then produced by pressing the mixture using a hydraulic press. Fusion discs and pressed powder pellets were

analysed on a PANalytical Axios Wavelength Dispersive X-ray fluorescence spectrometer to determine the major and trace element compositions, respectively. The XRF spectrometer has an Rh end window tube, with 4 kW anode (constituting of Rh) and a W cathode (filament). The peak voltage of the tube is 60 kV, with current altering in order to maintain 4 kW. For qualitative and quantitative analysis, the XRF spectrometer is equipped with modern software (Super Q V.4).

2.4 Mineral chemistry

Electron probe micro-analysis (EPMA) is a technique that uses an electron beam to excite X-rays on small, selected areas of a solid sample for non-destructive chemical analysis (Reed, 2005). The main purpose of an electron microprobe is to quantitatively determine the chemical composition of a very small spot (1-2 microns).

A Cameca SX-100 Microprobe (Figure 8) was utilized for EPMA data acquisition at the Department of Geology (University of Johannesburg). The samples were analysed under the following analytical conditions: 15 kV accelerating voltage, 20 nA electron beam current, beam size of ~1 micron, and counting times of 10 seconds and 5 seconds on peak and background, respectively, with the exception of potassium, which was analysed for 30 seconds on peak and 15 seconds on background.

Na, Mg, Al, Si, K, Ca, Ti, Mn, Cr and Fe were measured on their Ka-lines and the oxygen content was calculated by stoichiometry, assuming common oxidation states for the cations. Natural standards that were used for calibration included jadeite (Na), almandine (Al), diopside (Mg, Si), orthoclase (K), wollastonite (Ca), rhodonite (Mn) and hematite (Fe), while the synthetic standards included TiO_2 (Ti) and Cr_2O_3 (Cr). The ZAF matrix correction method was used for quantification. As a specimen is thicker, the intensity of the emitted characteristic X-rays is influenced by the atomic number effect, the absorption effect and the fluorescene excitation effect. Corrections of these three effects were determined whereby the the relative X-ray intensities obtained from an unknown specimen against those from a standard specimen are measured. The corrections of the three effects were made to the relative intensities.

Fifty eight polished thin sections covering the entire stratigraphy were analysed using transmitted light microscopy to choose the euhedral to subhedral plagioclase crystals

(for those samples containing cumulus plagioclase). Of the 58 samples, 44 samples were later analysed with EPMA for in-situ major element determinations. Prior to analysis, the thin sections were carbon coated at the University of Johannesburg in order to ensure a conductive surface. Plus, or minus three crystals per sample were analysed with an average of three spots per crystal. The EPMA was also utilized to produce back-scattered electron (BSE) images (Figure 9) showing spots that were analysed during the analyses.



Figure 8: The Cameca SX-100 Microprobe, equipped with four wavelength dispersive spectrometers at the University of Johannesburg.

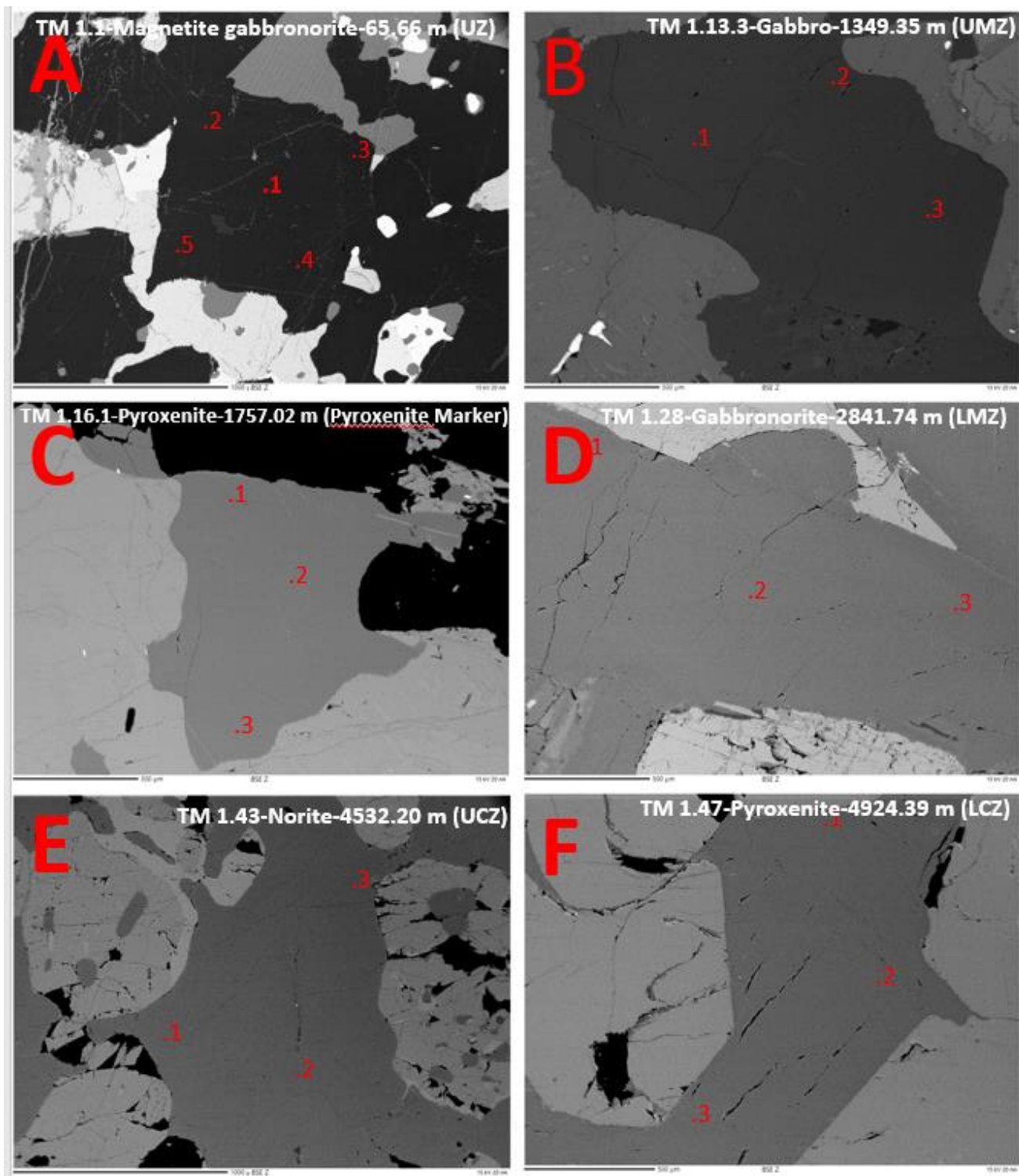


Figure 9: A selection of backscattered electron (BSE) images showing selected unaltered plagioclase crystals that were analysed by EPMA, including the positions of spots analysed.

2.5 Strontium-isotopic determinations

Thirty-four polished thin sections were used for the in-situ Sr-isotope analysis of plagioclase crystals. A minimum of three crystals per sample were analysed, with a minimum of three spots per crystal representing the core ($n=1$) and the rims ($n=2$) of the plagioclase crystals. The analyses were performed at the Spectrum Analytical Facility of the University of Johannesburg using a Nu Plasma II MC-ICPMS equipped with 16 Faraday detectors and 5 ion counting detectors, linked to a 193 nm ArF RESOlution SE excimer laser (Figure 10).

A few tests were performed to compare the results of ablating short lines vs spot ablations. It was decided that spot ablation produced the smallest measurement error and was also more appropriate for the purpose of the investigation. Line lengths varied between 170 to 220 μm while a spot size of 100 μm in diameter was used.

The plagioclase crystals were ablated with He gas at a repetition rate of 6 Hz for 60 seconds. The beam energy was 6 mJ with beam attenuation of 50%. Blank signal was measured for 20 seconds on peak positions before the start of ablation and subtracted from ablation signal to get a blank-corrected intensity.

For mass bias correction, the $^{86}\text{Sr}/^{88}\text{Sr}$ ratio was used to calculate and correct Sr mass fractionation. The Sr correction factor was regularly adjusted through analysis of the BHVO-2 glass reference standard ($^{87}\text{Sr}/^{86}\text{Sr} = 0.703469 \pm 0.000014$) to correct for Rb mass fractionation (Elburg *et al.*, 2005). ^{84}Kr and ^{86}Kr were subtracted from ^{84}Sr and ^{86}Sr during blank correction. ^{87}Rb was calculated from ^{85}Rb after mass bias correction and subtracted from the total signal at mass 87 to obtain ^{87}Sr . Other secondary standards that were also used to evaluate accuracy after every 8th unknown, included an in-house plagioclase glass standard ($^{87}\text{Sr}/^{86}\text{Sr} \sim 0.7072$) and calcite WC-1 ($^{87}\text{Sr}/^{86}\text{Sr} = 0.706930$) (Rasbury *et al.*, 2021). Initial $^{87}\text{Sr}/^{86}\text{Sr}$ ratios were calculated for an age of 2054.4 Ma (Scoates & Friedman, 2008), with a decay constant of $1.39 \times 10^{-11} \text{ y}^{-1}$ (Nebel *et al.*, 2011).



Figure 10: The Nu Plasma II MC-ICPMS linked with 193 nm ArF RESOlution SE excimer laser housed at the Spectrum Analytical Facility of the University of Johannesburg.

3. RESULTS

3.1 Petrography

3.1.1 Macroscopic descriptions

3.1.1.1 Upper Zone samples

Magnetite Gabbronorite

Magnetite gabbronorites were sampled in the UZ at different stratigraphic levels. The magnetite gabbronorites are medium crystalline with crystals ranging between 1–5 mm. They are greyish in colour, with the milky/white colour representing plagioclase and the black colour representing pyroxenes (Figure 11A).

Magnetite Gabbro

A magnetite gabbro is an intrusive igneous rock, which consist primarily of plagioclase feldspar and clinopyroxene, with magnetite forming part of the primary minerals. The magnetite gabbro sampled in the UZ is medium crystalline and greyish in colour (Figure 11B). The whitish component is the plagioclase and the black minerals are pyroxenes and magnetite.

Gabbro

A gabbro is defined as a mafic intrusive rock, composed predominantly of plagioclase feldspar and clinopyroxene. The gabbro sampled in this study is medium crystalline and has a grey colour (Figure 11C). The crystals range between 1-5 mm, and it is black to greenish in colour. The black minerals are predominantly clinopyroxene while the white minerals are plagioclase.

Gabbronorite

A gabbronorite is a mafic rock composed of calcium-rich plagioclase, ortho- and clinopyroxene. The gabbronorites are medium crystalline with crystals ranging between 1–5 mm. They are greyish in colour, with milky colour representing plagioclase and the black minerals representing pyroxenes (Figure 11D). Some of the gabbronorites sampled were sulphide-bearing.

Olivine Gabbronorite

An olivine gabbronorite is a gabbronorite with more than 5% olivine. It is a medium crystalline rock that was sampled near the base of the UZ, containing crystals that

range between 1-5 mm in size. It is black to green in colour, with black/green components representing mostly pyroxenes and white components representing plagioclase (Figure 11E).



Figure 11: Photographs of selection of samples from the UZ: A) Magnetite gabbronorite; B) Magnetite gabbro; C) Gabbro; D) Gabbronorite with a magnetitite layer; E) Olivine gabbronorite.

3.1.1.2 Upper Main Zone samples

Gabbronorite

Gabbronorite is the most dominant rock type in the UMZ, followed by gabbro and anorthosite in the sampled stratigraphy. Gabbronorite is generally medium-grained with crystal sizes ranging between 1 mm and 5 mm. The gabbronorite is greyish in colour, with milky colour representing plagioclase and the black minerals representing pyroxenes (Figure 12A).

Gabbro

The gabbro in the UMZ is black to green in colour, with white components representing plagioclase while the black/green components represent the pyroxenes. It is medium crystalline and the crystals size ranges between 1-5 mm (Figure 12B)

Anorthosite

Anorthosite is an intrusive igneous rock composed predominantly of calcium-rich plagioclase. The anorthosite in the UMZ is medium to coarse crystalline, whereby crystals are more than 5 mm in size. The anorthosite is mostly white in colour due to the abundance of plagioclase (Figure 12C).



Figure 12: Photographs of selection of samples from the UMZ: A) Gabbronorite; B) Gabbro; C) Anorthosite.

3.1.1.3 Pyroxenite Marker sample

Pyroxenite

The Pyroxenite Marker marks the boundary between the UMZ and the LMZ. The dominant rock type at this level is orthopyroxenite. The sampled pyroxenite is

medium crystalline and has crystals that range between 1 and 5 mm in size. It is black to green in colour (Figure 13A).



Figure 13: Photograph showing the sample taken from the Pyroxenite Marker.

3.1.1.4 Lower Main Zone samples

Gabbronorite

The LMZ is mostly gabbronoritic, containing gabbronorites with layers of gabbro and anorthosite in the sampled stratigraphy. The gabbronorite in the LMZ is medium crystalline, with crystals ranging between 1 mm and 5 mm in size. The gabbronorites contain calcium-rich plagioclase and pyroxenes, represented by white and black/green minerals in the rocks, respectively (Figure 14A).

Gabbro

The gabbro contained in the LMZ is medium crystalline, with crystals ranging between 1 mm and 5 mm. The gabbro is black to green in colour, with white components representing plagioclase and the black/green components representing mostly clinopyroxene (Figure 14B).

Anorthosite

The anorthosite is dominantly white in colour and has spots of black minerals. This is due to the dominance of calcium-rich plagioclase and the low abundance of mafic minerals. Most of the LMZ anorthosites sampled were spotted rather than mottled anorthosites. The anorthosite is medium-coarse crystalline (Figure 14C)



Figure 14: Photographs of selection of samples from the LMZ: A) Gabbronorite; B) Gabbro; C) Spotted anorthosite.

3.1.1.5 Upper Critical Zone samples

The UCZ has alternating layers of different rock types that will be described below:

Anorthosite

The spotted anorthosite is dominantly white with black/green spots of mafic minerals. The light colour is attributed to the calcium-rich plagioclase feldspar that is contained in the rock (90-100%). The anorthosite is medium-coarse crystalline (Figure 15A).

Gabbronorite

Gabbronorite is the dominant rock type in the UCZ. The gabbronorite is more whitish due to the high plagioclase content, with black spots of both ortho- and clinopyroxene. The gabbronorite is fine-medium crystalline with crystals ranging between 1-5 mm (Figure 15B).

Chromitite

Chromitite is an igneous cumulate rock composed mostly of the mineral chromite. It is the main economic source for the mining of chromite. It is a fine-medium crystalline rock which occurs as thin to thick layers within the gabbronoritic

cumulates. A photograph of the UG3 chromitite is shown in Figure 15C, where it is underlain by an anorthosite. The chromitite is black in colour.

Norite

The sampled norite is medium crystalline, with crystals ranging between 1-5 mm. It is composed of essential plagioclase and orthopyroxene (Figure 15D).

Pyroxenite

The sampled pyroxenite is medium crystalline, with crystals ranging between 1 mm and 5 mm in size. The pyroxenite is melanocratic to hypermelanic (Figure 15E).



Figure 15: Photographs of selection of samples from the UCZ: A) Anorthosite; B) Gabbronorite; C) UG3 chromitite with underlying anorthosite; D) Norite; E) Pyroxenite.

3.1.1.6 Lower Critical Zone samples

The LCZ is largely pyroxenitic. In this study, only pyroxenites and chromitites were sampled from the LCZ.

Chromitite

The sampled chromitites in this study are fine-medium crystalline as shown by the LG5 and LG6 chromitites in Figure 16A. The chromitites are black in colour and occur interlayered with pyroxenite of the LCZ.

Pyroxenite

The sampled pyroxenite in the LCZ is medium crystalline, with crystals ranging between 1 mm and 5 mm in size. The sampled pyroxenite is dark in colour and predominantly consists of ortho- and clinopyroxene, with limited plagioclase (Figure 16B).



Figure 16: Photographs of selection of samples from the LCZ: A) LG5 and LG6 chromitites; B) Pyroxenite.

3.1.2 Microscopic descriptions

The petrographic observations on all fifty-eight samples, inclusive of the modal mineralogical composition, textural and crystal size information, are presented in Electronic Appendix 1. Of the 58 studied samples, gabbronorites accounted for 53%, while magnetite gabbronorites, gabbros and chromitites accounted for 9% each. Anorthosites and pyroxenites accounted for 7% each, while norites accounted for 3%. One sample of magnetite gabbro and one sample of olivine gabbro accounted for the remaining 3%.

The most dominant rock type sampled in the gabbronoritic UZ is magnetite gabbronorite, followed by gabbronorite, gabbro, olivine gabbro and magnetite gabbro. The dominant mineral observed in the sampled UZ is plagioclase, occurring

with intergranular clinopyroxene and orthopyroxene. Plagioclase exhibits parallel to sub-parallel orientation, which defines igneous layering (Figure 17A). Bent and wedge-shaped twin lamellae of plagioclase (Figure 17B) was observed in the sampled UZ, which has been interpreted as evidence of deformation after deposition by Von Gruenewaldt (1971). Plagioclase has been altered into fine-grained material believed to be sericite in this stratigraphic zone (Figure 17C).

Orthopyroxene and clinopyroxene exhibits twinning in the UZ. Magnetite occurs throughout the stratigraphy of the UZ. In most cases, the magnetite is enclosed by biotite, which was altered to chlorite in samples at the depth of 812.53 m and 1 005.31 m (Figure 17D). Olivine was encountered (Figure 17E) in three samples from the UZ, namely the gabbronorite (138.77 m), magnetite gabbronorite (418.31 m) and olivine gabbronorite (1 104.46 m). Inverted pigeonite also occurred in three samples from the UZ (Figure 17F). The dominant texture in this zone is intergranular texture, followed by subophitic and ophitic texture. Quartz also occurs as a primary late-stage mineral in some samples.

The sampled UMZ is characterized by gabbronoritic rock cumulates, with layers of gabbros and mottled anorthosites contained in this zone. Subophitic and intergranular textures are the most dominant textures in the rock cumulates of this zone (Figure 18A & 18B). Plagioclase is the dominant mineral in this zone, occurring as lath-shaped crystals and it exhibits polysynthetic twinning (Figure 18C). Orthopyroxene, clinopyroxene and inverted pigeonite (Figure 18D) also occur as cumulus minerals in this stratigraphic unit. Olivine is rare in the UMZ but there is one unusual sample that contains olivine, the gabbro at 1 447.51 m (Figure 18E). Clinopyroxenes also exhibit twinning, e.g in the gabbro at the depth of 1 349.35 m (Figure 18F). Quartz and biotite occur as a primary late-stage and secondary minerals respectively, and the latter has been altered into chlorite in some samples. Opaques also occur across the entire UMZ.

The UMZ/LMZ boundary is marked by a thick orthopyroxenite layer called the Pyroxenite Marker. Orthopyroxene is the dominant mineral in this layer, occurring with cumulus clinopyroxene. Plagioclase, olivine (Figure 19A) and inverted pigeonite (Figure 19B) are observed as intercumulus minerals with biotite and chlorite as secondary minerals. The sampled gabbroic LMZ is dominated by gabbronorites with

layers of gabbros and anorthosites. The cumulus minerals in this zone include plagioclase, orthopyroxene, clinopyroxene and inverted pigeonite. The gabbronorite at 2 076.38 m exhibits pinch and swell texture (Figure 19C). The majority of the samples contain clinopyroxene that are twinned (Figure 19D). Quartz occurs as a primary late-stage mineral while biotite, sericite and chlorite occur as secondary minerals. Opaques are also observed in this unit. Intergranular texture is the most dominant texture, followed by ophitic (Figure 19E), poikilitic and subophitic textures. Orthopyroxene crystals occur as oikocrysts with clinopyroxene and plagioclase chadacrysts in the gabbronorite from a depth of 1 782.05 m (Figure 19F).

The main lithologies sampled in the UCZ include pyroxenite, norite and anorthosites occurring with chromitite layers. In this study, the majority of the samples encountered in this zone are gabbronorites, norites, anorthosites and pyroxenites with the UG3 chromitite. This is a unit where the last cumulus plagioclase was encountered from the UZ, occurring with orthopyroxene and clinopyroxene. The dominant texture observed in this zone is intergranular texture (Figure 20A) with ophitic texture (Figure 20B) observed in some rock cumulates. A massive texture is observed in the UG3 chromitite (Figure 20C). The LCZ is predominantly pyroxenitic, occurring with Lower Group chromitite layers. The cumulus minerals in the rock cumulates are orthopyroxene and clinopyroxene, with chromite being the most dominant mineral in the chromitites. The pyroxenites have a poikilitic texture (Figure 20D) while the chromitites have a massive texture.

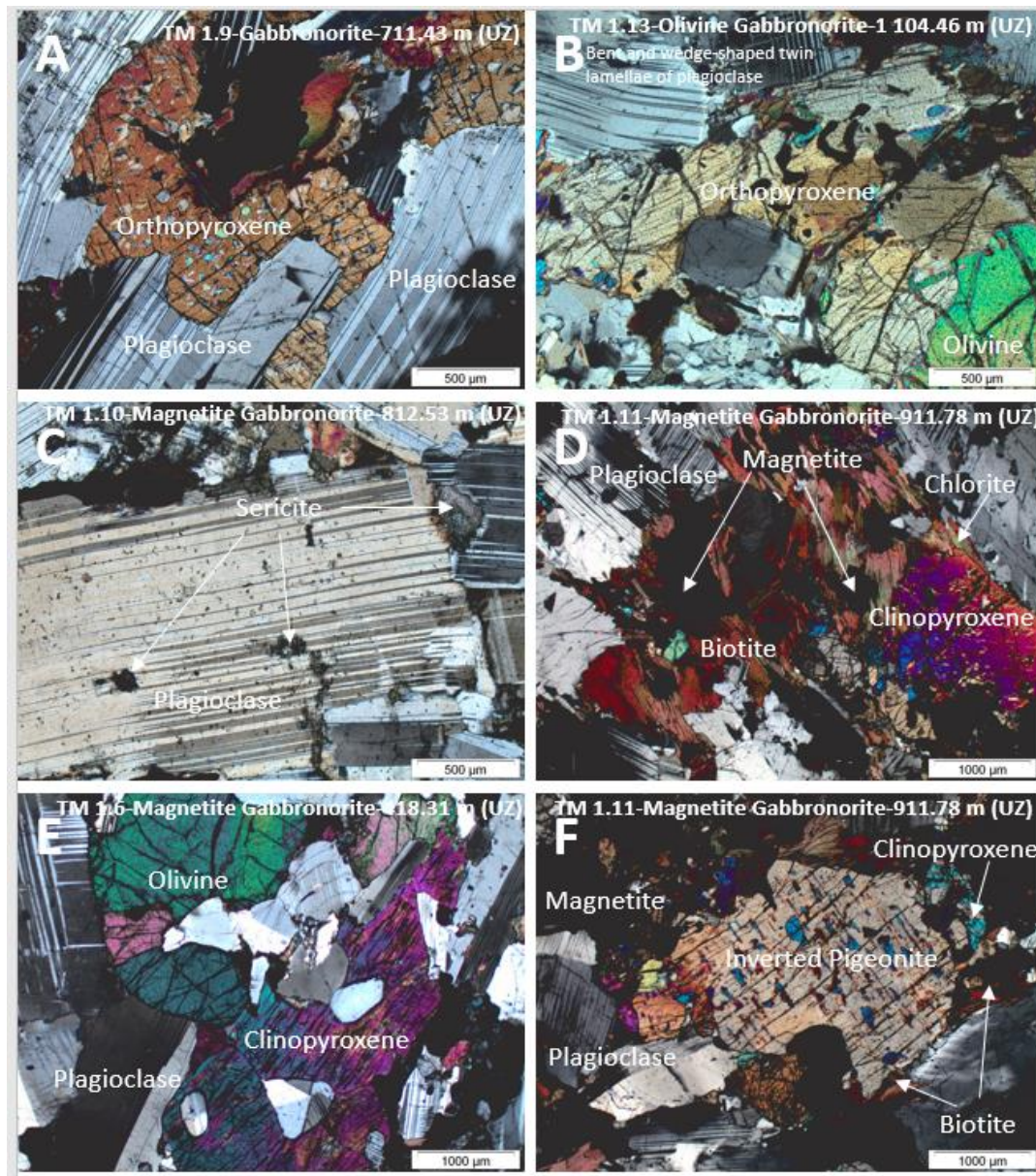


Figure 17: Cross-polarized transmitted light photomicrographs of: (A) Plagioclase crystals aligned in a parallel to sub-parallel orientation in gabbronorite, defining igneous layering that has been observed in most studied samples. Sample is from depth of 711.43 m; (B) Bent and wedge-shaped twin lamellae in the plagioclase of the olivine gabbronorite from a depth of 1 104.46 m; (C) Plagioclase in magnetite gabbronorite that has been altered along the rims and within the crystal, to sericite, from depth of 812.53 m; (D) Magnetite enclosed by biotite in the magnetite gabbronorite from depth 911.78 m, with biotite altered to chlorite; (E) Intercumulus plagioclase, olivine and clinopyroxene in the magnetite gabbronorite from depth of 418.31 m; (F) Inverted pigeonite surrounded by magnetite and biotite in the magnetite gabbronorite from depth 911.78 m.



Figure 18: Cross-polarized transmitted light photomicrographs of: (A) Orthopyroxene crystal enclosing lath-shaped plagioclase crystals, exhibiting subophitic texture contained in the gabbro from depth of 1 447.51 m; (B) Intergranular texture shown by cumulus plagioclase and clinopyroxene of the gabbronorite from the depth of 1 616.47 m; (C) Polysynthetic twinned plagioclase with intergranular orthopyroxene and clinopyroxene in the gabbronorite from the depth of 1 695.81 m; (D) Inverted pigeonite and plagioclase contained in the gabbro from the depth of 1 349.35 m; (E) Unusual olivine encountered in the gabbro from the UMZ at 1 447.51 m; (F) Clinopyroxene twinning contained in the gabbro from the depth of 1 349.35 m in the UMZ.

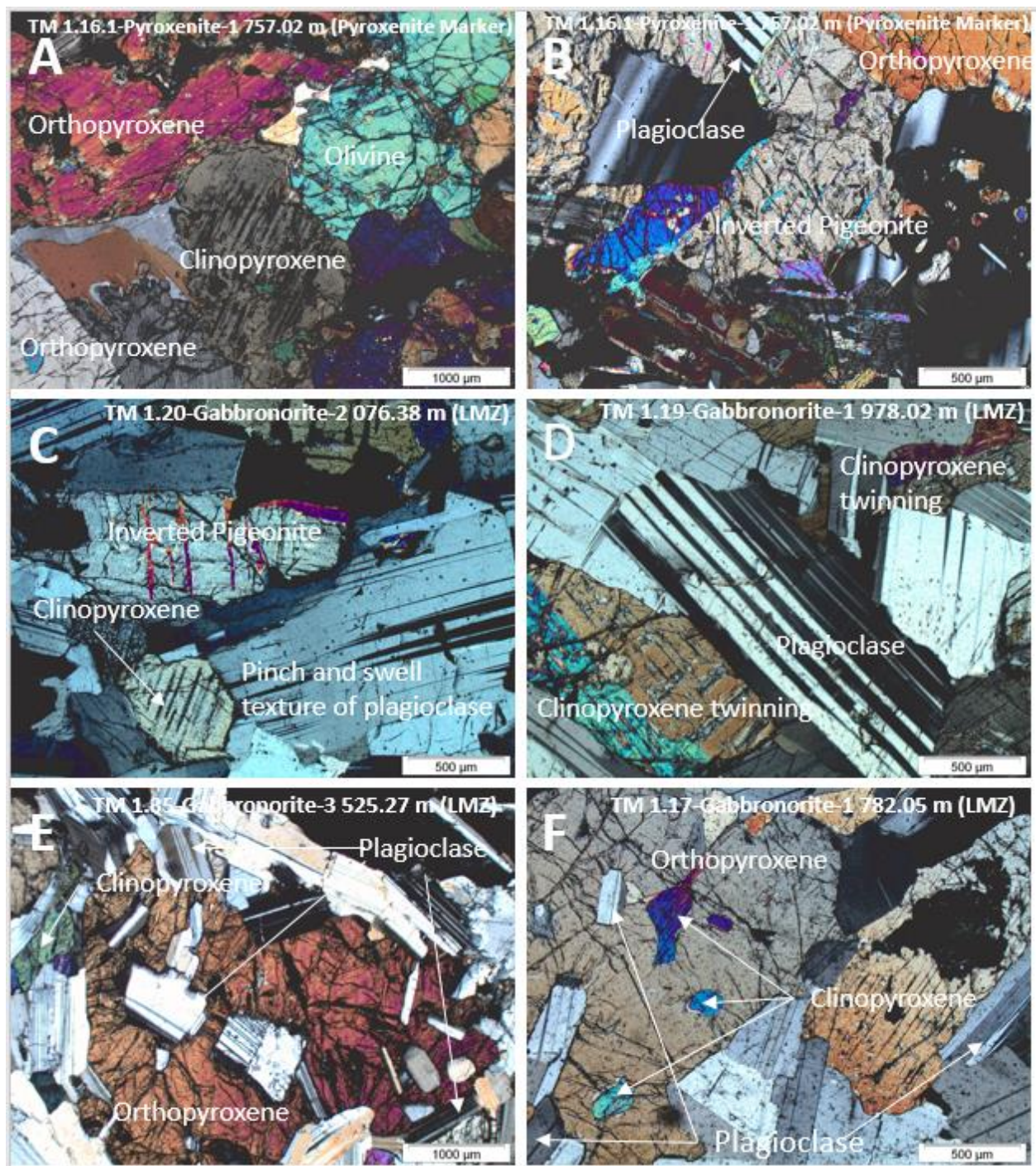


Figure 19: Cross-polarized transmitted light photomicrographs of: (A) Clinopyroxene, orthopyroxene and olivine crystals in the pyroxenite at the level of the Pyroxenite Marker; (B) Plagioclase, orthopyroxene and inverted pigeonite crystals observed in the pyroxenite at the level of the Pyroxenite Marker; (C) Clinopyroxene, inverted pigeonite crystals and a plagioclase crystal showing pinch and swell texture in the gabbronorite at 2 076.38 m; (D) Clinopyroxene crystals of the gabbronorite from the depth of 1 978.02 m exhibiting twinning; (E) Orthopyroxene and plagioclase crystals showing ophitic texture in the gabbronorite from the depth of 3 525.27 m; (F) Orthopyroxene oikocryst enclosing clinopyroxene and plagioclase chadacrysts in the gabbronorite from the depth of 1 782.05 m.

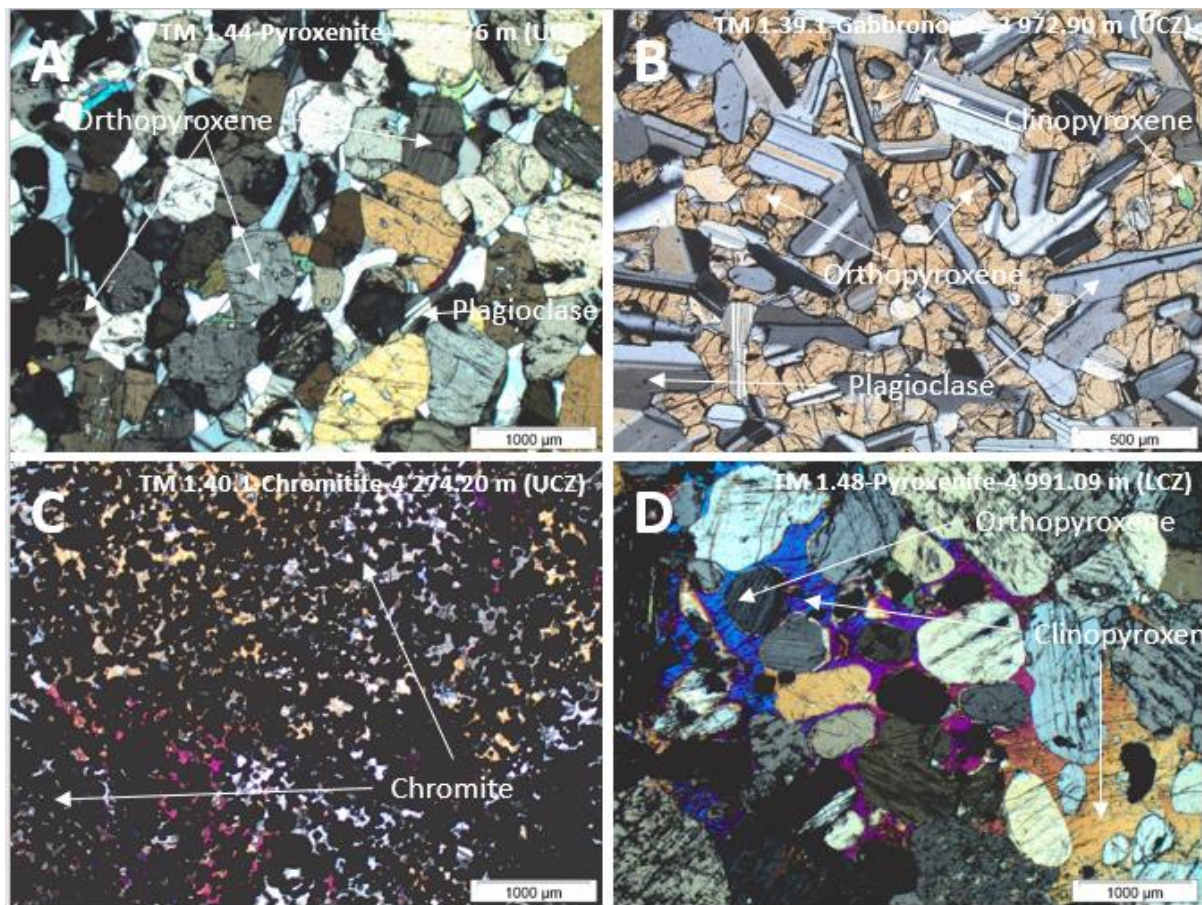


Figure 20: Cross-polarized transmitted light photomicrographs of: (A) Dominant pyroxene with interstitial plagioclase and clinopyroxene showing intergranular texture in the pyroxenite from the depth of 4 654.76 m in the UCZ; (B) Orthopyroxene and lath-shaped plagioclase crystals exhibiting ophitic texture in the gabbro at the depth of 3 972.90 m in the UCZ; (C) Massive texture shown by the dominant mineral chromite with traces of plagioclase and clinopyroxene in the UG3 chromitite; (D) Poikilitic texture shown by clinopyroxene enclosing orthopyroxene crystals in the pyroxenite at the depth of 4 991.09 m in the LCZ.

Variations in modal mineralogical composition with depth are shown in Figure 21. The dominant mineral in the sampled LCZ is orthopyroxene, with plagioclase occurring as an intercumulus phase. Chromite occurs at the level of the chromitite layers while clinopyroxene and quartz also occur as primary minerals. The boundary between the LCZ and UCZ is marked by the first appearance of cumulus plagioclase as observed between the MG2 and MG3 chromitite layers (Figure 21). The sampled UCZ is characterized by cumulus plagioclase as shown by the plagioclase peaks on Figure 21 and chromite at the level of the chromite stringers. The sampled UCZ also contains orthopyroxene and clinopyroxene as cumulus phases with quartz as a

primary late-stage mineral. The sampled LMZ is characterized by cumulus plagioclase, orthopyroxene, clinopyroxene and inverted pigeonite, with quartz occurring as primary late-stage mineral. Biotite occurs as a secondary mineral which is altered in most samples. At the level of the Pyroxenite Marker, which forms the LMZ/UMZ boundary, orthopyroxene is present in abundance. The UMZ contains plagioclase, clinopyroxene, orthopyroxene and inverted pigeonite as cumulus minerals. Olivine, which is commonly absent at this level, occurs in one sample in the UMZ. The UZ is characterized by the occurrence of cumulus plagioclase, clinopyroxene, orthopyroxene, magnetite, olivine and primary late-stage quartz. Inverted pigeonite and biotite also occur in the UZ.

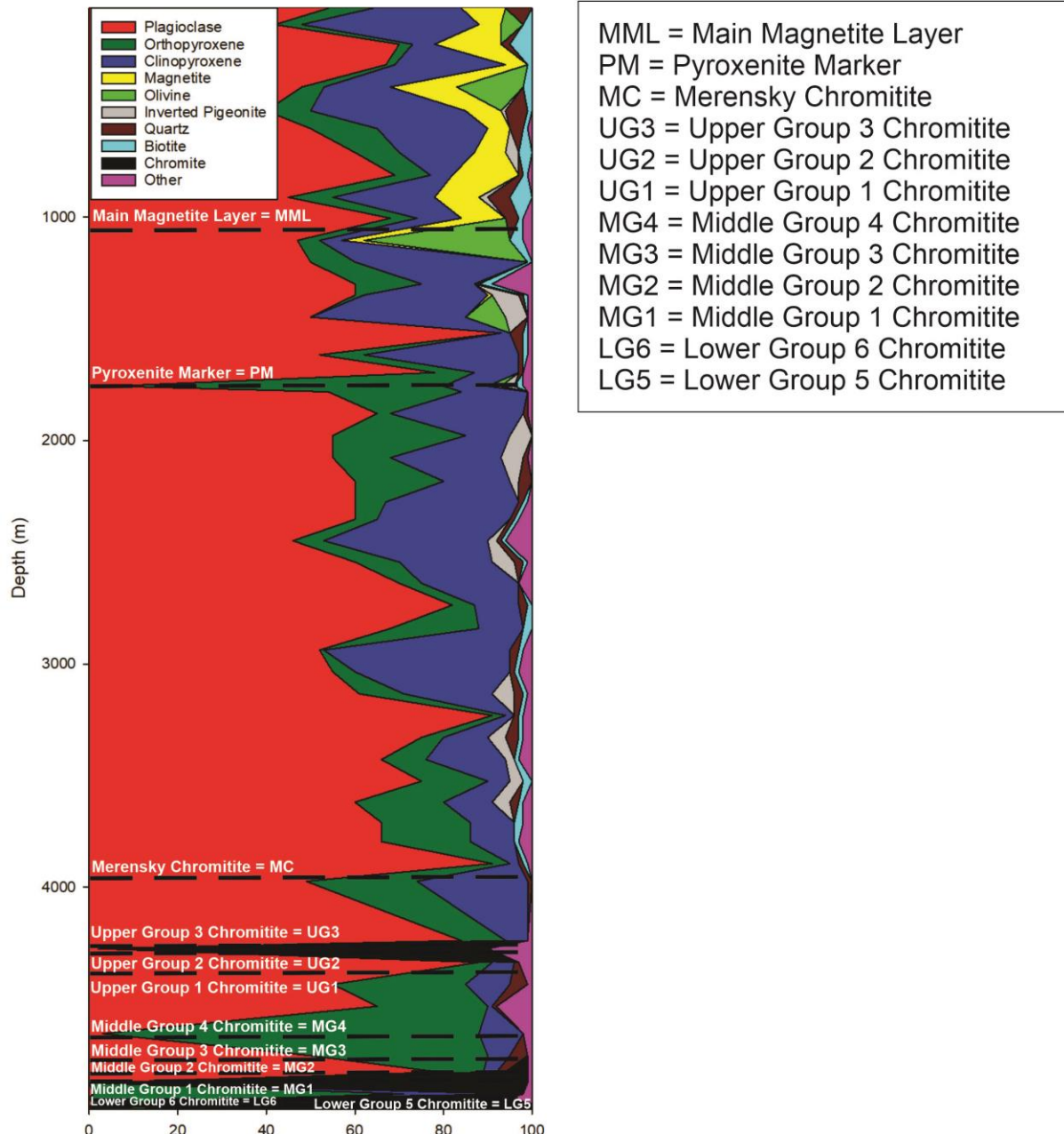


Figure 21: Variations in modal mineralogical composition with depth. Plagioclase, orthopyroxene and clinopyroxene are the dominant minerals in the stratigraphic profile. Magnetite and olivine occur mostly in the sampled UZ, while inverted pigeonite occurs mostly in the sampled LMZ. Quartz and biotite occur as minor minerals throughout the stratigraphic profile. Chromite is confined to the sampled CZ, where it locally forms chromitites.

3.2 Whole-rock major and trace element geochemistry

The major and trace element data of the 58 studied rock samples are presented in Appendix A1 and A2, respectively.

3.2.1 Whole-rock major element geochemistry

The SiO_2 content of the studied samples presented in Figure 22 averages 46.67 wt%, with the highest content observed at 2 352.82 m in the LMZ (gabbronorite). The lowest SiO_2 content is observed in the chromitite at depth 4 875.72 m in the LCZ. In the Upper and Critical Zones, the SiO_2 content averages below 46 wt%, while other stratigraphic units contain an average SiO_2 content that is above 50 wt%. TiO_2 content in the entire stratigraphy averages 0.70 wt%. The UZ has the highest TiO_2 average content compared to other stratigraphic units. This can likely be attributed to the presence of titaniferous magnetite within the UZ.

Al_2O_3 and CaO contents are high in all the rock samples, with the lowest contents observed in pyroxenites and chromitites. The P_2O_5 content is generally less than ~1 wt%, with the exception of two samples from the UZ, recording 2.07 wt% and 2.50 wt% at 138.77 m and 418.31 m, respectively, possibly due to the presence of apatite. The Fe_2O_3 content is lower in the Main and Upper Critical Zones compared to the Upper and Lower Critical Zones because of lack of mafic minerals in the former zones. Appreciable quantities of Cr_2O_3 are only observed in the chromite-bearing rocks of the CZ.

Al_2O_3 , CaO , K_2O and Na_2O show negative correlations with MgO in the binary variation diagrams presented below while Fe_2O_3 and MnO show positive correlations with MgO (Figure 22). The gabbronorites, anorthosites and norite contain lower concentrations of Fe_2O_3 and MnO because of the paucity of mafic minerals contained in these types of rocks, while the pyroxenites, chromitites and magnetite gabbronorites contain higher concentrations of Fe_2O_3 and MnO .

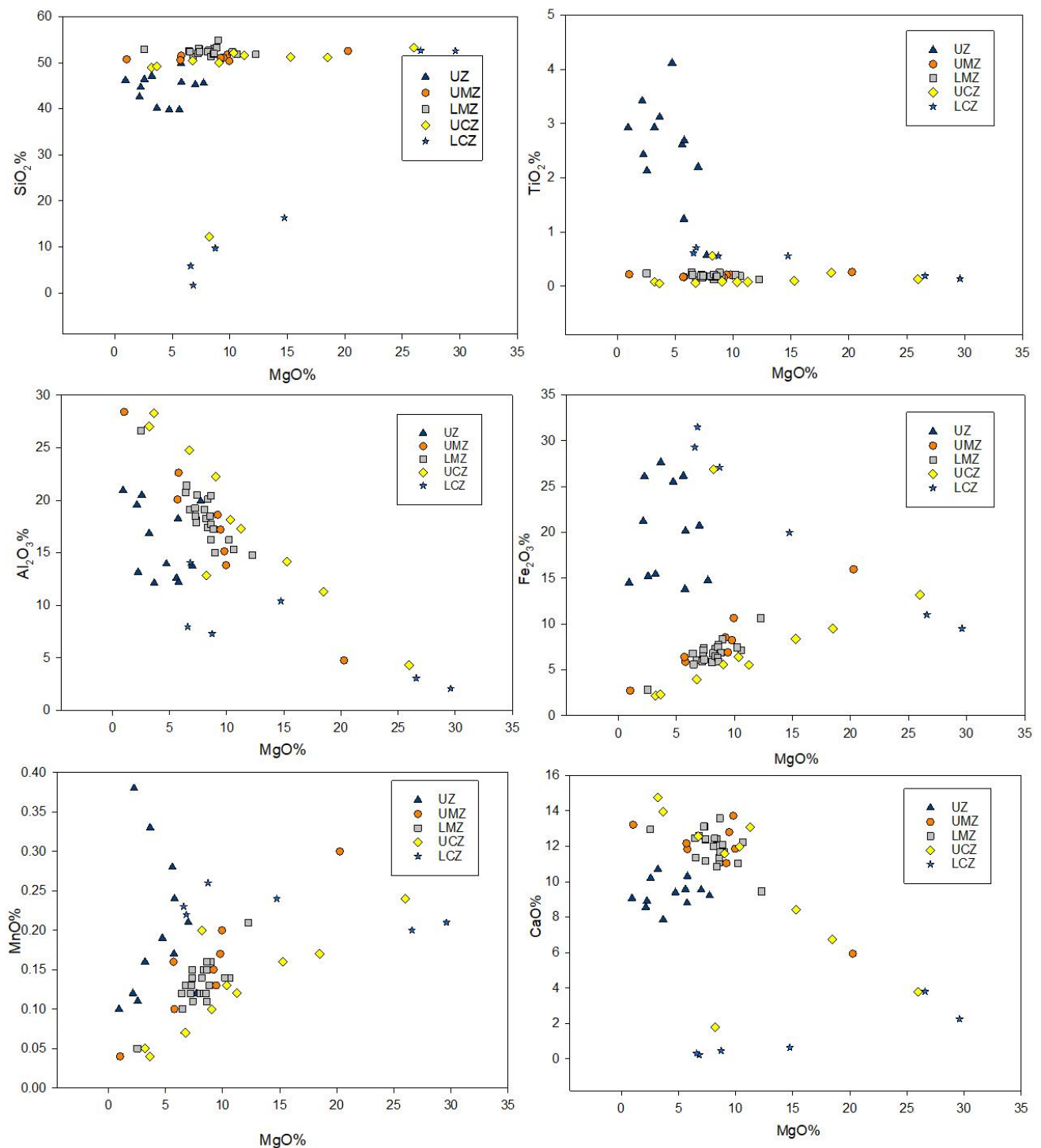


Figure 22: Binary variation diagrams of selected whole-rock major elements versus MgO.

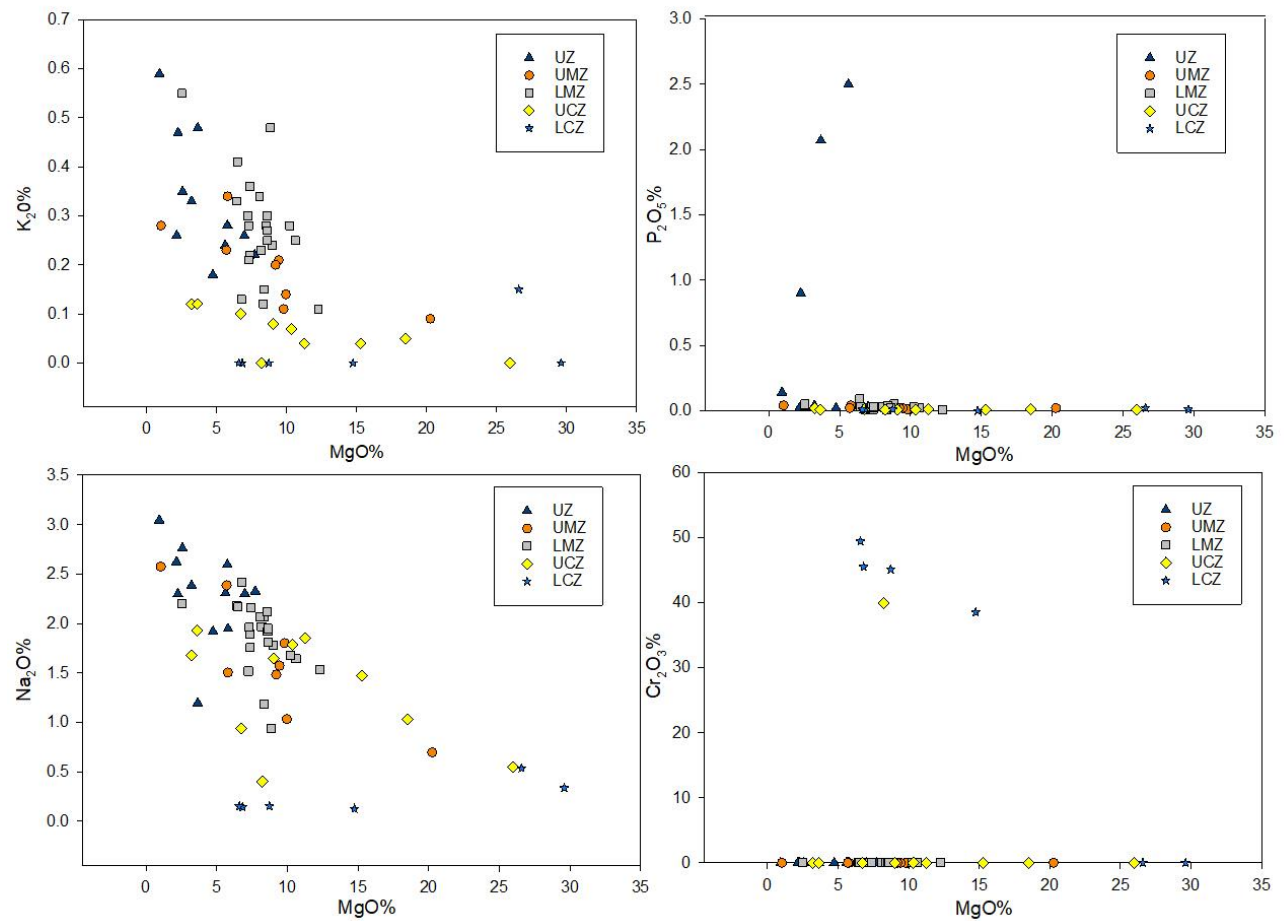


Figure 22: (Continued).

Whole-rock major elements were plotted against depth to observe their trends across the entire stratigraphy in Figure 23. SiO_2 concentrations remain relatively constant throughout the stratigraphy, with a decrease observed in the UZ. TiO_2 also remains relatively constant throughout the stratigraphy, but contrary to behaviour of SiO_2 , there is an increase in TiO_2 concentrations in the UZ, which might be attributed to the occurrence of Ti-rich magnetite. Al_2O_3 concentrations fluctuate throughout the stratigraphy, in-line with variations in the modal mineralogical composition.

Fe_2O_3 and MnO concentrations display a fluctuating trend in the sampled CZ, which is followed by a rather constant trend throughout the sampled LMZ. An increase in the concentrations are observed in the Upper Main and Upper zones. MgO and CaO show fluctuating trends in the sampled CZ, followed by a rather constant trend in concentrations throughout the remaining stratigraphy. K_2O and Na_2O concentrations show a generally increasing, albeit scattered trend upwards throughout the stratigraphy, with P_2O_5 concentrations showing a constant trend throughout the stratigraphy coupled with an increase in the sampled UZ, most likely as a result of the presence of apatite.

At the level of the Pyroxenite Marker, Al_2O_3 , CaO , K_2O and Na_2O are depleted as presented in Figure 23, while Fe_2O_3 , MgO and MnO are enriched as represented by the peaks. These peaks correspond with the high content of orthopyroxene in the modal mineralogy diagram. At 3 230.89 m, the anorthosite recorded high peaks of Al_2O_3 , K_2O and Na_2O while it was depleted in Fe_2O_3 , MgO and MnO , due to abundance of plagioclase. This observation corresponds with the plagioclase peak in the modal mineralogy diagram. At 4 826.62 m, the norite is enriched in Al_2O_3 , CaO and Na_2O as presented by the peaks in Figure 23, while it is depleted in Fe_2O_3 , MgO and MnO . This is the level at which the first cumulus plagioclase from the LCZ to the UCZ is encountered as represented by the plagioclase peak in the modal mineralogy diagram.

The variation of the calculated whole-rock Mg# with depth is shown in Figure 24. The Mg# is a petrological parameter that shows the ratio of the divalent cations of iron and magnesium in rocks ($\text{Mg\#} = \text{molar MgO} / (\text{molar MgO} + \text{FeO})$). The Mg# ranges between 0.11 – 0.86 in the stratigraphy, with the lowest Mg# recorded in the magnetite gabbro of the sampled UZ at 226.74 m and the highest Mg# recorded in

the pyroxenite of the sampled LCZ at 4991.09 m. High Mg#s are observed in the sampled rocks of the Upper Critical (0.38 – 0.80) and Main (0.43 – 0.75) Zones, with lower Mg#s observed in the chromitites of the sampled CZ and rocks of the UZ (0.11 – 0.51).

Mg# decreases throughout the sampled Upper and Upper Main Zones, which attests to fractionation being the dominant petrogenetic process within these zones. The relatively constant Mg# throughout the sampled Main and Upper Critical Zones may be suggestive of continued replenishment of the magma chamber by more primitive melts over this interval.

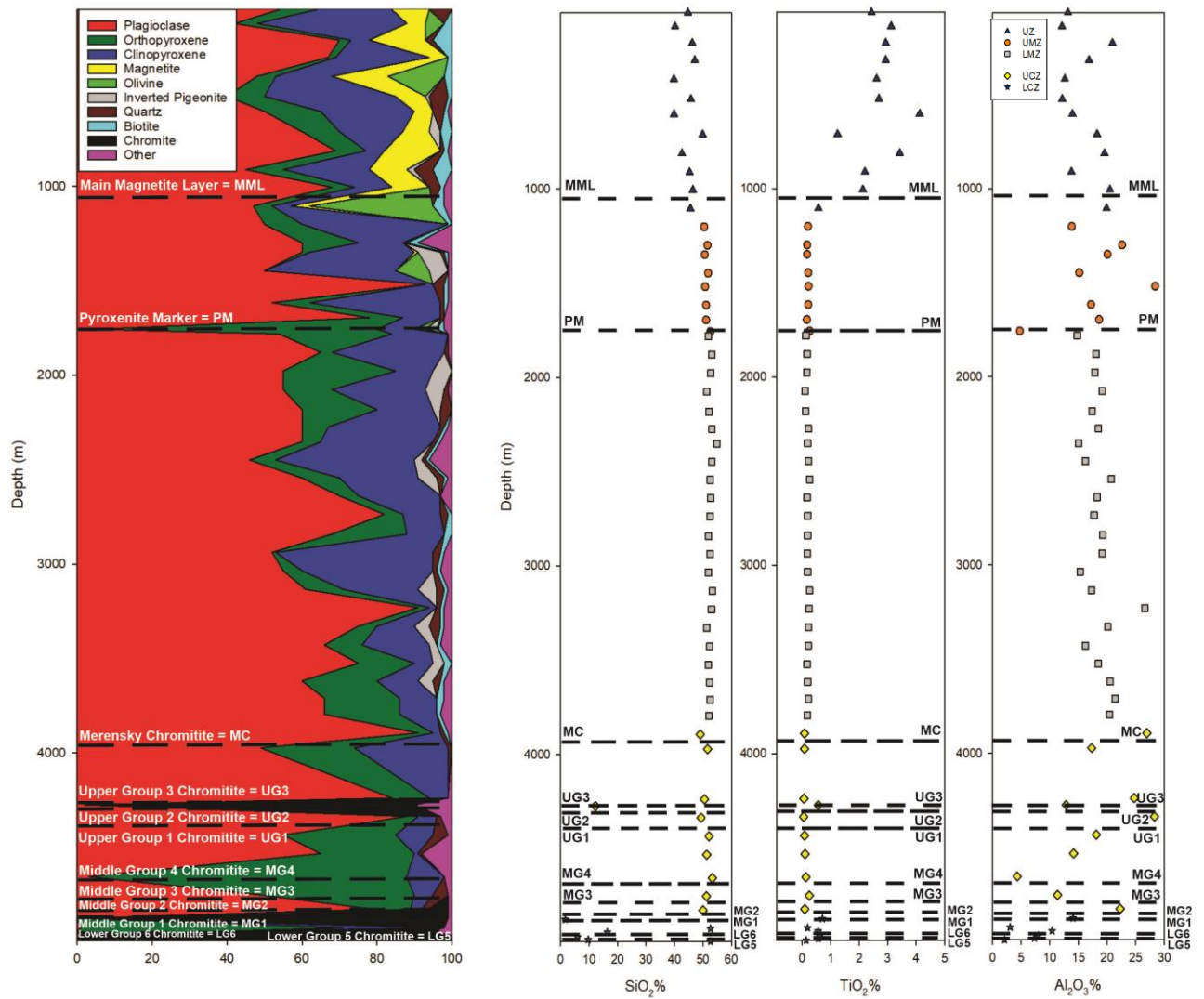


Figure 23: Variation of whole-rock major elements with depth across the studied interval.

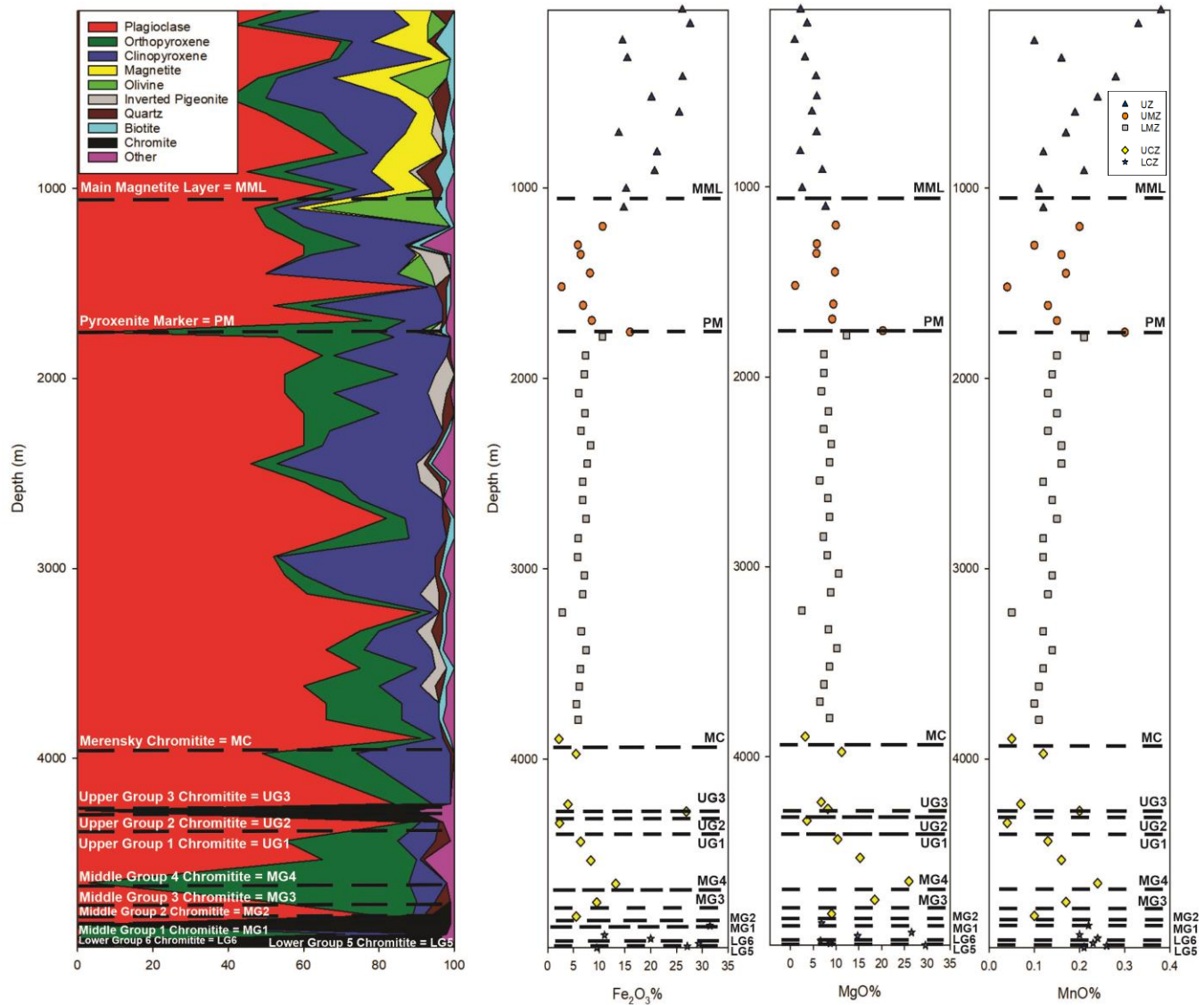


Figure 23: (Continued).

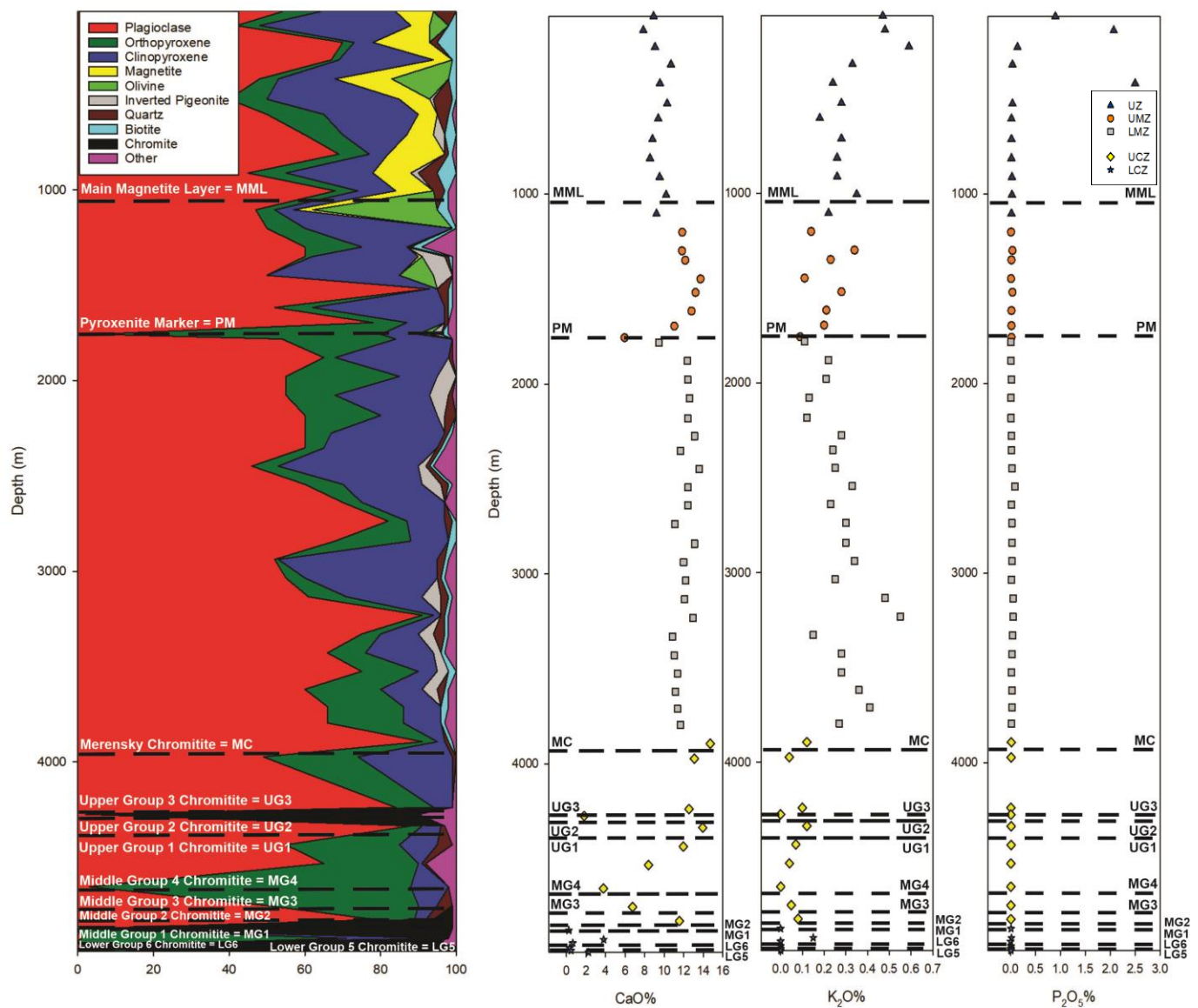


Figure 23: (Continued).

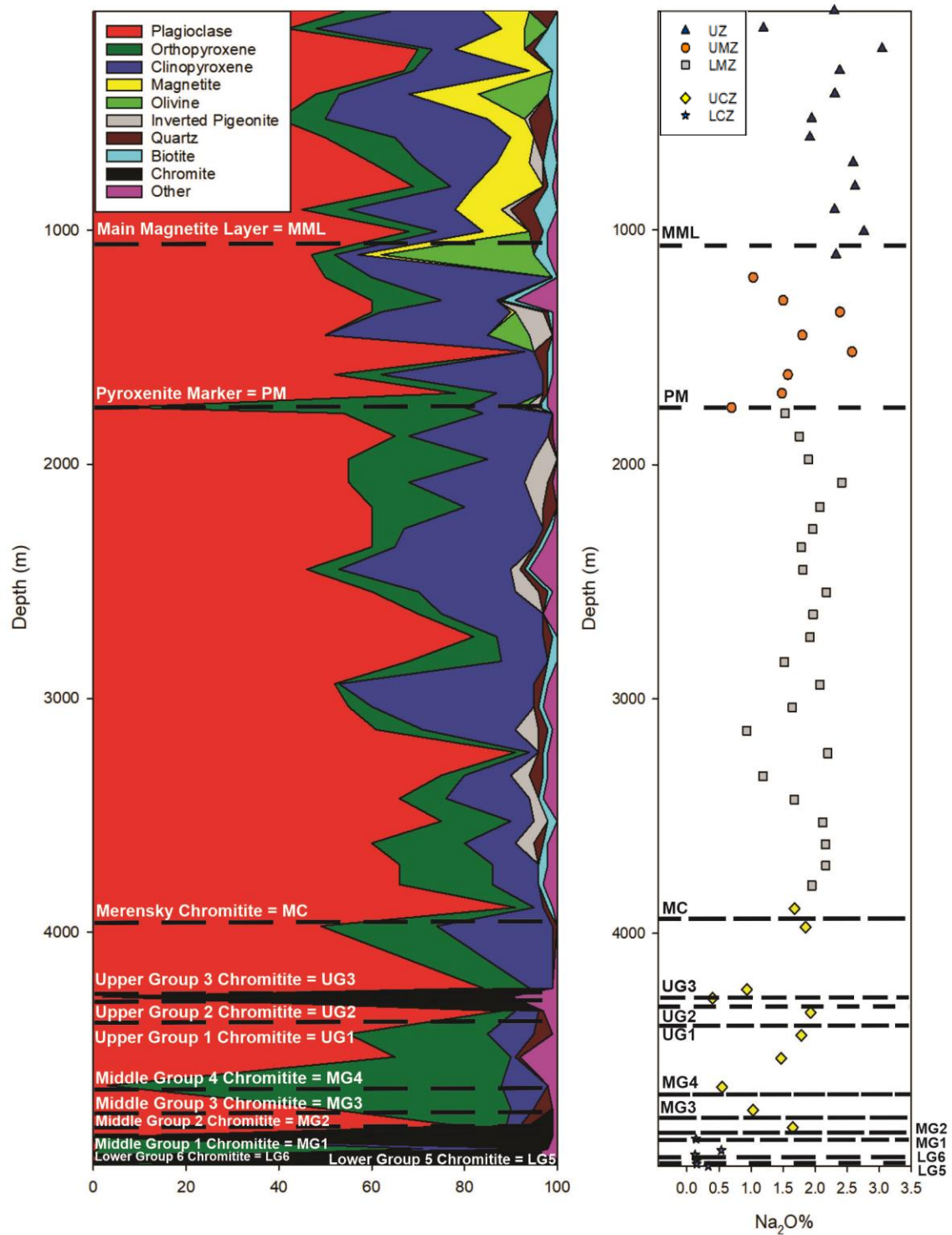


Figure 23: (Continued)

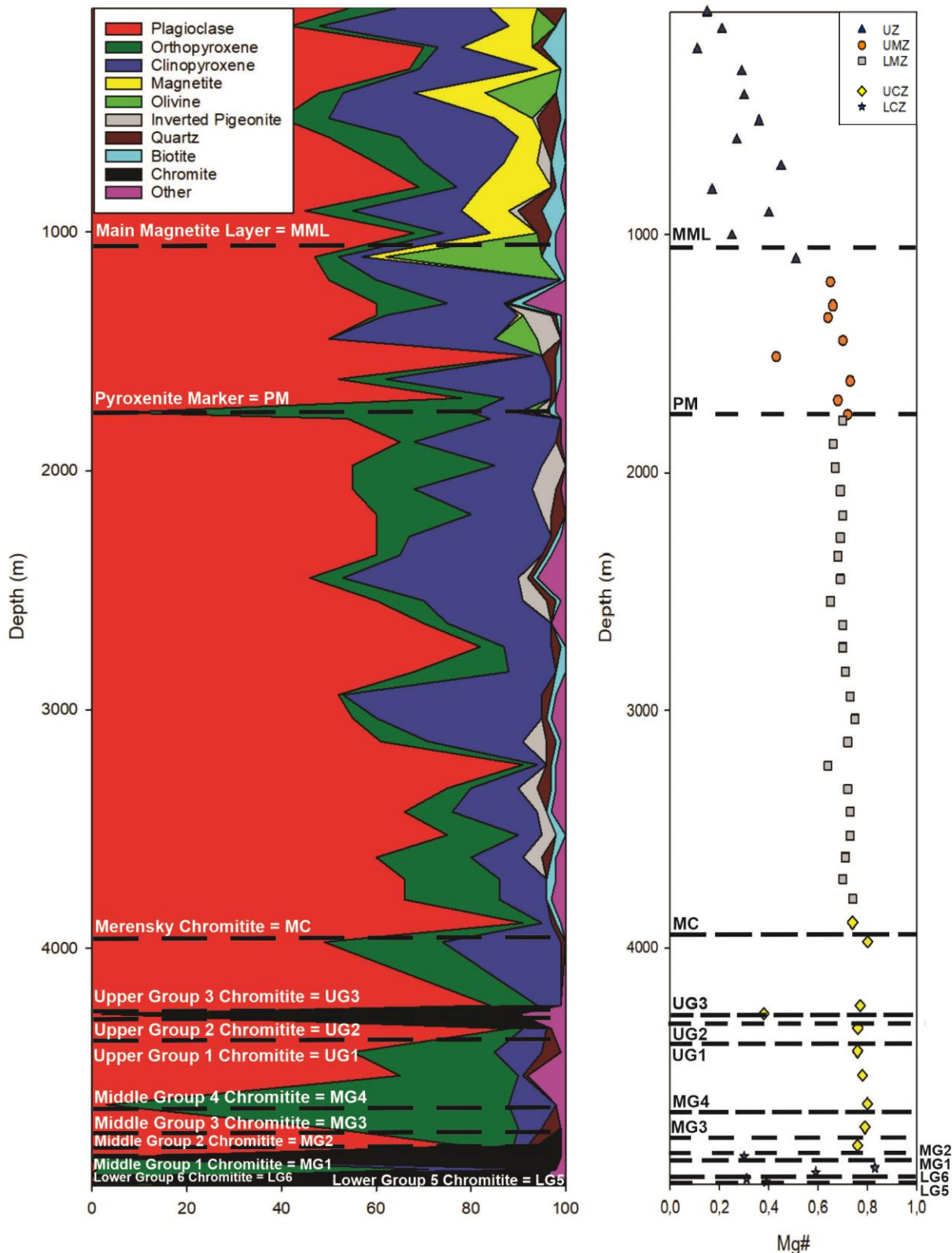


Figure 24: Variation of whole-rock Mg# with depth compared to variations in the modal mineralogical composition.

3.2.2 Whole-rock trace element geochemistry

The whole-rock trace element data were used to prepare binary variation diagrams (Figure 25) and Figure 26 shows the variation of trace element concentrations with depth across the studied stratigraphic interval. For binary variation diagrams, the trace elements were plotted against MgO, which is commonly used as a differentiation index since it is strongly compatible. Sc exhibits a positive correlation with MgO, ranging from 8 to 44 ppm. The highest Sc value was recorded in the PM from the MZ at 1 757.02 m while the lowest value was recorded in the chromitite from the sampled LCZ at 4 968.64 m. The average Sc value is 23.9 ppm.

V shows limited variation against MgO, with high contents recorded only in rocks from the sampled UZ and chromitites from the sampled CZ. The high concentration in the former is because of the presence of magnetite in the samples while the high concentration in the latter is caused by the presence of chromite in the samples. V contents range between 9 - 2369 ppm. The highest concentration was recorded in chromitite from the sampled UCZ, at a depth of 4 274.20 m, while the lowest value was recorded in the anorthosite from the sampled UCZ at 4 335.85 m. The average V content is 313.72 ppm.

Cr shows limited variation with MgO, with high contents recorded only in the rocks from the sampled CZ. The high concentrations of Cr in the two stratigraphic zones are the result of the presence of chromite. Cr values range between 7 – 8038 ppm, with the highest value occurring in the pyroxenite from the sampled LCZ at 4 991.09 m and the lowest value in the gabbronorite (711.43 m) and mottled anorthosite (1 519.05 m) from the sampled Upper and Upper Main Zones, respectively. Cr values average 581.92 ppm for the entire sample suite.

Co exhibits positive correlation with MgO with values ranging from 2 to 112 ppm. The highest values were mostly recorded in the sampled UZ, which might be the result of the incorporation of Co into magnetite. The highest value was recorded in the gabbronorite from the sampled UZ at 603.78 m while the lowest value was recorded in the mottled anorthosite from the sampled UMZ at 1 519.05 m. The average Co content is 45.65 ppm.

Ni shows positive correlation with MgO averaging at 221.48 ppm and values ranging between 7 – 884 ppm. High values were recorded in the sampled CZ, with the

highest value recorded in the chromitite at 4 875.72 m from the sampled LCZ. The lowest Ni value was recorded in the gabbronorite from the sampled UZ at 138.77 m.

Cu shows limited variation with MgO, ranging between 2 – 573 ppm. High values are recorded in the sampled UZ which might be an indication of the presence of sulphides. The highest value was recorded in the gabbronorite from the Upper Zone at 603.78 m, while the lowest value was recorded in the gabbronorite at 3 972.90 m from the UCZ. The average Cu content is 56.55 ppm.

Zn shows no correlation with MgO, ranging between 16 – 607 ppm. High values are observed in the sampled LCZ with the highest value recorded in the chromitite at 4 875.72 m. The lowest Zn value is recorded in the mottled anorthosite at 1 519.05 m from the UMZ. The average Zn value is 108.53 ppm.

Rb shows no correlation with MgO, and ranges from 2 to 16 ppm. This is indicative of the incompatible behaviour of Rb towards the constituted mineralogy in this study. The highest value was recorded in the gabbronorite at 3 134.33 m from the LMZ. The average Rb content was recorded as 6.26 ppm.

Sr exhibits a negative correlation with MgO, ranging from 4 to 449 ppm, while the average value for Sr is 244.24 ppm. The highest value was recorded in the magnetite gabbro at 226.74 m from the UZ while the lowest value was recorded in chromitites at 4 875.72 m and 4 942.93 m from the LCZ. High Sr concentrations tend to be confined to samples rich in plagioclase due to the element's affinity for plagioclase, hence the negative correlation with MgO.

Y shows no correlation with MgO and it averages 7.21 ppm. The lowest value is 1 ppm and the highest is 35 ppm. The former was recorded at 4 238.37 m in the gabbronorite from the UCZ while the latter was recorded at 65.66 m in the magnetite gabbronorite from the UZ.

Zr does not show any correlation with MgO, with a recorded average of 18.5 ppm. Zr ranges between 5 – 57 ppm, with the lowest value recorded in the gabbronorite from the UCZ at 3 972.90 m and the highest value recorded in the gabbronorite from the UZ at 138.77 m. The low contents of Zr are caused by the incompatible nature of Zr with the cumulus minerals in this study. Nb does not show any correlation with MgO and it has an average content of 2 ppm. The highest value is 8 ppm while the lowest

value is 1 ppm. The highest value was recorded in magnetite gabbronorite from the UZ at 65.66 m. Ba also shows no correlation with MgO and the concentrations range between 15 – 314 ppm. The highest value is recorded in the magnetite gabbronorite from the UZ at 65.66 m while the lowest value is recorded in the pyroxenite from the LCZ at 4 991.09 m. The average concentration for Ba is 97.32 ppm.

Pb shows no correlation with MgO and it ranges from 2 to 86 ppm. The lowest value is recorded in gabbro from the UZ at 318.47 m while the highest value is recorded in the chromitite from the LCZ at 4 968.64 m. The average Pb concentration recorded was 19.92 ppm.

The following whole-rock trace elements are not shown on the binary variation diagrams in Figure 25, as the majority of samples had values below detection as indicated in Appendix A2. As recorded a maximum value of 20 ppm, which was recorded in the gabbronorite from the UZ at 138.77 m. The lowest value of As was below the detection limit of 1 ppm. Th recorded a maximum value of 10 ppm, which was obtained in the gabbronorite from the UZ at 138.77 m. The lowest Th value measured below the detection limit of 3 ppm. U returned the highest value as 4 ppm and the lowest value was below the detection limit of 3 ppm.

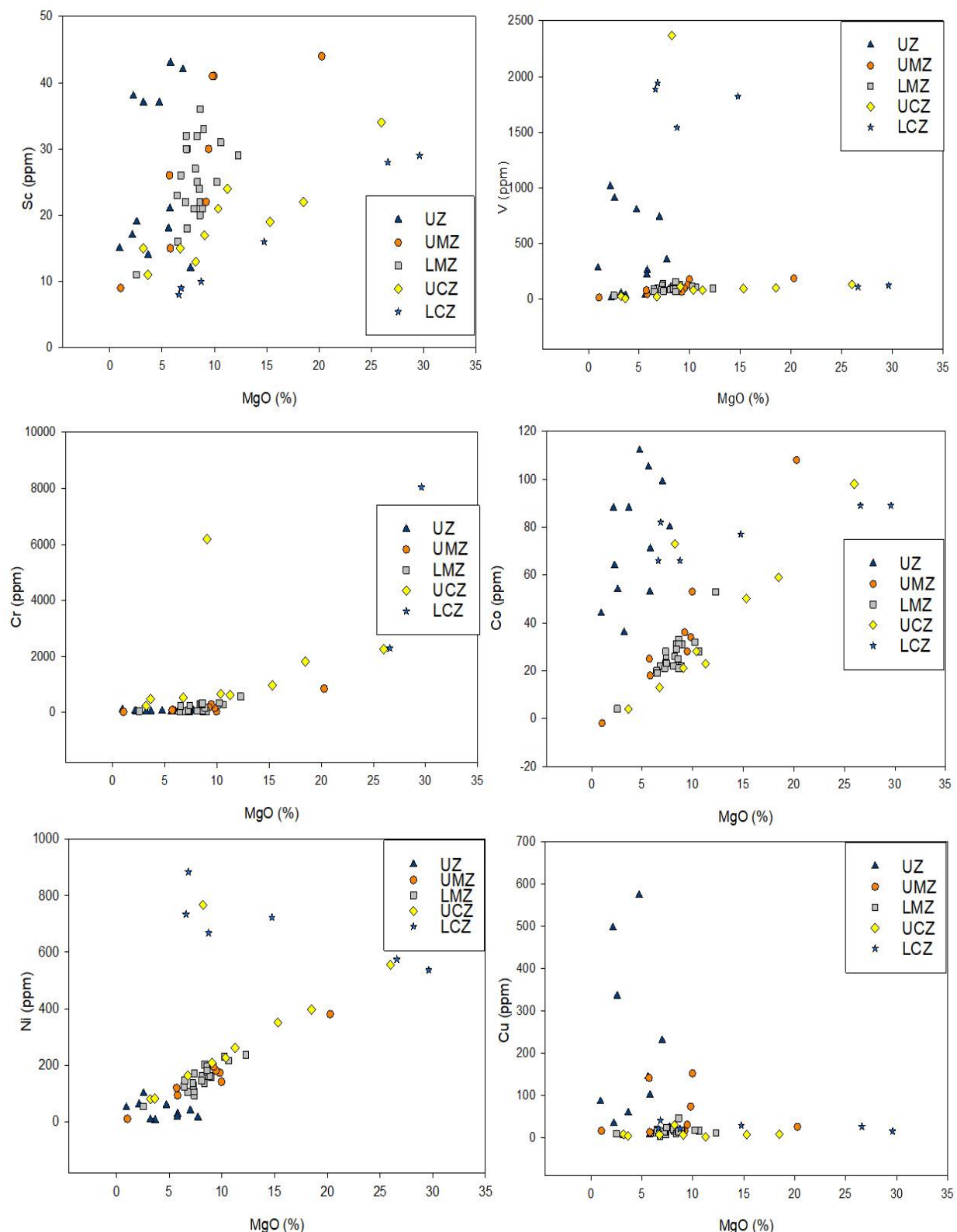


Figure 25: Binary variation diagrams of selected whole-rock trace elements vs. MgO.

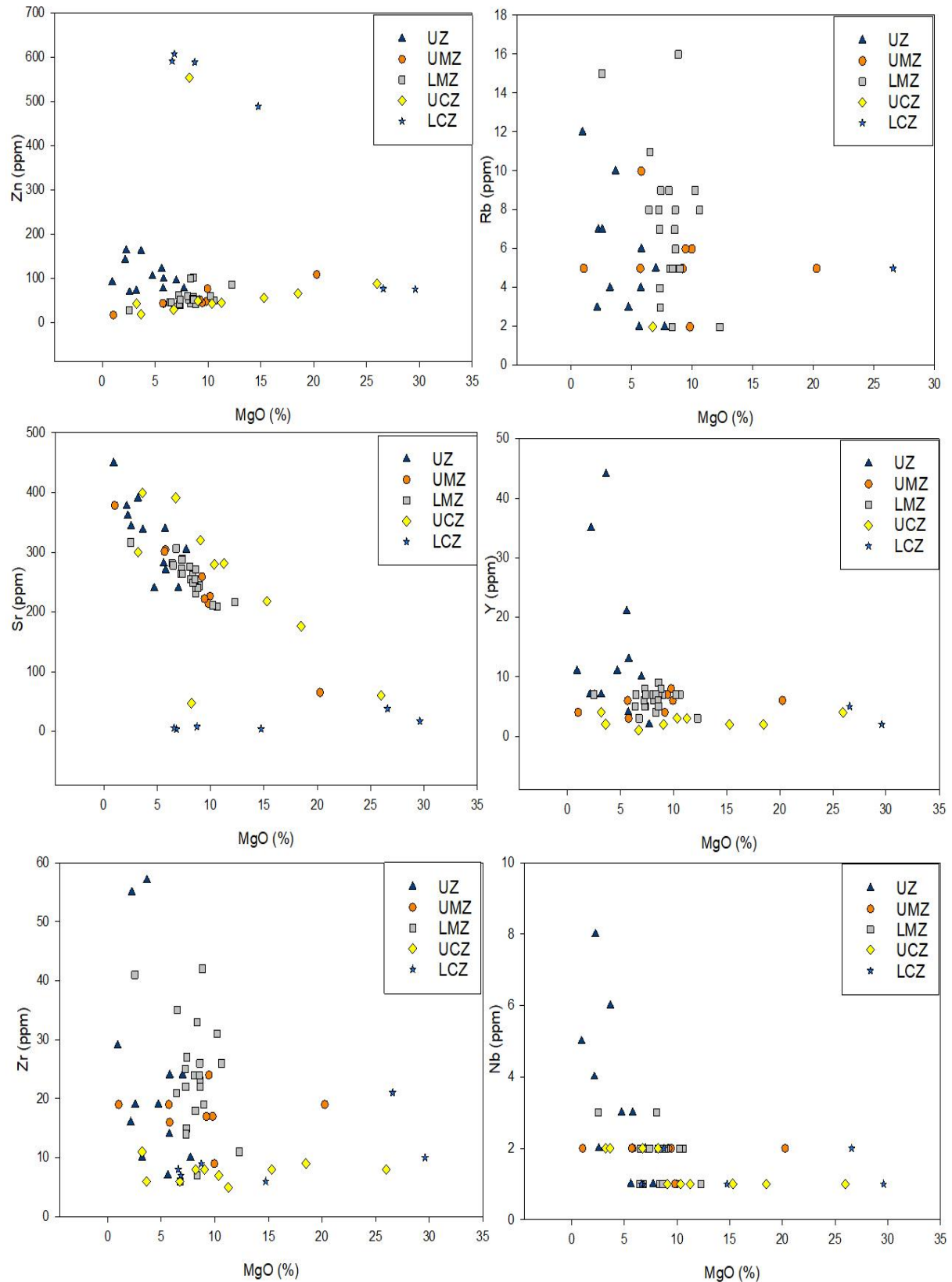


Figure 25: (Continued).

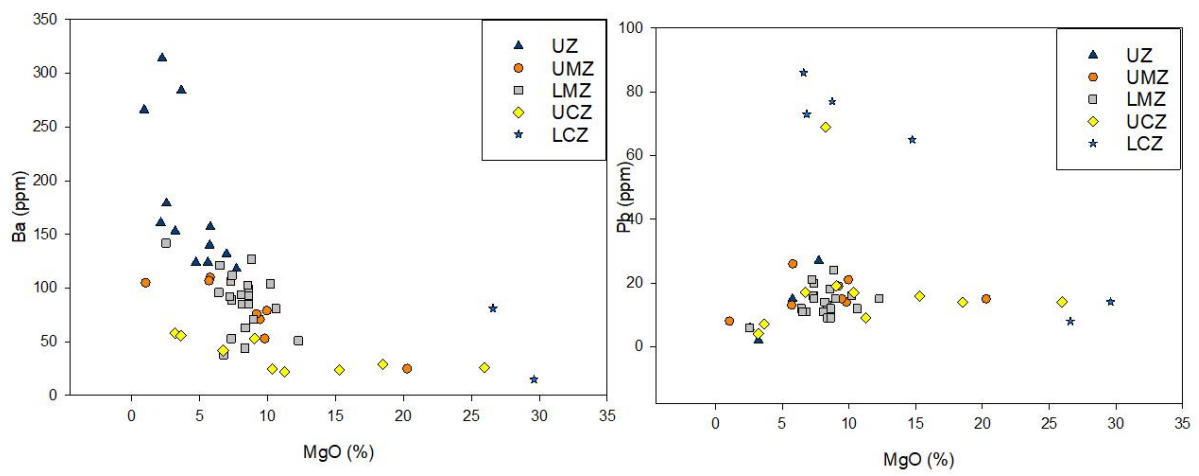


Figure 25: (Continued)

The plots of whole-rock trace elements vs depth show variability across the entire stratigraphy, from the sampled UZ to the sampled LCZ (Figure 26). Sc shows significant variation across the stratigraphy, with high concentrations occurring where ferromagnesian minerals like olivine and pyroxene are abundant. At approximately 2543.73 m in the lower parts of the LMZ, there is a decrease in the Sc concentration as the content of plagioclase increases.

V does not show much variability in the sampled MZ and sampled UCZ. In the latter, the V concentration is elevated at 4 274.20 m because of the abundance of chromite in the chromitite. The lower reaches of the sampled UZ recorded an increase in V, which is attributed to the presence of magnetite. Cr does not show systematic variation across the stratigraphy, except for localised increases in the lower and upper parts of the sampled Upper Critical and Lower Critical Zones, respectively. These are attributed to the presence of significant concentrations of chromite associated with chromitite layers.

Co is fairly constant in the sampled MZ except at the sampled Pyroxenite Marker. High Co concentrations are observed in the sampled Upper and Critical Zones. Ni is rather constant through the sampled UZ to the sampled LMZ, while high concentrations of Ni are observed in the sampled CZ. Cu is rather constant throughout the entire stratigraphy except in the sampled UZ where some samples display elevated Cu concentrations. Zn also displays rather constant concentrations throughout the stratigraphy, with elevated concentrations encountered in the chromitites of the sampled CZ.

Rb is depleted in the sampled CZ with concentrations below the detection limit. Rb shows significant variability throughout the stratigraphy, with high concentrations recorded in the lower parts of the sampled LMZ. There is a decrease in the Rb concentration just below the Pyroxenite Marker.

Sr concentrations are high throughout much of the stratigraphy due to the dominance of the mineral plagioclase. Sr is fairly constant in the sampled LMZ with more variability exhibited in the sampled Upper, Upper Main and Upper Critical Zones. The chromitites and pyroxenites in the sampled CZ recorded low Sr concentrations due to the paucity of the mineral plagioclase. The sampled Pyroxenite Marker similarly showed a low abundance of Sr.

Y and Nb do not show any systematic variation throughout the stratigraphy, except an increase in their concentrations in the sampled UZ which might be attributed to the presence of magnetite. Zr shows variability throughout the stratigraphy, with high concentrations recorded in the first 138.77 m of the UZ. Zr is low in the sampled CZ, with a significant increase recorded at the boundary between the CZ and MZ samples. This is followed by a stepwise decrease in Zr content throughout the sampled LMZ. The sampled UMZ and UZ show rather limited variability in Zr, apart from the top several hundred metres of the sampled UZ, which shows a trend of increasing Zr content.

Ba shows variability throughout the entire stratigraphy, with elevated concentrations in the sampled UZ. There is a decreasing trend commencing from the sampled UZ until the upper parts of the sampled LMZ. There is variation in the lower parts of the sampled LMZ which is followed by a decrease of Ba concentrations in the sampled CZ, with limited variation. Pb is fairly constant throughout the entire stratigraphy, with the exception of elevated concentrations close to the level of chromitite layers in the sampled CZ. Pb concentrations are low within the sampled UZ.

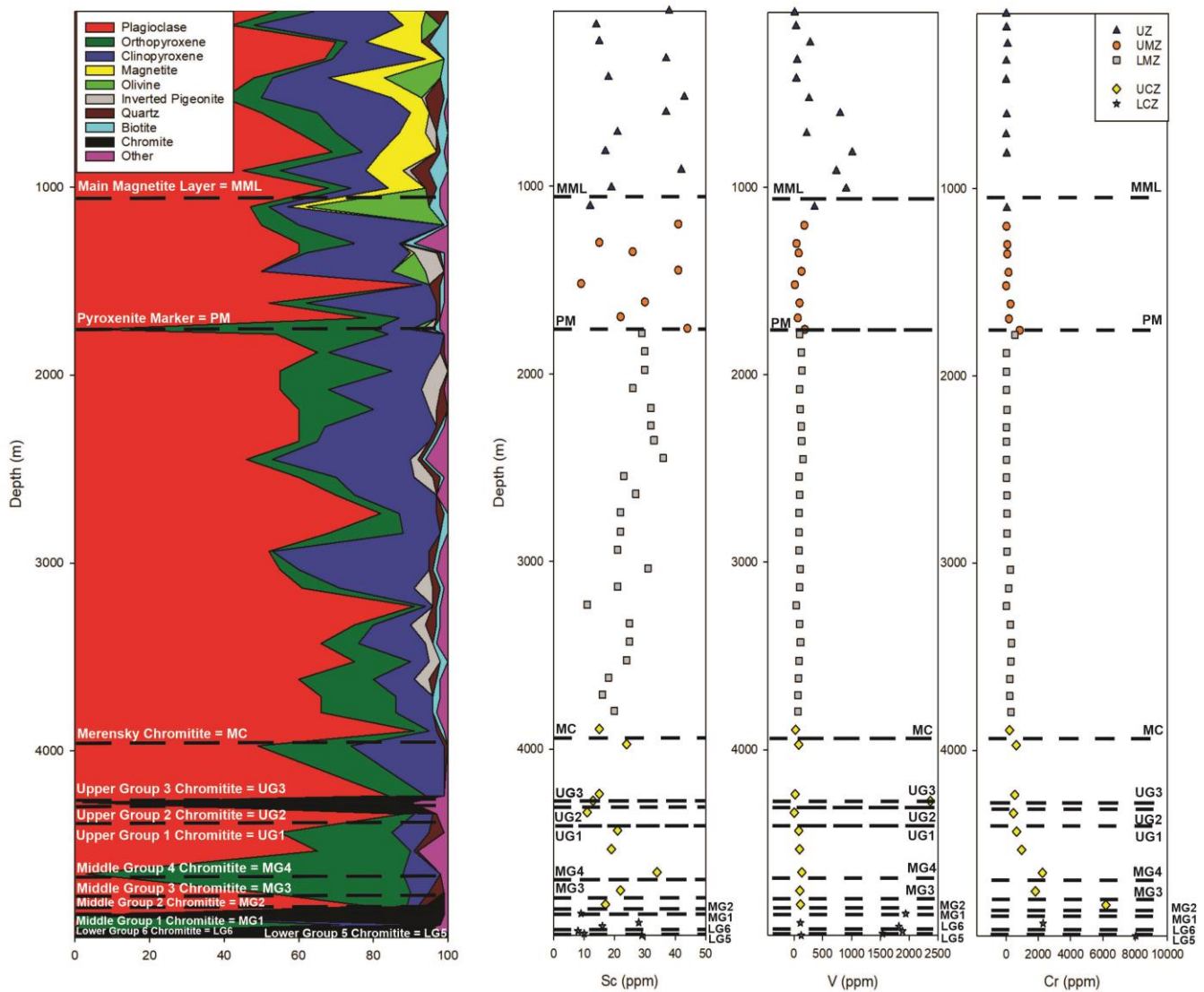


Figure 26: Variation in whole-rock trace elements with depth, compared with modal mineralogical variations.

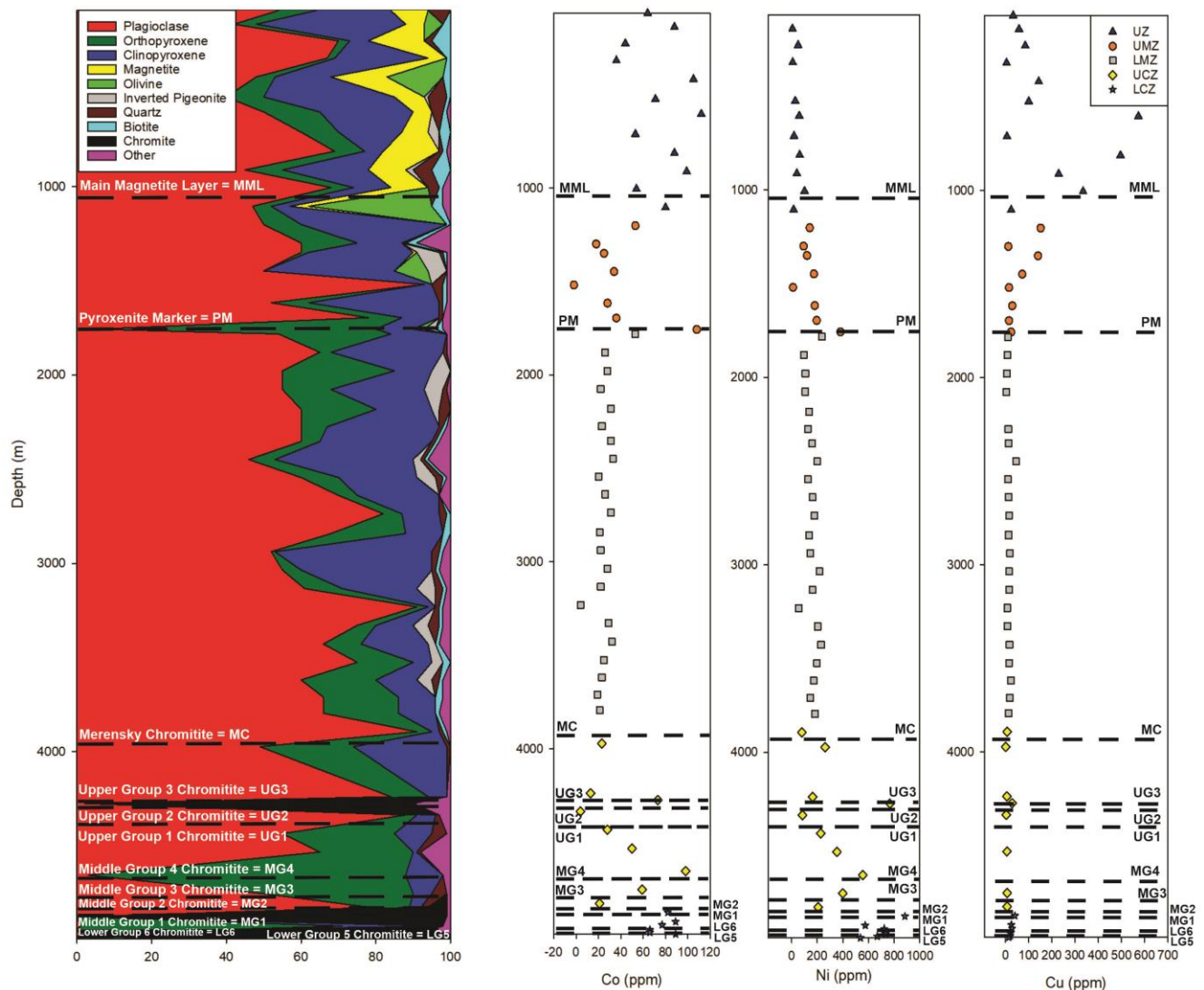


Figure 26: (Continued).

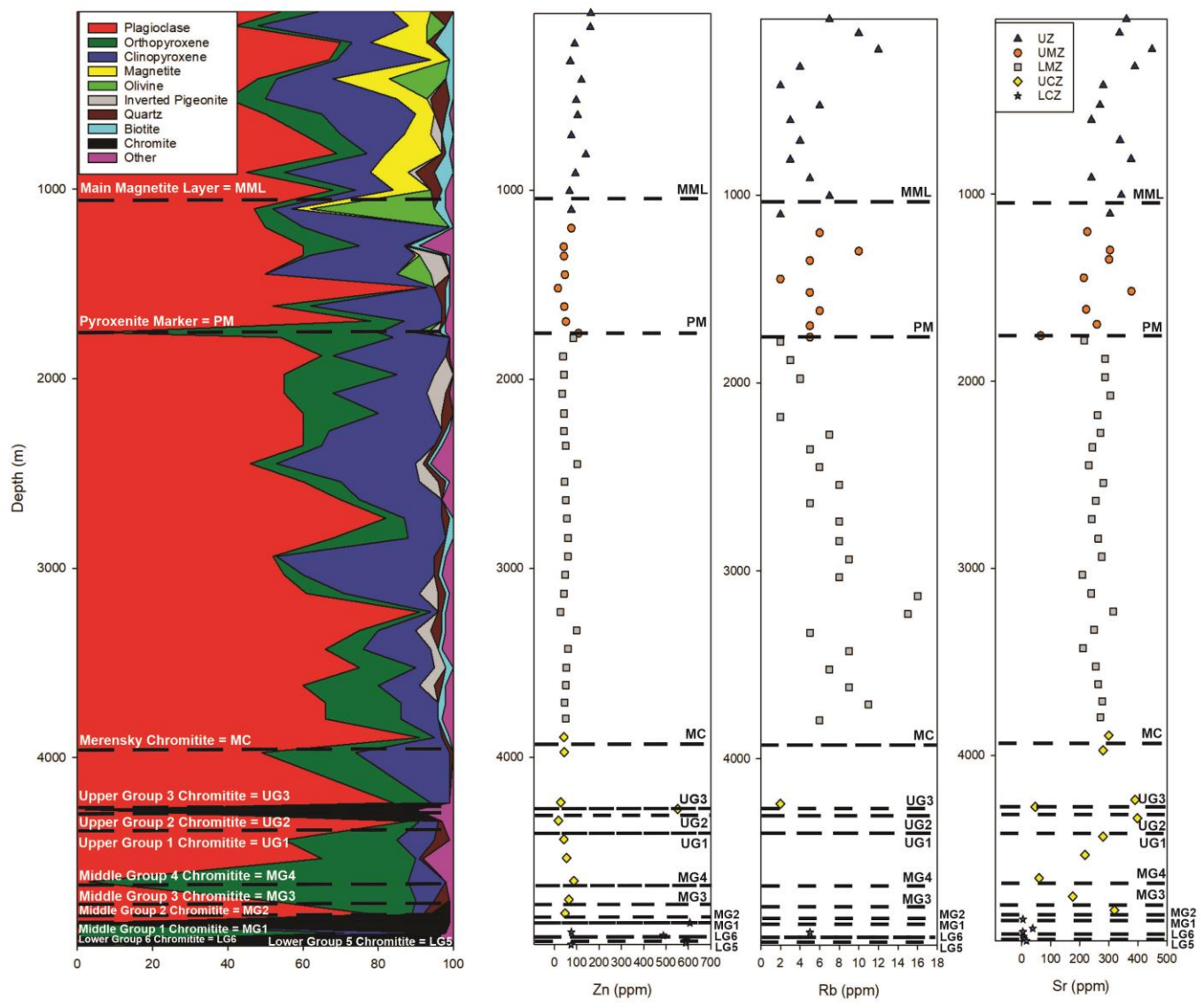


Figure 26: (Continued).

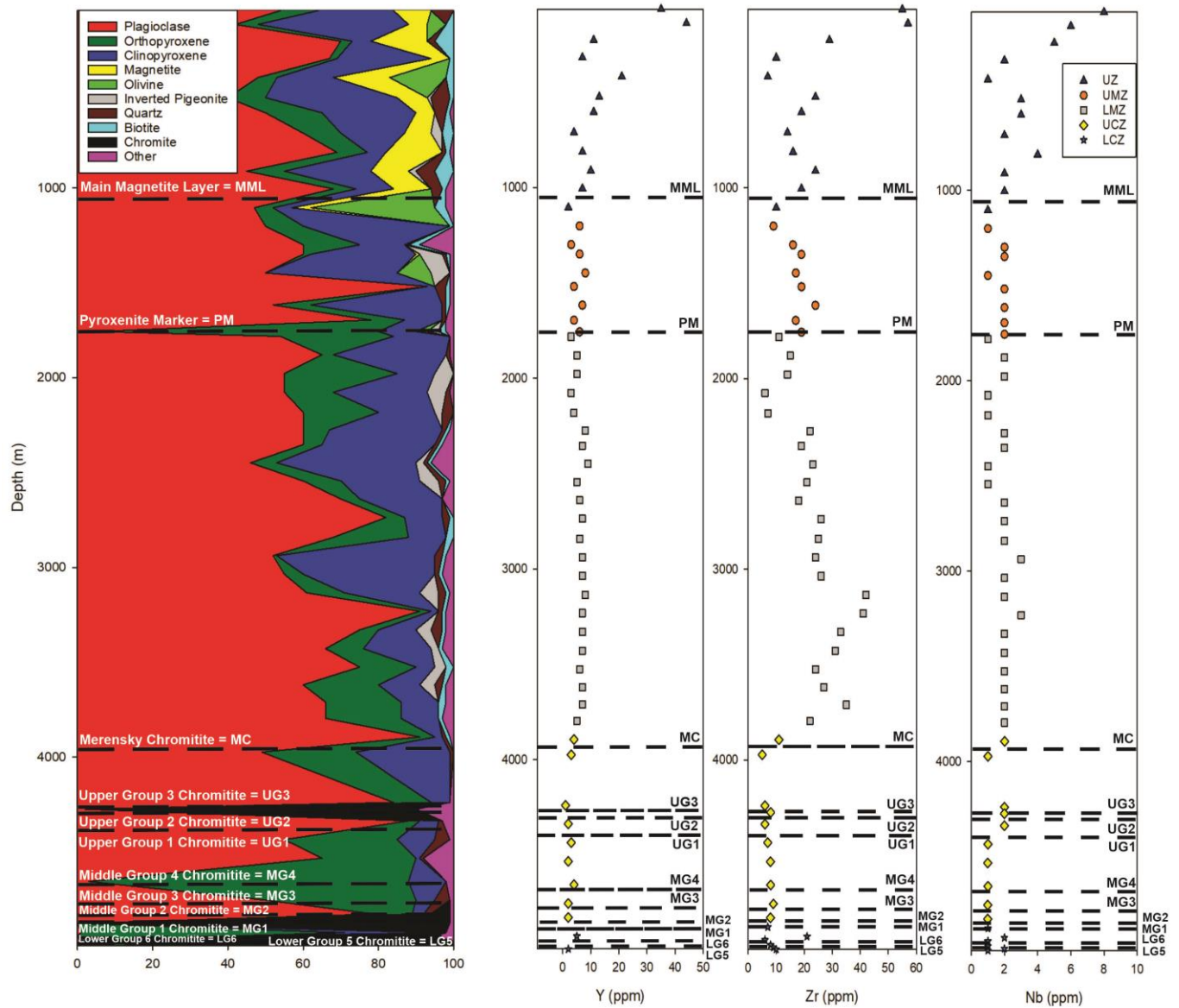


Figure 26: (Continued).

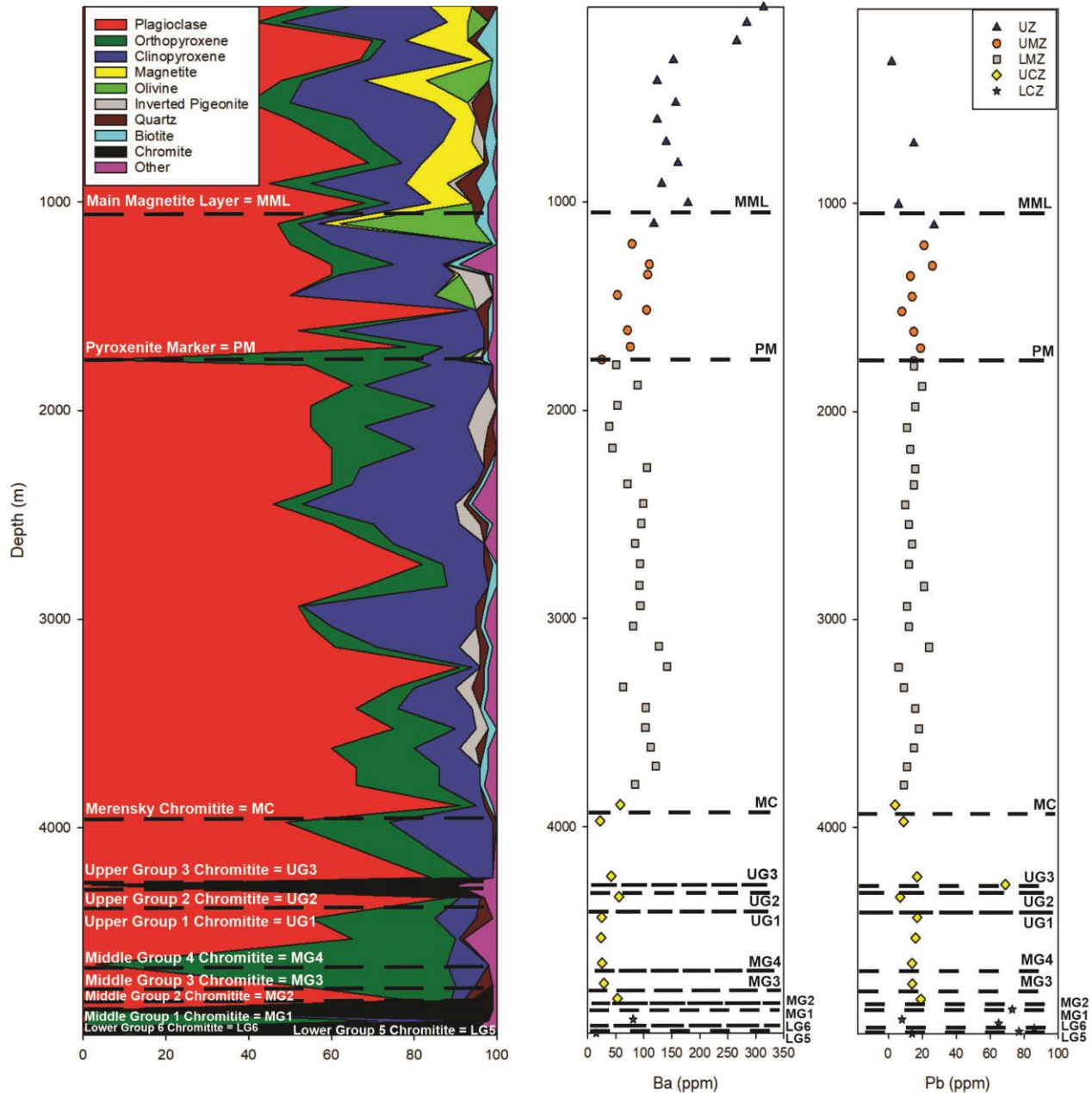


Figure 26: (Continued).

3.3 Plagioclase mineral chemistry

Visually unaltered plagioclase crystals were analysed in the samples to produce the in-situ major element geochemical data, which are presented in Appendix B. Mineral formulae calculated on the basis of average plagioclase compositions at a particular depth are presented in Electronic Appendix 2. Plagioclase compositions are presented in the feldspar ternary diagram in Figure 27.

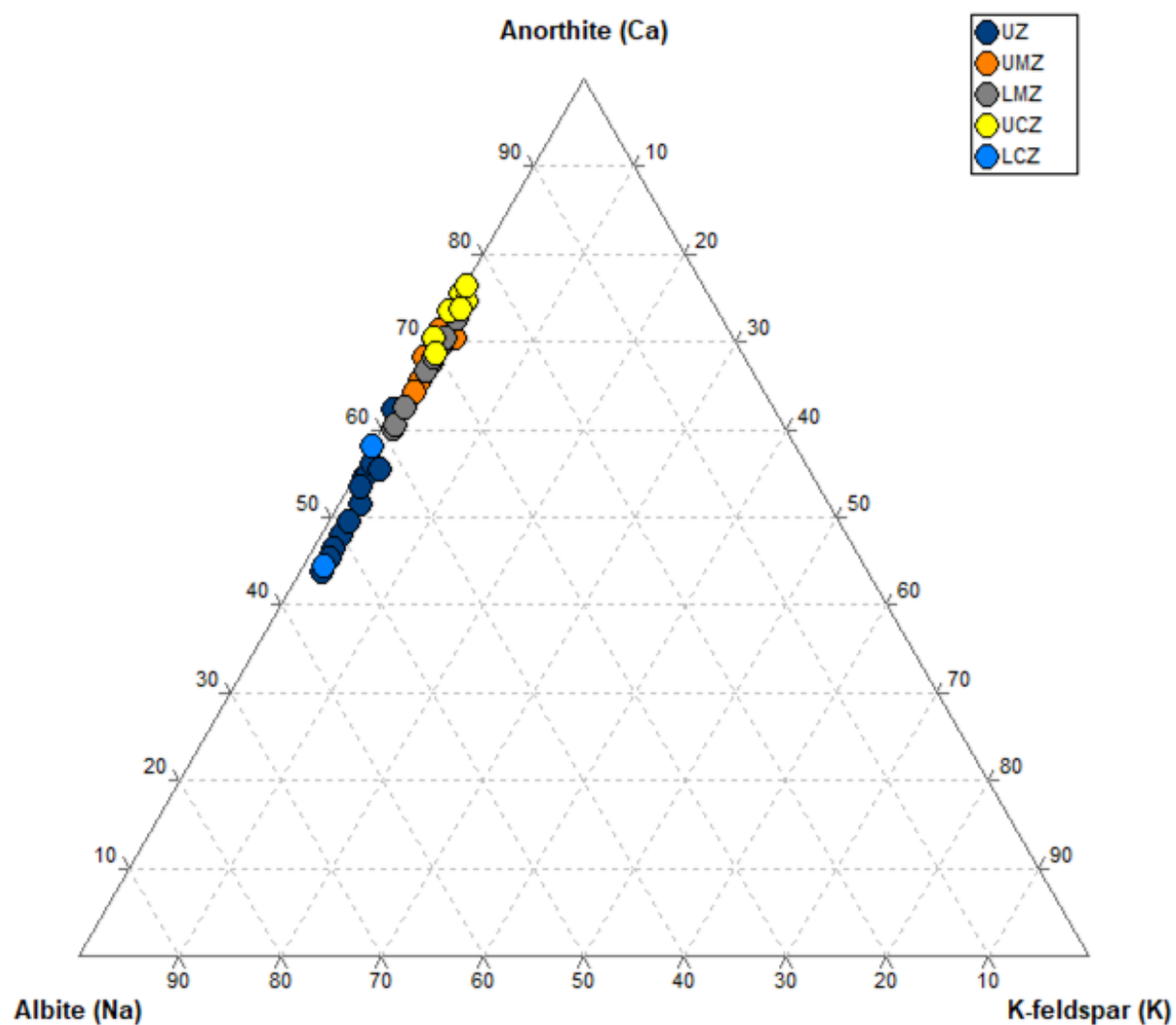


Figure 27: Plagioclase compositions encountered in this study presented in the feldspar ternary diagram.

The minimum and maximum values of the calculated An% of plagioclase encountered in this study are 40.20% and 77.00%, respectively. The variation in An% with depth is depicted in Figure 28.

The An% of plagioclase in the sampled UZ ranges between 40.20% and 72.97% (the latter value appearing to be an outlier), with an average of $49.64 \pm 4.90\%$. The An% of plagioclase in the sampled UMZ recorded an average of $66.91 \pm 4.49\%$, varying between 59.34% and 74.78%. The sampled LMZ plagioclase recorded an average An% of $65.71 \pm 4.51\%$, ranging between 56.21% and 74.67%. The sampled UCZ plagioclase recorded an average An% of $72.52 \pm 3.00\%$, ranging between 65.86% and 77.00% while the sampled LCZ plagioclase recorded an average An% of $51.04 \pm 7.76\%$, ranging between 38.57% and 59.65%.

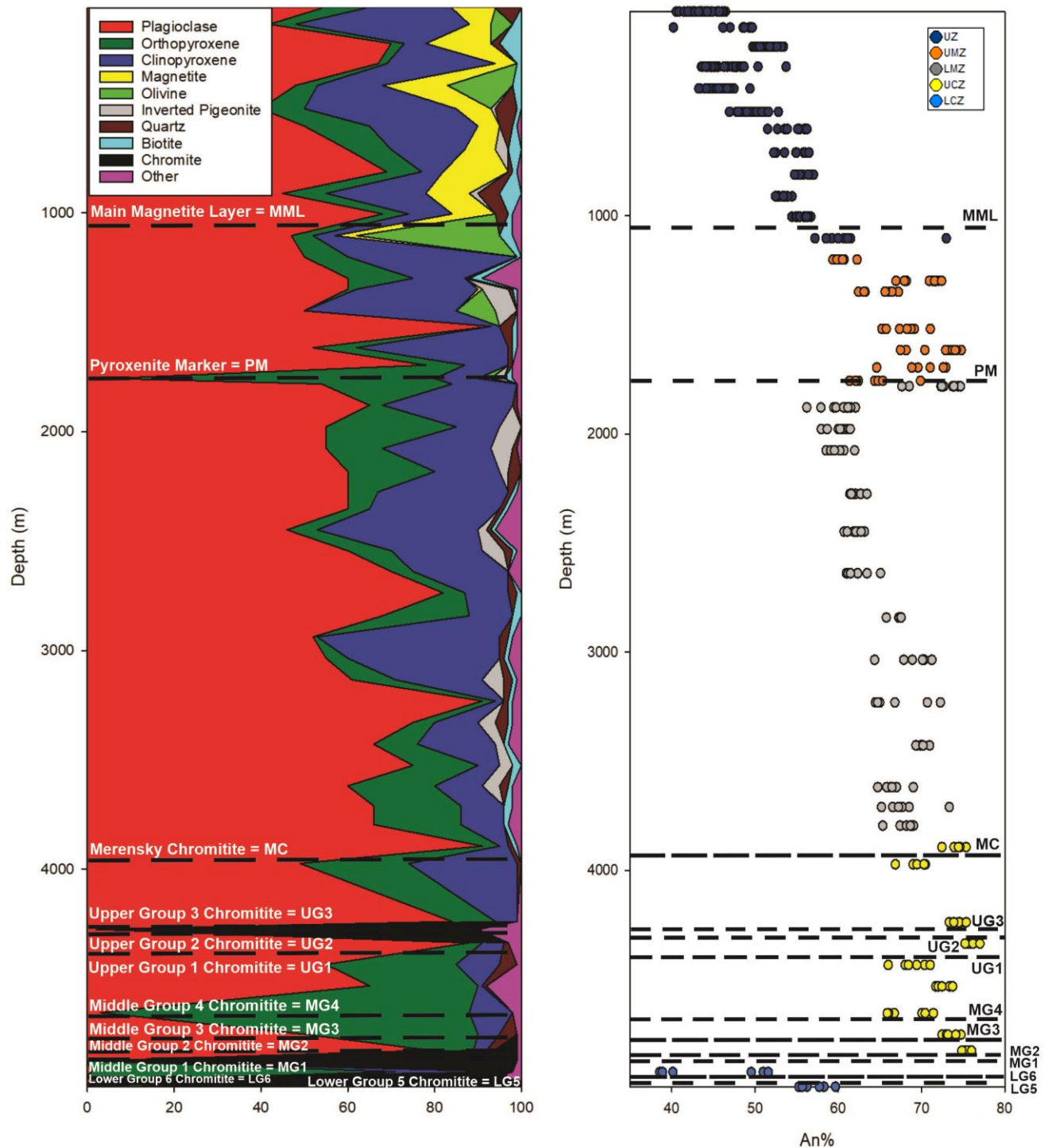


Figure 28: Variation of plagioclase anorthite content (An%) with depth compared to variations in the modal mineralogical composition.

In general, there is a decrease in An% from the UCZ to the UZ in the studied rock samples, coupled with numerous reversals in An% across the stratigraphy (Figure 29). In the upper parts of the LCZ, from 4 991.09 m to 4 924.39 m, there is a recorded decrease in An% from 57.14% to 44.93%. The decrease is followed by a sharp reversal in An% from the LCZ to the lower parts of the UCZ, reflecting the change from intercumulus plagioclase in the LCZ to cumulus plagioclase in the UCZ. This increase is from 44.93% to 75.53% at the depth of 4 924.39 m to 4 826.62 m. Subsequently, a decrease in An% is recorded from the depth of 4 826.62 m to 4 654.76 m, with an average value of 72.44%.

From 4 654.76 m to 4 532.20 m, the An% increases from 68.42% to 72.60%. The increase in An% is followed by another decrease recorded from 4 532.20 m to 4 434.09 m with values from 72.60% to 68.86%. From 4 434.09 m to 4 335.85 m, there is an increase in An% from 68.86% to 75.89%. Another decrease is observed from a depth of 4 335.85 m to 3 972.90 m, with an average of 73.22%. From 3 972.90 m to 3 893.44 m, an increase in An% is recorded, with values from 69.40% to 74.21%. From 3 893.44 m to 3 795.28 m, a decrease in An% is recorded, followed by a constant An% between 3 795.28 m and 3 710.10 m. There is another decrease in An% from 68.07% to 66.55% from the depth of 3 710.10 m to 3 618.98 m, which is followed by an increase from 66.55% to 69.93% from the depth of 3 618.98 m to 3 427.93 m.

There is a decrease in An% that is observed from 3 427.93 m to 3 230.89 m, recording values from 69.93% to 67.31%. This decrease is followed by an increase in An% from 67.31% to 69.22%, from the depth of 3 230.89 m to 3 035.77 m. From 3 035.77 m to 2 639.06 m, there is a decrease in An%, with an average of 66.24%. An% remains constant from 2 639.06 m to 2 274.98 m, with an average value of 62.19%. A decrease in An% is recorded from the depth of 2 274.98 m to 2 076.38 m, with the An% values from 62.13% to 60.00%. An% remained constant from 2 076.38 m to 1 879.26 m, with an average value of 60.04%.

From 1 879.26 m to 1 782.05 m, which is slightly below the Pyroxenite Marker, there is a significant increase in the An%, from the value of 59.95% to 72.24%. From 1 782.05 m to the Pyroxenite Marker, which is at the depth of 1 757.02 m, there is a decrease in An%. This decrease in An% ranges from 72.24% to 63.96%. From the

Pyroxenite Marker to the lower parts of the UMZ at the depth of 1 616.47m, there is an increase in An% with an average value of 68.73%. From 1 616.47 m to 1 349.35 m, there is a decrease in An% with an average value of 68.37%. There is an increase in An% from the depth of 1 349.35 m to 1 299.49 m, with values from 65.12% to 70.32%. Subsequent to this increase, a decrease in An% is recorded from 70.32% to 60.42% at the depths of 1 299.49 m and 1 201.54 m respectively. An increase of An% is recorded from 1 201.54 m UMZ to 1 104.46 m in the UZ, with values from 60.42% to 61.39%, From depth 1 104.46 m to 911.78 m, there is a decrease in An% with an average value of 56.75%.

From 911.78 m to 812.53 m, there is an increase in An% from the value of 53.26% to 55.88%. There is a decrease in An% from 812.53 m to 418.31 m, with an average value of 52.07%. From 418.31 m to 226.74 m, there is an increase in An%, with an average value of 47.83%. Subsequent to this increase, a decrease in An% is recorded from 226.74 m to 65.66 m, with an average value of 47.47%.

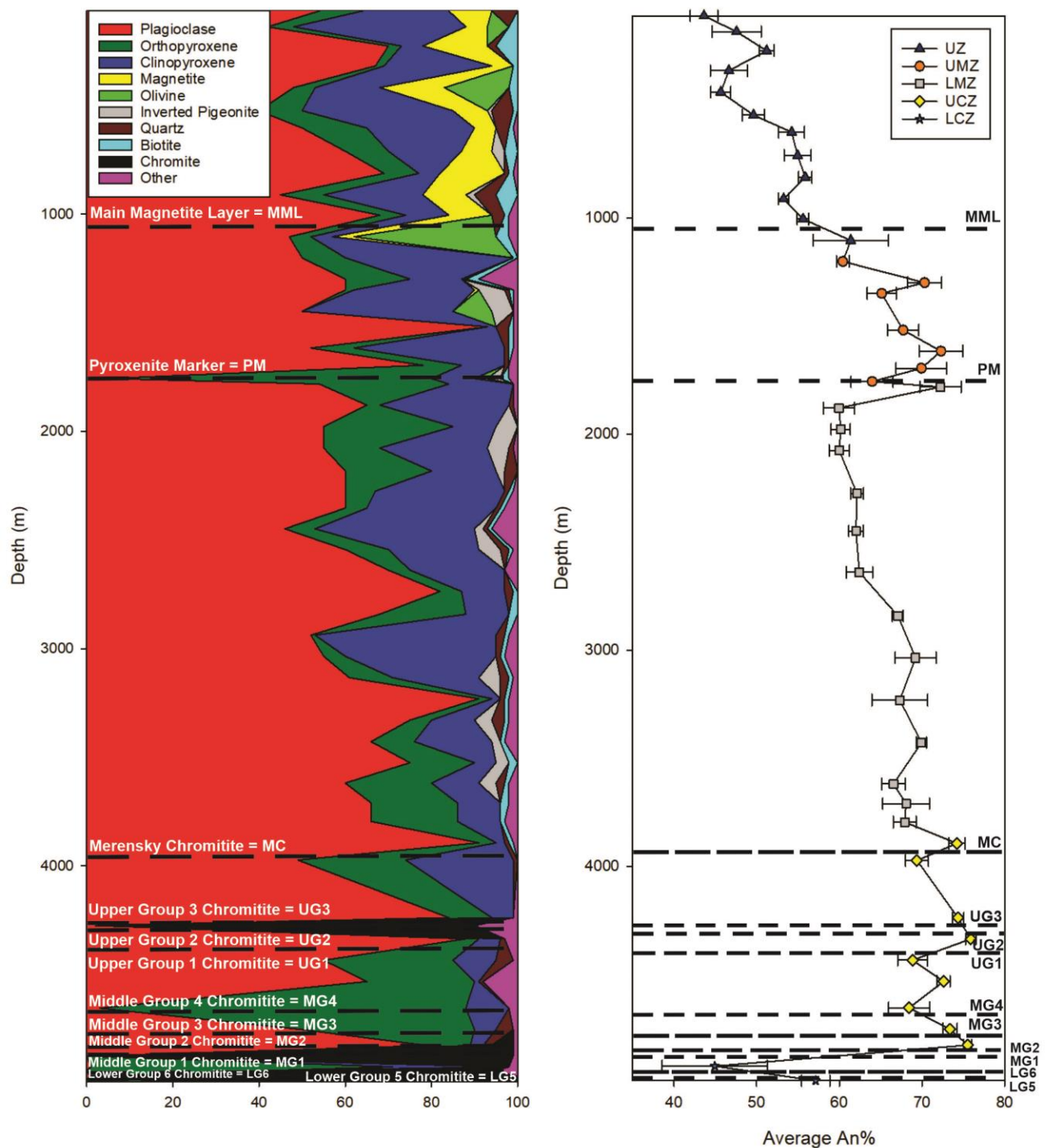


Figure 29: The average An content (An%) of samples versus depth, with error bars representing standard deviation, and a modal mineralogy graph showing varying mineral components in the samples.

3.4 Sr-isotopic compositions of plagioclase

The strontium isotopic data collected on plagioclase crystals are given in Appendix C. Initial $^{87}\text{Sr}/^{86}\text{Sr}$ ratios were calculated using an age of 2054.4 Ma (Scoates and Friedman, 2008), with a decay constant of $1.39 \times 10^{-11} \text{ y}^{-1}$ (Nebel *et al.*, 2011). The radioactive parent isotope (^{87}Rb) decays to the radiogenic daughter isotope (^{87}Sr) by beta decay, $^{87}\text{Rb} - \beta \rightarrow ^{87}\text{Sr}$. As the mass spectrometer is limited in measuring absolute concentrations of individual isotope species, the abundance of both parent and daughter isotopes are expressed relative to an isotope whose natural abundance does not change with time, such as ^{86}Sr . In age calculations, two isotopic ratios, $R = \text{parent/stable}$ ($^{87}\text{Rb}/^{86}\text{Sr}$) and $I = \text{daughter/stable}$ ($^{87}\text{Sr}/^{86}\text{Sr}$) are required. Given that, the $^{87}\text{Sr}/^{86}\text{Sr}$ ratio is measured directly on the mass spectrometer with corrections applied as per the methodology section above while $^{87}\text{Rb}/^{86}\text{Sr}$ is calculated by monitoring the 85/88 signal and multiplying that by $((87\text{Rb}/85\text{Rb})/0.1194)$.

The initial $^{87}\text{Sr}/^{86}\text{Sr}$ composition of individual spots is plotted against depth in Figure 30. The standard errors for $^{87}\text{Sr}/^{86}\text{Sr}$ and $^{87}\text{Rb}/^{86}\text{Sr}$ were propagated and multiplied by 2 to get the 2 standard error (2SE). The propagation formulas are: $\text{SE}(x+y) = \sqrt{\text{SE}(x)^2 + \text{SE}(y)^2}$; $\text{SE}(x-y) = \sqrt{\text{SE}(x)^2 + \text{SE}(y)^2}$. This error was used to observe the variability between samples.

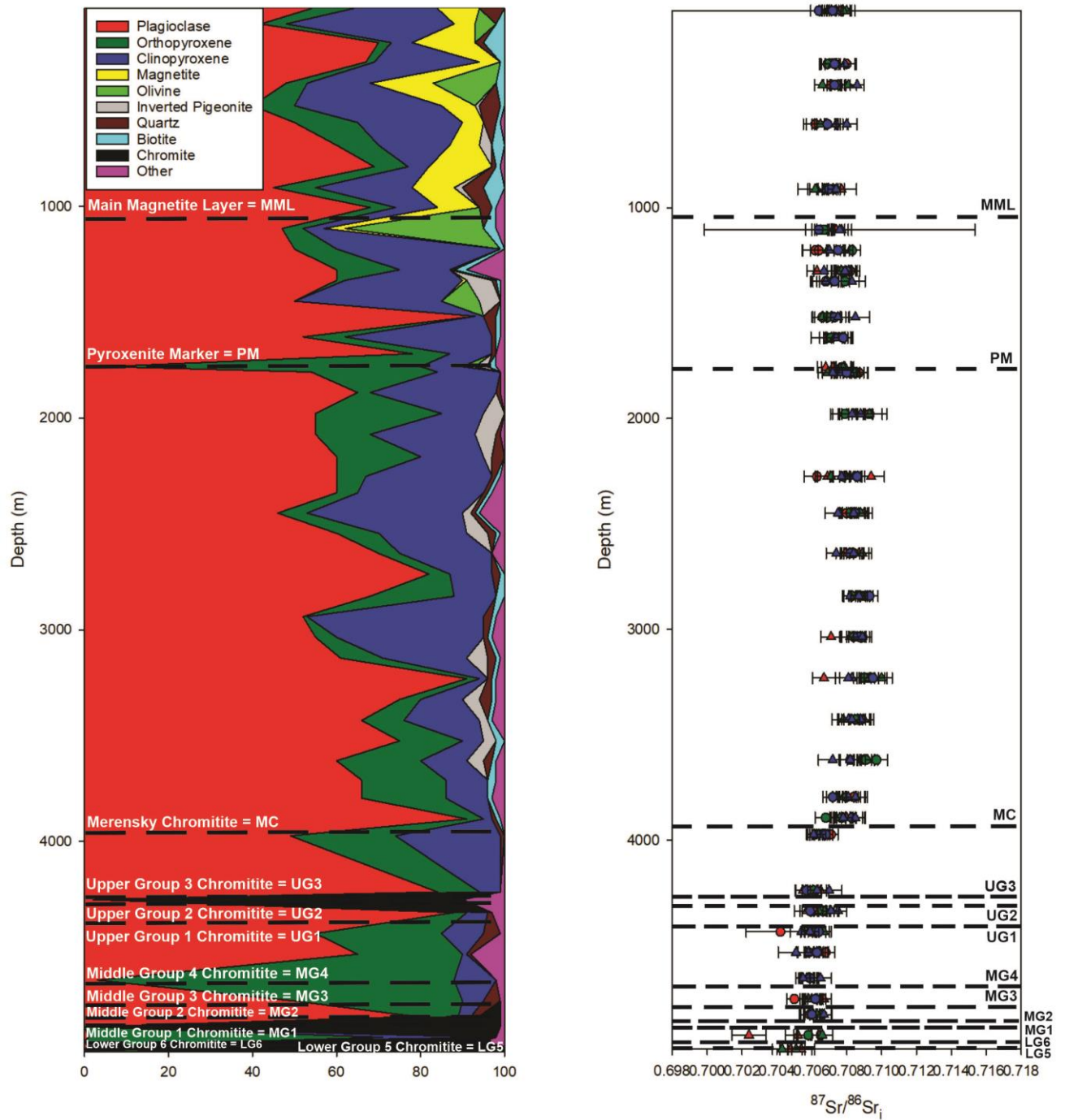


Figure 30: The initial $^{87}\text{Sr}/^{86}\text{Sr}$ composition of analysed spots plotted against depth, with modal mineralogy graph showing varying mineral compositions of samples throughout the stratigraphy. Different colours show coexisting plagioclase in a single sample. Circles represent analysed core domains while triangles represent rims. Error bars represent 2SE.

The plagioclase in the sampled LCZ shows variation in initial $^{87}\text{Sr}/^{86}\text{Sr}$ ratios, with an average value of 0.7052, ranging between 0.7024 and 0.7066. The plagioclase from the sampled UCZ rocks also shows variation in initial $^{87}\text{Sr}/^{86}\text{Sr}$ values, with an average value of 0.7063, ranging from 0.7042 to 0.7085. The sampled LMZ plagioclase shows varying initial $^{87}\text{Sr}/^{86}\text{Sr}$ values with an average of 0.7084, ranging between 0.7100 and 0.7063. The plagioclase from the sampled UMZ shows fairly little variation in initial $^{87}\text{Sr}/^{86}\text{Sr}$ ratios, with an average value of 0.7073, ranging between 0.7063 and 0.7083. The sampled UZ plagioclase shows initial $^{87}\text{Sr}/^{86}\text{Sr}$ compositions that have very limited variation across the stratigraphy with an average value of 0.7072. The ratios range between 0.7062 and 0.7086 in the UZ.

Initial $^{87}\text{Sr}/^{86}\text{Sr}$ variations between coexisting plagioclase (inter-granular variation) and within individual plagioclase crystals (intra-granular variation) were observed in some samples (Table 2). Two samples from the UZ show both inter- and intra-granular isotopic disequilibrium, at depths of 418.31 m and 911.78 m. Homogeneous plagioclase coexist with heterogeneous plagioclase, whereby the cores are in disequilibrium with the rims. The rims of different plagioclase crystals in these samples also vary, whereby the rims of homogeneous plagioclase are less radiogenic compared to the rims of heterogeneous plagioclase at 418.31 m. The inverse is applicable in the plagioclase crystals of the magnetite gabbronorite at 911.78 m. The sampled UMZ only has one sample that showed inter- and intra-granular variation. The gabbronorite at 1299.49 m has a homogeneous plagioclase that coexists with heterogeneous plagioclase, with cores that are more radiogenic than rims.

Plagioclase in the rocks from the sampled LMZ show larger variation, with inter- and intra-granular initial $^{87}\text{Sr}/^{86}\text{Sr}$ variation observed in five samples from depths of 1782.05 m, 2274.98 m, 2448.40 m, 3230.89m and 3795.28 m. The heterogeneous plagioclase in the gabbronorite at 1782.05 m and the spotted anorthosite at 3230.89 m show the same initial $^{87}\text{Sr}/^{86}\text{Sr}$ ratio for the core and one rim, with a decrease in the other rim. The homogeneous plagioclase in the gabbronorites at 2274.98 m, 2448.40 m and 3795.28 m coexist with heterogeneous plagioclase that has rims that are more radiogenic than the cores.

Inter- and intra-granular initial $^{87}\text{Sr}/^{86}\text{Sr}$ variation is also observed in five samples of the UCZ at depths of 3893.44 m, 4238.37 m, 4335.85 m, 4434.09 m, and 4753.11 m. Homogeneous plagioclase in the spotted anorthosite and gabbronorite at 3893.44 m and 4238.37 m respectively, coexist with heterogeneous plagioclase with the same initial $^{87}\text{Sr}/^{86}\text{Sr}$ ratio for one rim and the core, with an increase in another rim. Homogeneous plagioclase in the anorthosite and gabbronorite at 4335.85 m and 4753.11 m respectively, coexist with heterogeneous plagioclase that has rims that are more radiogenic than the cores. The heterogeneous plagioclase in the gabbronorite at 4434.09 m has rims that are in disequilibrium.

Only two samples from the sampled LCZ were analysed and there was no inter- or intra-granular variation observed in both samples.

Table 2: Samples showing inter- and intra-crystal initial $^{87}\text{Sr}/^{86}\text{Sr}$ variation.

Depth	Sample	Plag#	Point	Zone	$^{87}\text{Sr}/^{86}\text{Sr}$	$^{87}\text{Rb}/^{86}\text{Sr}$	$^{87}\text{Sr}/^{86}\text{Sr}_i$	2SE	Rim/Core
418,31	TM 1.6	26	99	UZ	0,7072	0,0043	0,7071	0,0004	Rim
		26	97	UZ	0,7075	0,0020	0,7075	0,0004	Rim
		26	100	UZ	0,7072	0,0026	0,7071	0,0004	Core
		28	106	UZ	0,7076	0,0057	0,7075	0,0005	Core
		28	109	UZ	0,7067	0,0028	0,7066	0,0004	Rim
		28	110	UZ	0,7083	0,0052	0,7081	0,0005	Rim
		30	118	UZ	0,7086	0,0023	0,7086	0,0004	Rim
		30	120	UZ	0,7074	0,0032	0,7073	0,0004	Core
		30	117	UZ	0,7074	0,0028	0,7073	0,0004	Core
911,78	TM 1.11	56	188	UZ	0,7077	0,0003	0,7077	0,0009	Rim
		56	189	UZ	0,7071	0,0317	0,7062	0,0010	Rim
		56	190	UZ	0,7070	0,0004	0,7069	0,0006	Core
		58	193	UZ	0,7072	0,0338	0,7063	0,0004	Rim
		58	191	UZ	0,7077	0,0507	0,7062	0,0004	Rim
		58	192	UZ	0,7074	0,0029	0,7073	0,0003	Core
		59	196	UZ	0,7068	0,0009	0,7068	0,0004	Rim
		59	195	UZ	0,7071	0,0015	0,7070	0,0004	Core
		59	197	UZ	0,7075	0,0008	0,7074	0,0005	Rim
1299,49	TM 1.13.2	79	229	UMZ	0,7075	0,0010	0,7075	0,0006	Rim
		79	230	UMZ	0,7064	0,0037	0,7063	0,0006	Rim
		79	231	UMZ	0,7082	0,0017	0,7082	0,0005	Core
		82	232	UMZ	0,7078	0,0022	0,7077	0,0005	Rim
		82	233	UMZ	0,7077	0,0011	0,7077	0,0006	Core
		82	234	UMZ	0,7077	0,0010	0,7077	0,0006	Rim
		84	236	UMZ	0,7082	0,0075	0,7080	0,0006	Core
		84	237	UMZ	0,7067	0,0006	0,7067	0,0006	Rim
		84	235	UMZ	0,7080	0,0023	0,7079	0,0006	Rim
1782,05	TM 1.17	103	287	LMZ	0,7080	0,0027	0,7079	0,0006	Rim
		103	286	LMZ	0,7085	0,0185	0,7079	0,0005	Rim
		103	286	LMZ	0,7080	0,0119	0,7077	0,0006	Rim
		103	285	LMZ	0,7091	0,0141	0,7087	0,0005	Core
		105	290	LMZ	0,7087	0,0042	0,7086	0,0006	Rim
		105	289	LMZ	0,7085	0,0026	0,7084	0,0006	Core
		105	288	LMZ	0,7070	0,0033	0,7069	0,0005	Rim
		107	291	LMZ	0,7083	0,0033	0,7082	0,0005	Rim
		107	292	LMZ	0,7078	0,0030	0,7077	0,0005	Rim
2274,98	TM 1.22	133	446	LMZ	0,7065	0,0060	0,7063	0,0007	Core
		133	447	LMZ	0,7069	0,0028	0,7069	0,0007	Rim
		133	448	LMZ	0,7095	0,0058	0,7094	0,0008	Rim
		136	320	LMZ	0,7082	0,0055	0,7080	0,0008	Rim
		136	319	LMZ	0,7080	0,0065	0,7078	0,0007	Core
		136	318	LMZ	0,7073	0,0046	0,7071	0,0008	Rim

Table 2: (continued).

Depth	Sample	Plag#	Point	Zone	$^{87}\text{Sr}/^{86}\text{Sr}$	$^{87}\text{Rb}/^{86}\text{Sr}$	$^{87}\text{Sr}/^{86}\text{Sr}_i$	2SE	Rim/Core
2274,98		138	322	LMZ	0,7087	0,0054	0,7086	0,0004	Core
2274,98		138	321	LMZ	0,7078	0,0037	0,7077	0,0005	Rim
2448,40	TM 1.24	150	449	LMZ	0,7082	0,0023	0,7081	0,0005	Rim
2448,40		150	450	LMZ	0,7081	0,0033	0,7080	0,0004	Core
2448,40		150	451	LMZ	0,7091	0,0032	0,7090	0,0004	Rim
2448,40		149	330	LMZ	0,7088	0,0033	0,7087	0,0005	Rim
2448,40		149	329	LMZ	0,7089	0,0033	0,7088	0,0005	Rim
2448,40		149	327	LMZ	0,7083	0,0041	0,7082	0,0005	Core
2448,40		145	326	LMZ	0,7076	0,0055	0,7075	0,0007	Rim
2448,40		145	324	LMZ	0,7086	0,0039	0,7085	0,0005	Core
2448,40		145	325	LMZ	0,7085	0,0038	0,7084	0,0006	Rim
3230,89	TM 1.32	195	461	LMZ	0,7096	0,0018	0,7096	0,0006	Rim
3230,89		195	462	LMZ	0,7093	0,0022	0,7092	0,0006	Core
3230,89		195	463	LMZ	0,7150	0,2887	0,7067	0,0007	Rim
3230,89		196	350	LMZ	0,7100	0,0019	0,7100	0,0006	Rim
3230,89		196	351	LMZ	0,7090	0,0019	0,7090	0,0006	Core
3230,89		196	349	LMZ	0,7096	0,0090	0,7093	0,0005	Rim
3230,89		197	354	LMZ	0,7099	0,0156	0,7095	0,0008	Core
3230,89		197	353	LMZ	0,7085	0,0056	0,7083	0,0007	Rim
3230,89		197	352	LMZ	0,7082	0,0036	0,7081	0,0007	Rim
3795,28	TM 1.38	229	367	LMZ	0,7082	0,0065	0,7080	0,0008	Rim
3795,28		229	368	LMZ	0,7079	0,0031	0,7078	0,0006	Rim
3795,28		229	369	LMZ	0,7091	0,0255	0,7084	0,0008	Core
3795,28		232	370	LMZ	0,7086	0,0026	0,7085	0,0006	Rim
3795,28		232	371	LMZ	0,7081	0,0027	0,7080	0,0005	Core
3795,28		232	372	LMZ	0,7075	0,0031	0,7074	0,0006	Rim
3795,28		234	470	LMZ	0,7082	0,0021	0,7081	0,0006	Rim
3795,28		234	471	LMZ	0,7072	0,0018	0,7072	0,0005	Core
3795,28		234	472	LMZ	0,7086	0,0023	0,7085	0,0005	Rim
3893,44	TM 1.39	236	436	UCZ	0,7080	0,0023	0,7079	0,0006	Rim
3893,44		236	437	UCZ	0,7078	0,0015	0,7077	0,0006	Core
3893,44		236	438	UCZ	0,7080	0,0020	0,7080	0,0006	Rim
3893,44		238	441	UCZ	0,7076	0,0018	0,7076	0,0006	Rim
3893,44		238	439	UCZ	0,7069	0,0025	0,7068	0,0006	Core
3893,44		238	440	UCZ	0,7085	0,0015	0,7085	0,0005	Rim
3893,44		240	473	UCZ	0,7083	0,0017	0,7083	0,0006	Core
3893,44		240	474	UCZ	0,7086	0,0050	0,7085	0,0006	Rim
3893,44		240	475	UCZ	0,7078	0,0015	0,7078	0,0006	Rim
4238,37	TM 1.40	243	424	UCZ	0,7068	0,0111	0,7065	0,0005	Rim
4238,37		243	425	UCZ	0,7061	0,0079	0,7059	0,0005	Rim
4238,37		243	426	UCZ	0,7058	0,0099	0,7055	0,0004	Rim
4238,37		244	422	UCZ	0,7063	0,0068	0,7061	0,0005	Rim
4238,37		244	421	UCZ	0,7063	0,0082	0,7061	0,0004	Rim
4238,37		244	423	UCZ	0,7063	0,0079	0,7061	0,0004	Core

Table 2: (continued).

Depth	Sample	Plag#	Point	Zone	$^{87}\text{Sr}/^{86}\text{Sr}$	$^{87}\text{Rb}/^{86}\text{Sr}$	$^{87}\text{Sr}/^{86}\text{Sr}_i$	2SE	Rim/Core
4238,37		246	479	UCZ	0,7072	0,0077	0,7070	0,0007	Rim
4238,37		246	481	UCZ	0,7066	0,0081	0,7063	0,0005	Rim
4335,85	TM 1.41	248	381	UCZ	0,7070	0,0089	0,7067	0,0008	Core
4335,85		248	380	UCZ	0,7065	0,0133	0,7061	0,0008	Core
4335,85		248	379	UCZ	0,7058	0,0055	0,7057	0,0007	Rim
4335,85		251	383	UCZ	0,7070	0,0050	0,7068	0,0005	Rim
4335,85		251	384	UCZ	0,7068	0,0074	0,7066	0,0005	Core
4335,85		251	382	UCZ	0,7066	0,0060	0,7064	0,0004	Rim
4335,85		252	482	UCZ	0,7076	0,0050	0,7075	0,0005	Rim
4335,85		252	483	UCZ	0,7061	0,0049	0,7059	0,0005	Core
4335,85		252	484	UCZ	0,7073	0,0061	0,7071	0,0005	Rim
4434,09	TM 1.42	254	485	UCZ	0,7065	0,0092	0,7062	0,0006	Rim
4434,09		254	486	UCZ	0,7046	0,0109	0,7042	0,0020	Core
4434,09		256	425	UCZ	0,7061	0,0099	0,7058	0,0004	Rim
4434,09		256	426	UCZ	0,7070	0,0110	0,7067	0,0004	Rim
4434,09		256	424	UCZ	0,7063	0,0106	0,7060	0,0004	Core
4434,09		258	428	UCZ	0,7067	0,0102	0,7064	0,0006	Core
4434,09		258	427	UCZ	0,7057	0,0102	0,7054	0,0006	Rim
4434,09		258	429	UCZ	0,7062	0,0100	0,7059	0,0005	Rim
4753,11	TM 1.45	271	493	UCZ	0,7051	0,0032	0,7050	0,0005	Core
4753,11		271	494	UCZ	0,7068	0,0041	0,7067	0,0004	Rim
4753,11		271	495	UCZ	0,7062	0,0049	0,7060	0,0003	Rim
4753,11		272	392	UCZ	0,7059	0,0036	0,7058	0,0005	Rim
4753,11		272	391	UCZ	0,7062	0,0043	0,7060	0,0006	Rim
4753,11		272	393	UCZ	0,7062	0,0045	0,7060	0,0005	Rim
4753,11		275	394	UCZ	0,7063	0,0037	0,7062	0,0006	Rim
4753,11		275	395	UCZ	0,7063	0,0129	0,7060	0,0005	Rim
4753,11		275	396	UCZ	0,7061	0,0045	0,7060	0,0005	Rim
4753,11		275	496	UCZ	0,7063	0,0049	0,7062	0,0004	Core

The variation in the average initial $^{87}\text{Sr}/^{86}\text{Sr}$ ratios of plagioclase with depth is depicted in Figure 31. The error bars represent 2 standard deviation, where by the standard deviations (initial $^{87}\text{Sr}/^{86}\text{Sr}$) for each sample were calculated and the average was multiplied by 2. At the base of the studied succession, from the depth of 4991.09 m in the LCZ to the bottom of the UCZ at 4826.62 m, there is an increase in initial $^{87}\text{Sr}/^{86}\text{Sr}$ ratios. This increase is from a value of 0.7048 to 0.7062, and the stratigraphic level represents the transition from intercumulus to cumulus plagioclase from the LCZ to the UCZ, respectively. The increase is followed by a decrease in initial $^{87}\text{Sr}/^{86}\text{Sr}$ ratio to 0.7058 at the depth of 4654.76 m.

A slight increase in the initial $^{87}\text{Sr}/^{86}\text{Sr}$ ratio to a value of 0.7061 is recorded at 4532.20 m, which is followed by a decrease to a value of 0.7058 at 4434.09 m. From 4434.09 m to 4335.85 m, the initial $^{87}\text{Sr}/^{86}\text{Sr}$ ratio increase from a value of 0.7058 to 0.7065. The increase is subsequently followed by a decrease to a value of 0.7061 m at the depth of 4238.37 m.

From 4238.37 m to 3618.98 m, the initial $^{87}\text{Sr}/^{86}\text{Sr}$ ratio increases from 0.7061 to 0.7087, transitioning from the UCZ to the LMZ. This major increase in initial $^{87}\text{Sr}/^{86}\text{Sr}$ ratio is followed by a slight decrease to a value of 0.7085 at 3427.93 m. At 3230.89 m, the initial $^{87}\text{Sr}/^{86}\text{Sr}$ ratio increased to a value of 0.7088, followed by a decrease to a value of 0.7084 at 3035.77 m. The initial $^{87}\text{Sr}/^{86}\text{Sr}$ ratio increased to a value of 0.7087 at the depth of 2841.74 m. From 2841.74 m to 2274.98, the initial $^{87}\text{Sr}/^{86}\text{Sr}$ ratio decreases from 0.7087 to 0.7078.

An increase in initial $^{87}\text{Sr}/^{86}\text{Sr}$ ratio to a value of 0.7086 is recorded at 1978.02 m. From 1978.02 m to 1782.05 m, which is just below the Pyroxenite Marker, the initial $^{87}\text{Sr}/^{86}\text{Sr}$ ratio decreased from 0.7086 to 0.7079. The decreasing trend is continued into the Pyroxenite Marker whereby the initial $^{87}\text{Sr}/^{86}\text{Sr}$ ratio recorded a value of 0.7075. The initial $^{87}\text{Sr}/^{86}\text{Sr}$ ratios in the UMZ remain relatively constant from the Pyroxenite Marker at 1757.02 m to 1201.54 m, with an average value of 0.7074. The initial $^{87}\text{Sr}/^{86}\text{Sr}$ ratios in the UZ also remained relatively constant from 1104.46 m to 65.66 m, with an average value of 0.7072.

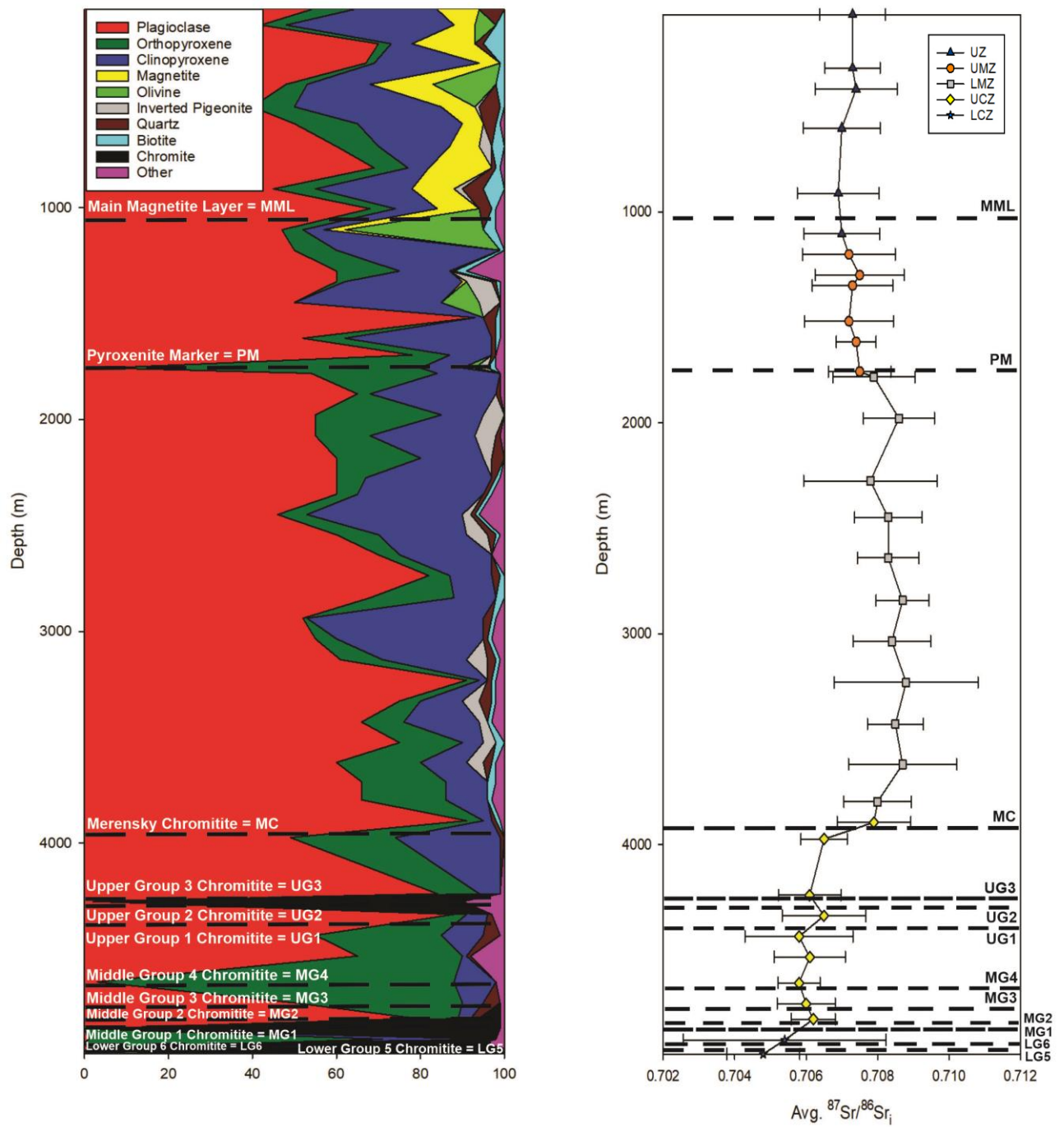


Figure 31: The variation in the average initial $^{87}\text{Sr}/^{86}\text{Sr}$ compositions of plagioclase with depth, compared to the variation in modal mineralogical composition. Error bars indicate 2 standard deviations.

4. DISCUSSION

4.1 Variations in whole-rock geochemistry and plagioclase mineral chemistry.

Whole-rock major and trace element data were presented above on binary variation diagrams and vertical stratigraphic profiles to observe variations through the LCZ to the UZ of the Eastern Limb of the BC (Figures 22 - 26).

Changes in whole-rock Mg# as discussed above are attributed to crystal fractionation and/or injection of new magma pulses. Mg# plotted against depth remains rather constant throughout the lower Main and Upper Critical zones, showing a general lack of differentiation. This is attributed to the repeated influx of magmas into the RLS over this stratigraphic interval. Roelofse & Ashwal (2012) similarly found a lack of differentiation within the LMZ of the Northern Limb of the BC, which they also attributed to repeated influxes of magma. The decreasing (i.e. normal differentiation) trend of Mg# across the Upper Main and Upper zones suggests fractional crystallisation to have been the main petrogenetic process within these zones, following the injection of the last major influx of magma into the RLS at or about the level of the Pyroxenite Marker (Figure 24). Most trace elements show constant concentrations in the Critical and Lower Main zones when plotted against depth (Figure 26). There are decreasing/increasing trends observed in the concentrations of some trace elements in the UZ with an increase in stratigraphic height, which might be a sign of fractionation in this zone.

There is a sharp increase in the calculated An% of plagioclase in the Eastern Limb, from the sampled LCZ to the UCZ, which might be an indication of an injection of a magma that is compositionally different (Figure 29). However, this could also merely be a reflection of the fact that plagioclase changes from being an intercumulus phase in the sampled LCZ to being a cumulus phase in the sampled UCZ. The calculated An% in the sampled UCZ shows cycles of normal fractionation and magma influxes, with limited variation overall and an overall lack of differentiation is observed in the Upper Critical and Lower Main Zones. These features also point to repeated influxes of magma into the RLS across these zones. The decreasing trend in the calculated plagioclase An% observed in the sampled UZ suggests that fractional crystallisation was the main petrogenetic process operating within the upper reaches of the RLS.

4.2 Variations in the Sr-isotopic composition of plagioclase

Karykowski *et al.* (2017) studied the entire stratigraphic profile of the BC analysing samples from the Western and Northern Limbs (Figure 32A). The interstitial plagioclase contained in the pyroxenite from the sampled LCZ recorded average initial $^{87}\text{Sr}/^{86}\text{Sr}$ ratios from 0.7049 to 0.7055. Similar initial $^{87}\text{Sr}/^{86}\text{Sr}$ ratios of plagioclase are recorded in the pyroxenites of this study, ranging from 0.7048 to 0.7054 near the LCZ/UCZ boundary at a depth of 4924.39 m. The values fall within error of each other and the plagioclase crystals are not radiogenic. Karykowski *et al.* (2017) defined the LCZ/UCZ boundary by the first occurrence of cumulus plagioclase, at the base of the MG3 chromite layer. Their observation is supported in this study by a sharp increase in initial $^{87}\text{Sr}/^{86}\text{Sr}$ ratios and An% content going from the LCZ to the UCZ (Figure 32A).

Sharpe (1985) was one of the earliest authors to investigate the initial $^{87}\text{Sr}/^{86}\text{Sr}$ ratios of the stratigraphy in the Eastern Limb of the BC. The author recorded initial $^{87}\text{Sr}/^{86}\text{Sr}$ ratios from 0.7061 to 0.7065 in the UCZ, while this study recorded ratios between 0.7058 and 0.7079 in the sampled UCZ. The ratios in this zone fall within error of each other and are more radiogenic compared to the LCZ ratios. Lee and Butcher (1990) recorded initial $^{87}\text{Sr}/^{86}\text{Sr}$ ratios of 0.7064 ± 1 and 0.7064 ± 2 in the Merensky Reef and in the norite above the Merensky Reef in the UCZ, while this study recorded an average initial $^{87}\text{Sr}/^{86}\text{Sr}$ ratio of 0.7063. The pyroxenite above the chromitite stringer of the Merensky Reef in the UCZ recorded initial $^{87}\text{Sr}/^{86}\text{Sr}$ ratios of 0.7090 ± 2 . According to the authors, the differences in initial $^{87}\text{Sr}/^{86}\text{Sr}$ suggest mixing of magmas of contrasting isotopic compositions.

Seabrook *et al.* (2005) and Yang *et al.* (2013) recorded Sr-isotopic disequilibrium in mineral separates of the UCZ in the Eastern Limb and Western Limb, respectively. The former study found Sr-isotopic disequilibrium between coexisting plagioclase and orthopyroxene, while the latter study found Sr-isotopic disequilibrium between cores and rims of plagioclase crystals and between cores of various plagioclase crystals. Similar Sr-isotopic disequilibrium is observed in the gabbronorite at 4434.09 m of this study, as shown in Table 2 above, whereby the core of one plagioclase crystal recorded an average $^{87}\text{Sr}/^{86}\text{Sr}$ ratio that is different from the cores of coexisting plagioclase crystals and rims within the same plagioclase crystal. Seabrook *et al.* (2005) concluded that the Sr-isotopic disequilibrium observed in their

study is not in favour of a magma mixing model to account for Sr-isotope variations throughout the Merensky and Bastard cyclic units, but that the observed Sr-isotopic disequilibrium is suggestive of co-accumulation of minerals from different stratified magmas.

Sharpe (1985) observed an increase from 0.7065 in the UCZ to 0.7085 about 200 m into the LMZ. This break was also recorded at the level of the Merensky Reef by Seabrook *et al.* (2005). These observations are consistent with the current study, which shows a sharp increase in initial $^{87}\text{Sr}/^{86}\text{Sr}$ ratio and the calculated plagioclase An% from below the Merensky Reef to the lower sections of the LMZ (Figure 32B). Both features point to the introduction of a more primitive, isotopically distinct magma into the RLS at the level of the UCZ/LMZ boundary.

Roelofse & Ashwal (2012) recorded significant disequilibrium in initial $^{87}\text{Sr}/^{86}\text{Sr}$ ratios of coexisting plagioclase (0.708) and orthopyroxene (~0.711) in the LMZ of the Northern Limb. Mangwegape *et al.* (2016) recorded variations in initial $^{87}\text{Sr}/^{86}\text{Sr}$ ratios within and between individual coexisting plagioclase crystals in the LMZ of the Northern Limb, which they argued are suggestive of the intrusion of crystal mushes as opposed to aphyric liquids. Similar disequilibrium features to those observed by Mangwegape *et al.* (2016) were observed in three samples of the LMZ in this study, as shown in Table 2 above.

Mangwegape *et al.* (2016) reported an average Sr-isotopic ratios for the LMZ in the Northern Limb of $\sim 0.7087 \pm 0.0005$. They also recorded an overall lack of differentiation, as shown by the calculated plagioclase An%, which they used to suggest that their sampled LMZ was formed through the repeated influx of magmas. The LMZ in the current study has Sr-isotopic compositions that overlap with those of Mangwegape *et al.* (2016), of $\sim 0.7084 \pm 0.0003$, whereby the ratios fall within error of each other and the ratios are more radiogenic compared to the CZ. The LMZ in the present study similarly shows limited variation in the calculated An% of plagioclase, suggestive of limited differentiation.

Tegner *et al.* (2006) reported that the initial $^{87}\text{Sr}/^{86}\text{Sr}$ ratios are near constant (0.7073 ± 0.0001) in the Upper Main and Upper Zones, suggesting that rock cumulates formed from crystallization of a homogeneous magma sheet without major magma recharge. Mangwegape *et al.* (2016) also recorded a near constant $^{87}\text{Sr}/^{86}\text{Sr}$

composition ($\sim 0.7073 \pm 0.0003$) of plagioclase within the Upper Main and Upper Zones in the Northern Limb. A similar near-constant trend of initial $^{87}\text{Sr}/^{86}\text{Sr}$ composition (0.7074 ± 0.0003) of plagioclase was observed in the UMZ in this study, whereby the ratios fall within error of each other. The UZ also has a similar trend of initial $^{87}\text{Sr}/^{86}\text{Sr}$ ratios (0.7072 ± 0.0003) of plagioclase, whereby the ratios fall within error of each other. Kruger *et al.* (1987) observed a gradual increase in calculated An% in plagioclase and change in initial $^{87}\text{Sr}/^{86}\text{Sr}$ composition from 0.7082 below the Pyroxenite Marker to 0.7073 above the Pyroxenite Marker, attributed to magma recharge and mixing at the level of the Pyroxenite Marker. Similar changes are observed in this study as shown in Figure 32B.

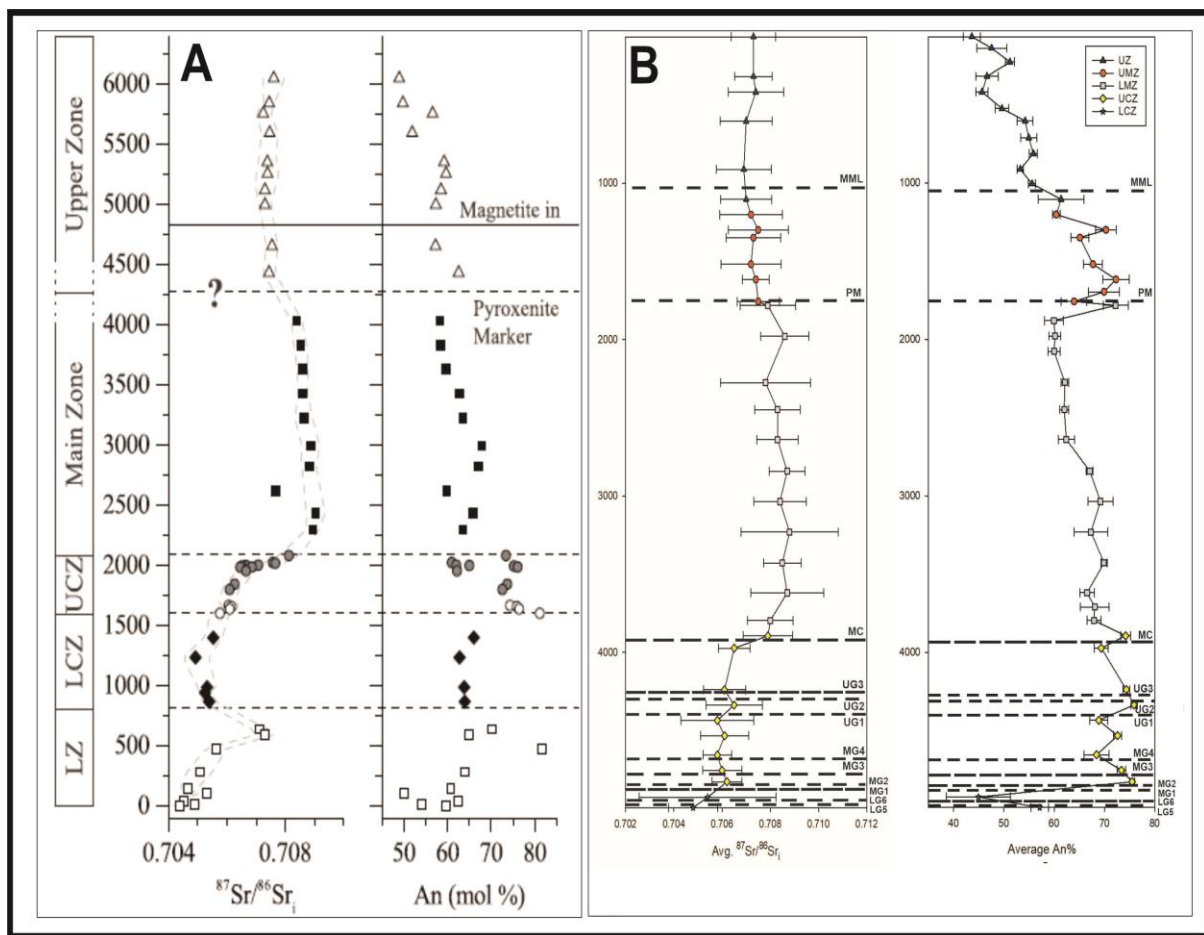


Figure 32: Comparison of variations in initial $^{87}\text{Sr}/^{86}\text{Sr}$ compositions and anorthite (An%) content of plagioclase across the stratigraphy: (A) Karykowski *et al.* (2017) and (B) this study.

4.3 Comparison of the Sr-isotopic stratigraphy of the Eastern Limb with the Western Limb

Kruger (1994) proposed two stages, based on variations in initial $^{87}\text{Sr}/^{86}\text{Sr}$ ratios, in the development of the RLS in the Western Limb of the BC (Figure 3 and 33). The two stages are the Integration and Differentiation stage, whereby the former comprises of the Lower, Critical and Lower Main Zones, while the latter comprises of the Upper Main and Upper Zones. The Integration Stage is distinguished from the Differentiation Stage by an irregular upward increase in the initial $^{87}\text{Sr}/^{86}\text{Sr}$ ratios from 0.7047 in the LZ to 0.7091 in the LMZ, with a decrease in the initial $^{87}\text{Sr}/^{86}\text{Sr}$ ratio from 0.7071 to 0.7047 at the LZ/LCZ boundary. The Differentiation Stage on the other hand is marked by constant initial $^{87}\text{Sr}/^{86}\text{Sr}$ compositions with the exception of a step-like change at the Pyroxenite Marker (Kruger *et al.*, 1987), where $^{87}\text{Sr}/^{86}\text{Sr}$ changes from 0.7085 to 0.7073 (Kruger, 1994). The entire sampled UZ is characterized by uniform initial $^{87}\text{Sr}/^{86}\text{Sr}$ ratios, and this uniformity was also observed by Sharpe (1985) in the Eastern Limb of the BC.

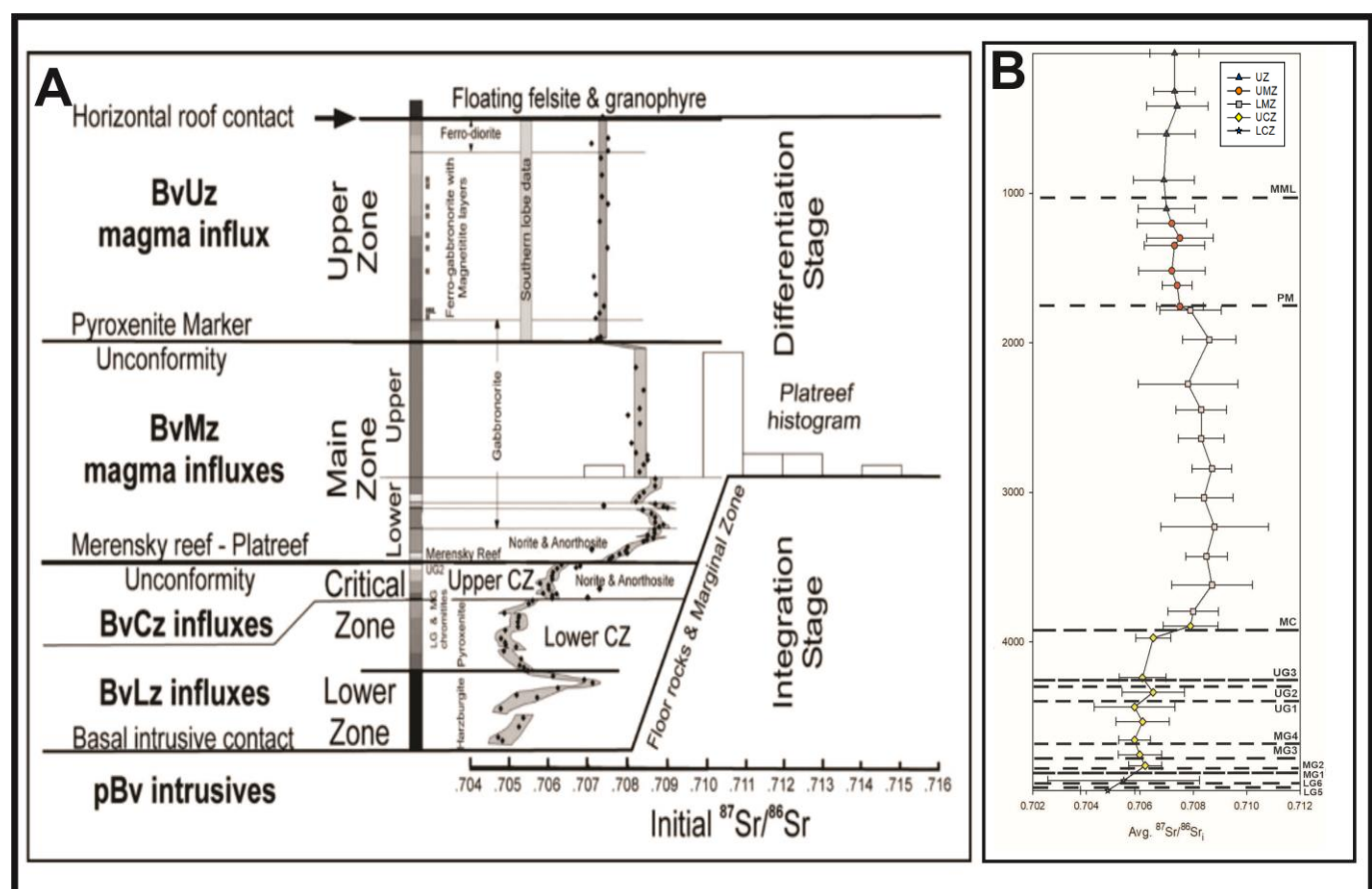


Figure 33: Comparison of initial $^{87}\text{Sr}/^{86}\text{Sr}$ compositions of the Western Limb and the Eastern Limb from: (A) Kruger (2005) and (B) this study, respectively.

Kruger (1994) interpreted the heterogeneity in initial $^{87}\text{Sr}/^{86}\text{Sr}$ compositions of the Integration Stage to be the result of repeated influxes of compositionally different magmas, with limited mixing between the new and existing magmas in the chamber. The Differentiation Stage, which exhibits homogeneous initial $^{87}\text{Sr}/^{86}\text{Sr}$ compositions, is interpreted to have formed due to closed system fractional crystallisation. The last major magma influx is believed to have happened at the level of the Pyroxenite Marker, at the beginning of the Differentiation Stage.

The Sr-isotopic data that are presented in this study for the Eastern Limb of the BC, exhibits similar variations to the ones observed in the Western Limb of the BC by Kruger (1994). Based on these similarities, the Eastern Limb can also be divided into an Integration and Differentiation Stages. The Integration Stage of the Eastern Limb in this study exhibit fluctuating initial $^{87}\text{Sr}/^{86}\text{Sr}$ compositions, coinciding with very limited differentiation as exemplified by the calculated plagioclase An%. This stage is interpreted to have formed due to repeated influxes of new magma in the Critical and Lower Main Zones.

The existence of inter- and intra-crystal Sr-isotopic disequilibrium in the Upper Critical and Lower Main Zones, suggests that the influxes may have consisted of crystal-charged mushes, rather than aphyric liquids. Such a model was also proposed by Roelofse & Ashwal (2012), Roelofse *et al.* (2015) and Mangwegape *et al.* (2016) for the Northern Limb of the BC.

4.4 A petrogenetic model for the Eastern Limb of the Bushveld Complex

Key aspects that need to be taken into consideration when proposing a petrogenetic model for the Critical, Main and Upper Zones of the BC in this study include: (1) the inter- and intra-crystal disequilibrium of initial $^{87}\text{Sr}/^{86}\text{Sr}$ ratios, largely observed in the Upper Critical and Lower Main Zones as opposed to the Upper Main and Upper Zones and (2) very limited differentiation observed in the Critical and Lower Main Zones, with more pronounced differentiation observed in the Upper and Upper Main Zones. These key features were also observed in similar studies by Roelofse & Ashwal (2012), Yang *et al.* (2013), Roelofse *et al.* (2015) and Mangwegape *et al.* (2015).

The lower reaches of the RLS were constructed through the repeated influx of magma as recorded by variations in the Sr_i and very limited differentiation observed in the Critical and Lower Main Zones. These influxes were most likely not aphyric because of the inter- and intra-crystal disequilibrium that was observed largely in the Upper Critical and Lower Main Zones. A model similar to the one proposed by Roelofse & Ashwal (2012) to account for the Sr-isotopic disequilibrium between coexisting plagioclase and orthopyroxene in the LMZ of the Northern Limb of the BC is proposed for this study. The Critical and Lower Main Zones of the Eastern Limb of the BC formed through intrusion of variably contaminated crystal mushes derived from a sub-compartmentalized, sub-Bushveld staging chamber that underwent different degrees of contamination with crustal rocks of the Kaapvaal craton.

The Upper Main and Upper Zones experienced differentiation as the main petrogenetic process without major additional input of magma, apart from at the level of the Pyroxenite Marker. This is supported by the normal fractionation observed through the decrease in the calculated Mg#, An% and the homogeneity observed in the Sr_i compositions in the Upper Main and Upper Zones, following the significant decrease observed at the level of the Pyroxenite Marker.

5. Summary

The studied samples are broadly gabbronoritic to gabbroic in the Upper and Main Zones, with pyroxenitic cumulates dominating the CZ. Plagioclase was the dominant mineral encountered in the study. Plagioclase occurs as a cumulus mineral within the Upper Critical, Main and Upper Zones, and as an intercumulus mineral in the LCZ.

Magnetite is confined to samples from the UZ. Biotite occurs as a minor mineral throughout the entire stratigraphy, and it has been altered to chlorite near the UZ/UMZ boundary. Inverted pigeonite was encountered in the lower parts of the UZ, the UMZ and the LMZ. Olivine was encountered in the interstitial spaces of the rock cumulates in the UZ, occurring in one sample of the UMZ and at the Pyroxenite Marker. Chromite is confined to the CZ, forming chromitites locally, but also occurring as disseminated crystals in the silicate rocks close to the chromitite layers. Quartz was encountered as a minor mineral throughout the entire studied stratigraphy (Figure 34A).

The calculated Mg# plotted against depth (Figure 34B) remains virtually unchanged throughout the Lower Main and Upper Critical zones, showing a general lack of differentiation. This can be attributed to the repeated influx of magmas into the RLS over this stratigraphic interval. A decreasing trend of the calculated Mg# observed across the Upper Main and Upper Zones suggests fractional crystallisation to have been the main petrogenetic process within these zones, following injection of the last major influx of magma into the RLS at or about the level of the Pyroxenite Marker.

The calculated An% plotted against depth (Figure 34C) show limited differentiation in the Critical and Lower Main zones with cycles of normal differentiation and magma replenishment observed in the UCZ. These observations suggest repeated influxes of magma into the RLS across these zones. The decreasing trend in the calculated plagioclase An% across the Upper Main and Upper Zones suggests fractional crystallisation as the main petrogenetic process that was operating in the upper reaches of the RLS.

The initial $^{87}\text{Sr}/^{86}\text{Sr}$ composition of plagioclase plotted against depth (Figure 34D) show significant variability in the Critical and Lower Main Zones, which suggest repeated influxes of magma during the petrogenesis of these zones. The uniform

trend of initial $^{87}\text{Sr}/^{86}\text{Sr}$ compositions of plagioclase in the Upper Main and Upper Zones suggests fractional crystallisation as the petrogenetic process that was operating across these zones, with the last major injection of magma recorded at the level of the Pyroxenite Marker, marked by a significant decrease in initial $^{87}\text{Sr}/^{86}\text{Sr}$ ratios at this level.

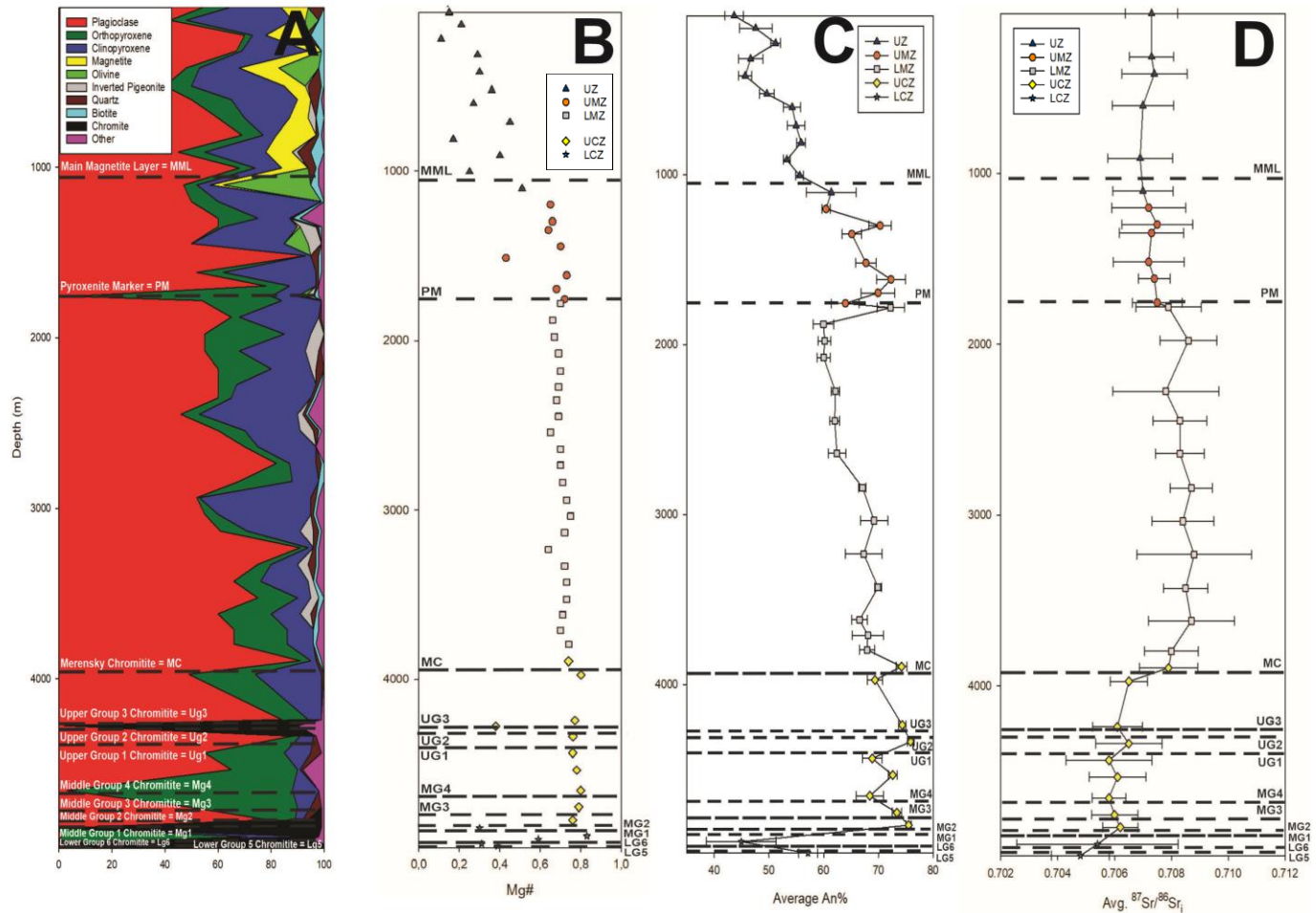


Figure 34: Variations in: A) Modal mineralogy; B) Whole-rock Mg#; C) Plagioclase An% and D) Plagioclase Sr_i.

6. Conclusion

The whole-rock geochemical data, plagioclase compositional data (An%) and plagioclase $^{87}\text{Sr}/^{86}\text{Sr}$ compositions in this study provided a broad view of understanding the petrogenesis of the Critical, Main and Upper Zones of the Eastern Limb of the Bushveld Complex. Significant variations in initial $^{87}\text{Sr}/^{86}\text{Sr}$ ratios, coupled with a lack of differentiation as shown by the calculated plagioclase An% and the calculated whole-rock Mg# in the Critical and Lower Main Zones is consistent with the data that have been presented by others working on the Bushveld Complex. The similarities with other limbs are also observed in the uniformity of the initial $^{87}\text{Sr}/^{86}\text{Sr}$ ratios and normal fractionation shown by decreasing of the calculated plagioclase An% in the Upper Main and Upper Zones.

Based on the aforementioned, the RLS of the Eastern Limb can be divided into an isotopically heterogeneous Integration Stage (spanning the Critical and Lower Main Zones) and an isotopically homogeneous Differentiation Stage (spanning the Upper Main and Upper Zones). Within the “Integration Stage”, where significant variations in initial $^{87}\text{Sr}/^{86}\text{Sr}$ ratios of plagioclase are recorded, there is limited variation in the calculated plagioclase An% compared to the “Differentiation Stage”, which is characterized by a dominantly normal differentiation trend shown by decreasing calculated plagioclase An% with increasing stratigraphic height and limited variation in initial $^{87}\text{Sr}/^{86}\text{Sr}$ ratios of plagioclase.

The isotopically homogeneous “Differentiation Stage” is characterized by relatively uniform initial $^{87}\text{Sr}/^{86}\text{Sr}$ composition of ~0.7073. Limited variation in Sr-isotopic compositions suggests that this stratigraphic interval was formed through fractional crystallization with limited or no injections of new magma. The last major addition of magma into the Bushveld magma chamber is recorded by fluctuations in the calculated plagioclase An% and initial $^{87}\text{Sr}/^{86}\text{Sr}$ ratios at the level of the Pyroxenite Marker, which occurs at the boundary between the Lower and Upper Main zones.

Inter- and intra-crystal initial $^{87}\text{Sr}/^{86}\text{Sr}$ disequilibrium is locally observed in the Lower Main and Upper Critical Zones and is limited in the Upper Main and Upper Zones. This disequilibrium supports a model of petrogenesis which suggests that the Critical Zone and Lower Main Zones formed through intrusion of variably contaminated crystal mushes derived from a sub-compartmentalized, sub-Bushveld staging chamber that underwent different degrees of contamination with crustal rocks of the

Kaapvaal craton. The Upper Main and Upper Zones revealed uniform initial $^{87}\text{Sr}/^{86}\text{Sr}$ compositions with a decreasing calculated plagioclase An% trend, suggesting normal fractionation as the main petrogenetic process.

7. References

- Ashwal, L. D., Webb, S. J. & Knoper, M. W. 2005. Magmatic stratigraphy in the Bushveld Northern Lobe: continuous geophysical and mineralogical data from the 2950 m Bellevue drill core. *South African Journal of Geology*, 108, 199-232.
- Boorman, S., Boudreau, A. & Kruger, F. J. 2004. The Lower Zone – Critical Zone transition of the Bushveld Complex: a quantitative textural study. *Journal of Petrology*, 45 (6), 1209-1235.
- Cameron, E. N. 1978. The Lower Zone of the eastern Bushveld Complex in the Olifants River Trough. *Journal of Petrology*, 19, 437–462.
- Cameron, E. N. 1980. Evolution of the lower Critical Zone, central sector, eastern Bushveld Complex, and its chromite deposits. *Economic Geology*, 75, 845-871.
- Cameron, E. N. & Abendroth, H. E. 1957. Structure of lopoliths: discussion. *Bulletin of the Geological Society of South Africa*, 79, 3-12.
- Cawthorn, R. G. 2005. Pressure fluctuations and the formation of the PGE-rich Merensky and chromitite reefs, Bushveld Complex. *Mineralium Deposita*, 40, 231-235.
- Cawthorn, R. G., Meyer, P. S. & Kruger, F. J. 1991. Major addition of magma at the Pyroxenite Marker in the western Bushveld Complex, South Africa. *Journal of Petrology*, 32, 739-763.
- Cawthorn, R. G. & Walraven, F. 1998. Emplacement and crystallization time for the Bushveld Complex. *Journal of Petrology*, 39 (9), 1669-1687.
- Chutas, N. I., Bates, E., Prevec, S. A., Coleman, D. S. & Boudreau, A. E. 2012. Sr and Pb isotopic disequilibrium between coexisting plagioclase and orthopyroxene in the Bushveld Complex, South Africa: microdrilling and progressive leaching evidence for subliquidus contamination within a crystal mush. *Contributions to Mineralogy and Petrology*, 163 (4), 653-668.
- de Waal, S. A., Maier, W. D., Armstrong, R. A. & Gauert, C. D. 2001. Parental magma and emplacement of the stratiform Uitkomst Complex, South Africa. *Canadian Mineralogist*, 39 (2), 557-571.

Eales, H. V. & Cawthorn, R. G. 1996. *The Bushveld Complex*. In: Cawthorn RG (edi) Layered intrusions. Elsevier, Amsterdam, 181–229.

Eales, H. V., de Klerk, W. J., Butcher, A. R. & Kruger, F. J. 1990. The cyclic unit beneath the UG1/chromitite (UG1FW unit) at R.P.M Union Section Mine, Rosetta Stone of the Bushveld Upper Critical Zone. *Mineralogical Magazine*, 54, 23-43.

Eales, H. V., Marsh, J. S., Mitchell, A. A., De Klerk, W. J., Kruger, F. J. & Field, M. 1986. Some geochemical constraints upon models for the crystallization of the Upper Critical Zone-Main Zone interval, northwestern Bushveld Complex. *Mineralogical Magazine*, 50, 567-582.

Elburg, M., Vroon, P., van der Wagt, B. & Tchalikian, A. 2005. Sr and Pb isotopic composition of five USGS glasses (BHVO-2G,BIR-1G,BCR-2G, TB-1G, NKT-1G). *Chemical Geology*, 223, 196-207.

Field, M. 1987. *The petrology and geochemistry of the upper Critical Zone of the Bushveld Complex at the Amandelbult Section of Rustenburg Platinum Mines Ltd., northwestern Transvaal, South Africa*. M.Sc. thesis (unpubl.), Rhodes University, Grahamstown, 129.

Fischer, L. A, & Yuan, Q. 2016. Fe-Ti-V-(P) resources in the Upper Zone of the Bushveld Complex, South Africa. *Papers and Proceedings of the Royal Society of Tasmania*. 150 (1), 2016.

Grobler, D. F., Brits, J. A. N., Maier, W. D. & Crossing, A. 2019. Litho- and chemostratigraphy of the Flatreef PGE deposit, northern Bushveld Complex. *Mineralium Deposita*, 54 (1), 335-428.

Hall, A. L. 1932. The Bushveld Igneous Complex of the central Transvaal. *Memoir of the Geological Survey of South Africa*, 28, 530.

Harmer, R. E. & Armstrong, R. A. 2000. *Duration of the Bushveld Complex (seno lato) magmatism: constraints from new SHRIMP zircon chronology*. Abstracts and program, Workshop on the Bushveld Complex, Gethane Lodge, Burgersfort, South Africa.

Hulbert, L. J. 1983. *A petrographical investigation of the Rustenburg Layered Suite and associated mineralisation south of Potgietersrus*. DSc thesis, University of Pretoria.

Hulbert, L. J. & von Grunewaldt, G. 1982. Nickel, cooper, and platinum mineralization in the Lower Zone of the Bushveld Complex, south of Potgietersrus. *Economic Geology*, 77, 1296-1306.

Karykowski, B. T., Yang, S. H., Maier, W. D., Lahaye, Y., Lissenberg, C. J. & O'Brien, H. 2017. In situ Sr isotope compositions of plagioclase from a complete stratigraphic profile of the Bushveld Complex, South Africa: evidence for extensive magma mixing and percolation. *Journal of Petrology*, 58 (11), 2285-2308.

Kinnaird, J. A. 2005. Geochemical evidence for multiple emplacement in the southern Platreef. *Applied Earth Science*, 114, 225–242.

Kinnaird, J. A., Hutchinson, D., Schurmann, L., Nex, P. A. M. & De Lange, R. 2005. Petrology and mineralisation of the southern Platreef: Northern Limb of the Bushveld Complex, South Africa. *Mineralium Deposita*, 40, 576-597.

Kruger, F. J. 1989. *The geochronology and Sr-isotope geochemistry of the Molopo Farms Complex, Bushveld magmatic province: a preliminary report*. Molopo Botswana (Pvt) Ltd, Final Report, prospecting Licences 14/85 and 38/90, Open File Report, Geological Survey, Botswana.

Kruger, F. J. 1990. The stratigraphy of the Bushveld Complex: a re-appraisal and the relocation of the Main Zone boundaries. *South African Journal of Geology*, 93, 376-381.

Kruger, F. J. 1994. The Sr-isotopic stratigraphy of the western Bushveld Complex. *South African Journal of Geology*, 97, 393-398.

Kruger, F. J. 2005. Filling the Bushveld Complex magma chamber: lateral expansion, roof and floor interaction, magmatic unconformities, and the formation of giant chromitite, PGE and Ti-V-magnetite deposits. *Mineralium Deposita*, 40, 451-472.

Kruger, F. J. & Marsh, J. S. 1982. Significance of $^{87}\text{Sr}/^{86}\text{Sr}$ ratios in the Merensky cyclic unit of the Bushveld Complex. *Nature*, 298, 53–55.

- Kruger, F. J., Cawthorn, R. G. & Walsh, K. L. 1987. Strontium isotopic evidence against magma addition in the Upper Zone of the Bushveld Complex. *Earth and Planetary Science Letters*, 84, 51–58.
- Latypov, R. M. 2009. Testing the validity of the petrological hypothesis ‘no phenocrysts, no post-emplacement differentiation’. *Journal of Petrology*, 50, 1047–106.
- Latypov, R., Chistyakova, S., Page, A. & Hornsey, R. 2016. Field Evidence for the in-situ crystallization of the Merensky Reef. *Journal of Petrology*, 56 (12), 2341-2372.
- Latypov, R., Costin, G., Chistyakova, S., Hunt, E. J., Mukherjee, R. & Naldrett, T. 2018. Platinum-bearing chromite layers are caused by pressure reduction during magma ascent. *Nature Communications*, 9 (462).
- Lee, C. A. & Butcher, A. R. 1990. Cyclicity in the Sr isotope stratigraphy through the Merensky and Bastard Reefs, Atok Section, eastern Bushveld Complex. *Economic Geology*, 85, 877-883.
- Maier, W. D., Arndt, N. T. & Curl, E. A. 2000. Progressive crustal contamination of the Bushveld Complex: evidence from Nd isotopic analyses of the cumulate rocks. *Contributions to Mineralogy and Petrology*, 140, 316-327.
- Maier, W. D., Barnes, S. -J. & Van der Merwe, M. J. 2001. Platinum-group elements in the Pyroxenite Marker, Bushveld Complex: implications for the formation of the Main Zone. *South African Journal of Geology*, 104, 301-308.
- Maier, W. D., Barnes, S. -J. & Groves, D. I. 2013. The Bushveld Complex, South Africa: formation of platinum–palladium, chrome and vanadium-rich layers via hydrodynamic sorting of a mobilized cumulate slurry in a large, relatively slowly cooling, subsiding magma chamber. *Mineralium Deposita*, 48, 1-56.
- Maier, W.D., Yudovskaya, M. & Jugo, P. 2021. Introduction to the special issue on the Flatreef PGE-Ni-Cu deposit, Northern Limb of the Bushveld Igneous Complex. *Mineralium Deposita*. 56, 1-10
- Mangwegape, M., Roelofse, F., Mock, T. & Carlson, R. W. 2016. The Sr-isotopic stratigraphy of the Northern Limb of the Bushveld Complex, South Africa. *Journal of African Earth Sciences*, 113, 95–100.

Mapeo, R. B., Kampuznu, A. B., Ramokate, L. V., Corfu, F. & Key, R. M. 2004. Bushveld-age magmatism in southeastern Botswana: evidence from U-Pb zircon and titanite geochronology of the Moshaneng Complex. *South African Journal of Geology*, 107, 219-232.

Marsh, B. D. 2013. On some fundamentals of igneous petrology. *Contributions to Mineralogy and Petrology*, 166, 665–690.

McDonald, I. & Holwell, D. A. 2011. Geology of the northern Bushveld Complex and the setting and genesis of the Platreef Ni–Cu–PGE deposit. In Li C, Ripley EM (eds) Magmatic Ni–Cu and PGE deposits: geology, geochemistry, and genesis. *Economic Geology*, 17, 297–327.

McDonald, I., Holwell, D. A. & Armitage, P. E. B. 2005. Geochemistry and mineralogy of the Platreef and ‘Critical Zone’ of the Northern Lobe of the Bushveld Complex, South Africa: implications for Bushveld stratigraphy and the development of PGE mineralization. *Mineralium Deposita*, 40, 526-549.

Mitchell, A. A. 1990. The stratigraphy, petrography and mineralogy of the Main Zone of the northwestern Bushveld Complex. *South African Journal of Geology*, 93, 818-831.

Nebel, O., Scherer, E. E. & Mezger, K. 2011. Evaluation of the ^{87}Rb decay constant by age comparison against the U-Pb system. *Earth and Planetary Science Letters*, 301, 1-8.

Raedeke, L. D. & McCallum, I. S. 1984. Investigations in the Stillwater Complex: Part II. Petrology and petrogenesis of the ultramafic series. *Journal of Petrology*, 25 (2), 395-420.

Rasbury, E. T., Present, T. M., Northrup, P., Tappero, R. V., Lanzilliotti, A., Cole, J. M., Wooton, K. M. & Hatton, K. 2021. Tools for uranium characterization in carbonate samples: case studies of natural U–Pb geochronology reference materials. *Geochronology*, 3, 103-122.

Reed, S. J. B. 2005. *Electron microprobe analysis and scanning electron microscopy in geology*, 2nd edn, Cambridge University Press, New York.

Roelofse, F. 2010. *Constraints on the magmatic evolution of the lower Main Zone and Platreef on the Northern Limb of the Bushveld Complex as inferred from the Moordkopje drill core*. Ph.D. Thesis. University of the Witwatersrand.

Roelofse, F. & Ashwal, L. D. 2012. The Lower Main Zone in the Northern Limb of the Bushveld Complex — a >1.3 km thick sequence of intruded and variably contaminated crystal mushes. *Journal of Petrology*, 53, 1449–1476.

Roelofse, F., Ashwal, L. D. & Romer, R. L. 2015. Multiple, isotopically heterogeneous plagioclase populations in the Bushveld Complex suggest mush intrusion. *Chemie der Erde*, 75, 357–364.

Scoates, J. S. & Friedman, R. M. 2008. Precise age of the planitiferous Merensky Reef, Bushveld Complex, South Africa, by the U-Pb zircon chemical abrasion ID-TIMS technique. *Economic Geology*, 103, 465-471.

Scoon, R. N. & Viljoen, M. J. 2019. Geoheritage of the Eastern Limb of the Bushveld Igneous Complex, South Africa: a uniquely exposed layered igneous intrusion. *Geoheritage*, 11, 1723-1748.

Seabrook, C. L., Cawthorn, R. G. & Kruger, F. J. 2005. The Merensky Reef, Bushveld Complex: mixing of minerals not mixing of magmas. *Economic Geology*, 100, 1191-1206.

Sharpe, M. R. 1985. Strontium isotope evidence for preserved density stratification in the Main Zone of the Bushveld Complex, South Africa. *Nature*, 316, 119-126.

Tanner, D., Mavrogenes, J. A., Arculus, R. J. & Jenner, F. E. 2014. Trace element stratigraphy of the Bellevue core, northern Bushveld: Multiple magma injections obscured by diffusive processes. *Journal of Petrology*, 55 (5), 859-883.

Tegner, C., Cawthorn, R. G. & Kruger, F. J. 2006. Cyclicity in the Main and Upper Zones of the Bushveld Complex, South Africa: Crystallization from a zoned magma sheet. *Journal of Petrology*, 47, 2257-2279.

Van der Merwe, M. J. 1976. The Layered Sequence of the Potgietersrus Limb of the Bushveld Complex. *Economic Geology*, 71, 1337-1351.

Von Gruenewaldt, G. 1971. *A petrographical and mineralogical investigation of the rocks of the Bushveld Igneous Complex in the Tauteshoogte-Roossenekal area of the eastern Transvaal*. DSc thesis, University of Pretoria.

Wilson, A. H. 2011. *Early magma emplacement stages of the Bushveld Complex and Great Dyke*. In: Knoper, M. (edi.) 23rd Colloquium of African Geology. University of Johannesburg.

Wilson, A. H., Zeh, A. & Gerdes, A. 2017. In situ Sr isotopes in plagioclase and trace element systematics in the lowest part of the eastern Bushveld Complex: dynamic Processes in an evolving magma chamber. *Journal of Petrology*, 58 (2), 327-360.

Yang, S. H., Maier, W. D., Lahaye, Y. & O'Brien, H. 2013. Strontium isotope disequilibrium of plagioclase in the Upper Critical Zone of the Bushveld Complex: evidence for mixing of crystal slurries. *Contributions to Mineralogy and Petrology*, 166, 959-974.

Yudovskaya, M. A., Kinnaird, J. A., Sobolev, A. V., Kuzmin, D. V., McDonald, I. & Wilson, A. H. 2013. Petrogenesis of the Lower Zone olivine-rich cumulates beneath the Platreef and their correlation with recognized occurrences in the Bushveld Complex. *Economic Geology*, 108, 1923-1952.

Yudovskaya, M. A., Kinnaird, J. A., Grobler, D. F., Costin, G., Abramova, V. D., Dunnett, T. & Barnes, S. J. 2017. Zonation of Merensky-Style Platinum-Group Element Mineralization in Turfspruit Thick Reef Facies (Northern Limb of the Bushveld Complex). *Economic Geology*, 112, 1333-1365.

Zeh, A., Ovtcharova, M., Wilson, A. H. & Schaltegger, U. 2015. The Bushveld Complex was emplaced and cooled in less than one million years - results of zirconology, and geotectonic implications. *Earth and Planetary Science Letters*, 418, 103-114.

8. Appendices

Appendix A1: Whole-rock major element data in weight% of samples from the LCZ to the UZ, with LOI and Mg#.

Sample	Zone	Depth(m)	SiO ₂	TiO ₂	Al ₂ O ₃	Fe ₂ O ₃	MgO	MnO	CaO	K ₂ O	P ₂ O ₅	Na ₂ O	Cr ₂ O ₃	LOI	Total	Mg#
TM1.1	UZ	65.66	44,68	2,43	13,17	26,12	2,25	0,38	8,91	0,47	0,90	2,30	0,00	-0,03	101,60	0,15
TM1.2	UZ	138.77	40,14	3,12	12,13	27,65	3,66	0,33	7,86	0,48	2,07	1,19	0,00	-0,01	98,62	0,21
TM1.4	UZ	226.74	46,18	2,93	20,95	14,51	0,93	0,10	9,06	0,59	0,14	3,04	0,00	-0,01	98,43	0,11
TM1.5	UZ	318.47	47,11	2,93	16,86	15,45	3,21	0,16	10,70	0,33	0,04	2,38	0,00	0,00	99,16	0,29
TM1.6	UZ	418.31	39,78	2,61	12,61	26,17	5,61	0,28	9,57	0,24	2,50	2,31	0,00	-0,04	101,68	0,30
TM1.7	UZ	524.44	45,75	2,69	12,18	20,15	5,79	0,24	10,31	0,28	0,04	1,95	0,00	-0,01	99,38	0,36
TM1.8	UZ	603.78	39,80	4,12	13,95	25,53	4,73	0,19	9,39	0,18	0,02	1,92	0,00	-0,02	99,81	0,27
TM1.9	UZ	711.43	49,85	1,24	18,26	13,80	5,75	0,17	8,80	0,28	0,02	2,60	0,00	-0,01	100,75	0,45
TM1.10	UZ	812.53	42,57	3,42	19,56	21,22	2,15	0,12	8,55	0,26	0,02	2,62	0,00	-0,02	100,50	0,17
TM1.11	UZ	911.78	45,23	2,20	13,78	20,75	6,99	0,21	9,53	0,26	0,03	2,30	0,00	-0,02	101,28	0,40
TM1.12	UZ	1005.31	46,43	2,13	20,50	15,23	2,57	0,11	10,20	0,35	0,03	2,76	0,00	-0,01	100,31	0,25
TM1.13	UZ	1104.46	45,57	0,57	19,91	14,77	7,72	0,12	9,21	0,22	0,02	2,33	0,00	0,00	100,42	0,51
TM1.13 1	UMZ	1201.54	50,40	0,20	13,84	10,65	9,95	0,20	11,85	0,14	0,01	1,03	0,00	0,01	98,27	0,65
TM1.13 2	UMZ	1299.49	51,52	0,17	22,62	5,86	5,78	0,10	11,83	0,34	0,04	1,50	0,00	0,01	99,76	0,66

Sample	Zone	Depth(m)	SiO ₂	TiO ₂	Al ₂ O ₃	Fe ₂ O ₃	MgO	MnO	CaO	K ₂ O	P ₂ O ₅	Na ₂ O	Cr ₂ O ₃	LOI	Total	Mg#
TM1.13.3	UMZ	1349.35	50,58	0,17	20,07	6,38	5,70	0,16	12,16	0,23	0,02	2,39	0,00	0,18	97,84	0,64
TM1.13.4	UMZ	1447.51	51,78	0,21	15,14	8,21	9,79	0,17	13,72	0,11	0,01	1,80	0,00	0,13	100,93	0,70
TM1.14	UMZ	1519.05	50,73	0,22	28,40	2,70	1,03	0,04	13,21	0,28	0,04	2,57	0,00	0,00	99,22	0,43
TM1.15	UMZ	1616.47	51,08	0,21	17,21	6,88	9,44	0,13	12,80	0,21	0,02	1,57	0,00	0,01	99,56	0,73
TM1.16	UMZ	1695.81	51,09	0,16	18,62	8,55	9,20	0,15	11,04	0,20	0,02	1,48	0,00	0,00	100,50	0,68
TM1.16.1	UMZ	1757.02	52,57	0,26	4,76	15,98	20,26	0,30	5,94	0,09	0,02	0,70	0,00	-0,18	100,87	0,72
TM1.17	LMZ	1782.05	51,82	0,13	14,80	10,64	12,27	0,21	9,45	0,11	0,01	1,53	0,00	0,00	100,96	0,70
TM1.18	LMZ	1879.26	53,03	0,17	18,11	7,37	7,36	0,15	12,39	0,22	0,01	1,76	0,00	0,00	100,55	0,66
TM1.19	LMZ	1978.02	52,71	0,16	17,90	7,11	7,33	0,14	12,41	0,21	0,02	1,89	0,00	0,00	99,89	0,67
TM1.20	LMZ	2076.38	51,37	0,10	19,14	6,06	6,78	0,13	12,59	0,13	0,01	2,42	0,00	0,00	98,72	0,69
TM1.21	LMZ	2182.20	52,12	0,12	17,39	7,25	8,34	0,15	12,41	0,12	0,01	2,07	0,00	0,01	99,97	0,70
TM1.22	LMZ	2274.98	53,16	0,21	18,51	6,50	7,29	0,13	13,10	0,28	0,02	1,96	0,00	0,00	101,16	0,69
TM1.23	LMZ	2352.82	54,93	0,19	15,04	8,33	8,97	0,16	11,67	0,24	0,02	1,78	0,00	0,00	101,33	0,68
TM1.24	LMZ	2448.40	53,13	0,22	16,23	7,70	8,61	0,16	13,58	0,25	0,03	1,81	0,00	0,03	101,71	0,69
TM1.25	LMZ	2543.73	52,58	0,26	20,75	6,77	6,42	0,12	12,44	0,33	0,09	2,18	0,00	0,00	101,93	0,65
TM1.26	LMZ	2639.06	52,69	0,17	18,27	6,81	8,17	0,14	12,44	0,23	0,02	1,97	0,00	0,00	100,90	0,70
TM1.27	LMZ	2736.76	52,42	0,19	17,73	7,45	8,60	0,15	11,09	0,30	0,03	1,92	0,00	0,01	99,87	0,70
TM1.28	LMZ	2841.74	51,98	0,19	19,24	5,93	7,23	0,12	13,12	0,30	0,03	1,52	0,00	0,01	99,64	0,71

Sample	Zone	Depth(m)	SiO ₂	TiO ₂	Al ₂ O ₃	Fe ₂ O ₃	MgO	MnO	CaO	K ₂ O	P ₂ O ₅	Na ₂ O	Cr ₂ O ₃	LOI	Total	Mg#
TM1.29	LMZ	2938.23	52,48	0,18	19,13	5,83	8,07	0,12	11,99	0,34	0,03	2,07	0,00	0,01	100,23	0,73
TM1.30	LMZ	3035.77	51,88	0,19	15,29	7,12	10,61	0,14	12,22	0,25	0,02	1,65	0,00	0,01	99,37	0,75
TM1.31	LMZ	3134.33	53,32	0,25	17,26	6,83	8,84	0,13	12,10	0,48	0,05	0,94	0,00	0,01	100,19	0,72
TM1.32	LMZ	3230.89	52,97	0,24	26,63	2,81	2,53	0,05	12,94	0,55	0,05	2,20	0,00	0,01	100,96	0,64
TM1.33	LMZ	3329.37	51,34	0,22	20,10	6,51	8,36	0,12	10,84	0,15	0,04	1,19	0,00	0,16	98,85	0,72
TM1.34	LMZ	3427.93	52,36	0,21	16,23	7,43	10,22	0,14	11,05	0,28	0,03	1,68	0,00	0,00	99,63	0,73
TM1.35	LMZ	3525.27	51,81	0,17	18,52	6,33	8,55	0,12	11,36	0,28	0,02	2,12	0,00	0,00	99,29	0,73
TM1.36	LMZ	3618.98	52,37	0,19	20,53	6,12	7,39	0,11	11,18	0,36	0,03	2,16	0,00	0,00	100,43	0,71
TM1.37	LMZ	3710.10	52,42	0,21	21,40	5,58	6,49	0,10	11,36	0,41	0,03	2,17	0,00	0,01	100,16	0,70
TM1.38	LMZ	3795.28	52,01	0,18	20,43	5,90	8,61	0,11	11,68	0,27	0,02	1,95	0,00	0,03	101,15	0,74
TM1.39	UCZ	3893.44	48,96	0,08	27,01	2,17	3,21	0,05	14,74	0,12	0,02	1,68	0,00	0,07	98,03	0,74
TM1.39.1	UCZ	3972.90	51,62	0,08	17,32	5,52	11,26	0,12	13,07	0,04	0,01	1,85	0,00	0,05	100,89	0,80
TM1.40	UCZ	4238.37	50,47	0,06	24,79	3,94	6,74	0,07	12,56	0,10	0,01	0,94	0,00	0,01	99,66	0,77
TM1.40.1	UCZ	4274.20	12,20	0,56	12,83	26,90	8,22	0,20	1,79	0,00	0,01	0,40	39,90	-1,42	103,02	0,38
TM1.41	UCZ	4335.85	49,27	0,05	28,27	2,31	3,63	0,04	13,95	0,12	0,01	1,93	0,00	0,01	99,56	0,76
TM1.42	UCZ	4434.09	52,14	0,08	18,14	6,38	10,35	0,13	11,97	0,07	0,01	1,79	0,00	0,00	101,07	0,76
TM1.43	UCZ	4532.20	51,27	0,10	14,18	8,36	15,29	0,16	8,41	0,04	0,01	1,47	0,00	0,00	99,28	0,78
TM1.44	UCZ	4654.76	53,29	0,13	4,33	13,20	25,97	0,24	3,77	0,00	0,01	0,55	0,00	-0,01	101,48	0,80

Sample	Zone	Depth(m)	SiO ₂	TiO ₂	Al ₂ O ₃	Fe ₂ O ₃	MgO	MnO	CaO	K ₂ O	P ₂ O ₅	Na ₂ O	Cr ₂ O ₃	LOI	Total	Mg#
TM1.45	UCZ	4753.11	51,19	0,25	11,32	9,50	18,49	0,17	6,75	0,05	0,01	1,03	0,00	0,00	98,75	0,79
TM1.46	UCZ	4826.62	49,99	0,09	22,28	5,57	9,05	0,10	11,58	0,08	0,01	1,65	0,00	0,01	100,39	0,76
TM1.46.3	LCZ	4875.72	1,65	0,71	14,08	31,50	6,82	0,22	0,23	0,00	0,01	0,14	45,50	-1,81	100,85	0,30
TM1.47	LCZ	4924.39	52,64	0,19	3,07	11,03	26,58	0,20	3,80	0,15	0,02	0,54	0,00	0,00	98,23	0,83
TM1.47.1	LCZ	4942.93	16,35	0,56	10,41	19,99	14,74	0,24	0,63	0,00	0,00	0,13	38,50	-1,42	101,54	0,59
TM1.47.2	LCZ	4968.64	5,89	0,61	7,98	29,30	6,59	0,23	0,31	0,00	0,01	0,15	49,42	-1,56	100,49	0,31
TM1.47.4	LCZ	4982.25	9,71	0,56	7,32	27,10	8,73	0,26	0,46	0,00	0,01	0,15	45,10	-0,54	99,39	0,39
TM1.48	LCZ	4991.09	52,60	0,14	2,10	9,50	29,60	0,21	2,25	0,00	0,01	0,34	0,00	-0,01	96,72	0,86

Appendix A2: Whole-rock trace element data in ppm of samples covering the LCZ to the UZ.

Sample	Zone	Depth (m)	Sc	V	Cr	Co	Ni	Cu	Zn	As	Rb	Sr	Y	Zr	Nb	Ba	Pb	Th	U
TM1.1	UZ	65.66	38	13	13	64	<4	34	163	10	7	361	35	55	8	314	<2	4	<3
TM1.2	UZ	138.77	14	37	26	88	7	59	161	20	10	337	44	57	6	284	<2	10	4
TM1.4	UZ	226.74	15	282	95	44	51	86	91	6	12	449	11	29	5	266	<2	3	<3
TM1.5	UZ	318.47	37	56	19	36	9	5	71	2	4	390	7	10	2	153	2	<3	<3
TM1.6	UZ	418.31	18	41	8	105	<4	144	121	7	2	281	21	7	1	124	<2	5	<3
TM1.7	UZ	524.44	43	261	<4	71	29	101	98	7	6	270	13	24	3	157	<2	7	3
TM1.8	UZ	603.78	37	804	41	112	60	573	104	16	3	240	11	19	3	124	<2	8	<3
TM1.9	UZ	711.43	21	221	7	53	19	7	76	<1	4	339	4	14	2	140	15	<3	<3
TM1.10	UZ	812.53	17	1013	46	88	63	496	141	15	3	377	7	16	4	161	<2	7	<3
TM1.11	UZ	911.78	42	738	<4	99	41	230	94	3	5	240	10	24	2	132	<2	3	<3
TM1.12	UZ	1005.31	19	908	<4	54	101	335	68	1	7	343	7	19	2	179	6	<3	4
TM1.13	UZ	1104.46	12	357	50	80	16	25	76	<1	2	304	2	10	1	118	27	<3	<3
TM1.13.1	UMZ	1201.54	41	180	25	53	142	152	76	<1	6	226	6	9	1	79	21	<3	<3
TM1.13.2	UMZ	1299.49	15	45	73	18	94	13	42	<1	10	304	3	16	2	110	26	<3	<3
TM1.13.3	UMZ	1349.35	26	81	74	25	120	141	43		5	301	6	19	2	107	13	<3	<3
TM1.13.4	UMZ	1447.51	41	130	151	34	174	73	47		2	214	8	17	1	53	14	<3	<3
TM1.14	UMZ	1519.05	9	16	7	2	11	16	16	<1	5	378	4	19	2	105	8	<3	<3
TM1.15	UMZ	1616.47	30	98	272	28	181	30	44	<1	6	222	7	24	2	71	15	<3	<3
TM1.16	UMZ	1695.81	22	67	176	36	196	16	51	<1	5	259	4	17	2	76	19	<3	<3
TM1.16.1	UMZ	1757.02	44	188	843	108	381	25	108		5	65	6	19	2	25	15	<3	<3
TM1.17	LMZ	1782.05	29	100	564	53	236	11	85	<1	2	216	3	11	1	51	15	<3	<3
TM1.18	LMZ	1879.26	30	129	17	26	95	9	39	<1	3	288	5	15	2	89	20	<3	<3
TM1.19	LMZ	1978.02	30	140	28	28	108	7	43	<1	4	287	5	14	2	53	16	<3	<3
TM1.20	LMZ	2076.38	26	97	28	22	106	4	35	<1	<2	306	3	6	1	38	11	<3	<3
TM1.21	LMZ	2182.20	32	112	49	31	138	<4	44	<1	2	262	4	7	1	44	13	<3	<3

Sample	Zone	Depth (m)	Sc	V	Cr	Co	Ni	Cu	Zn	As	Rb	Sr	Y	Zr	Nb	Ba	Pb	Th	U
TM1.22	LMZ	2274.98	32	124	31	23	127	13	42	<1	7	272	8	22	2	106	16	<3	<3
TM1.23	LMZ	2352.82	33	132	20	31	160	14	50	<1	5	244	7	19	2	71	15	<3	<3
TM1.24	LMZ	2448.40	36	157	40	33	200	46	102	<1	6	232	9	23	1	99	10	<3	<3
TM1.25	LMZ	2543.73	23	89	34	20	126	11	46	<1	8	281	5	21	1	96	12	<3	4
TM1.26	LMZ	2639.06	27	101	44	26	163	15	52	<1	5	255	6	18	2	85	14	<3	<3
TM1.27	LMZ	2736.76	22	87	46	31	178	16	57	<1	8	241	7	26	2	93	12	<3	<3
TM1.28	LMZ	2841.74	22	87	52	21	137	14	61	<1	8	264	6	25	2	92	21	<3	<3
TM1.29	LMZ	2938.23	21	87	47	22	146	20	60	<1	9	276	7	24	3	94	11	3	<3
TM1.30	LMZ	3035.77	31	111	270	28	217	16	49	<1	8	209	7	26	2	81	12	<3	<3
TM1.31	LMZ	3134.33	21	94	158	22	163	17	42	<1	16	240	8	42	2	127	24	<3	<3
TM1.32	LMZ	3230.89	11	36	32	4	55	9	28	1	15	316	7	41	3	142	6	<3	<3
TM1.33	LMZ	3329.37	25	95	273	29	203	9	99	<1	5	249	7	33	2	63	9	<3	<3
TM1.34	LMZ	3427.93	25	114	326	32	230	18	60	<1	9	211	7	31	2	104	16	<3	<3
TM1.35	LMZ	3525.27	24	89	292	25	198	16	53	<1	7	255	6	24	2	103	18	<3	<3
TM1.36	LMZ	3618.98	18	75	235	23	172	24	52	<1	9	264	7	27	2	112	15	<3	<3
TM1.37	LMZ	3710.10	16	69	223	19	147	19	46	<1	11	278	7	35	2	121	11	<3	<3
TM1.38	LMZ	3795.28	20	69	313	21	183	14	51	<1	6	271	5	22	2	85	9	<3	<3
TM1.39	UCZ	3893.44	15	28	221	<3	81	8	42	1	<2	300	4	11	2	58	4	3	<3
TM1.39.1	UCZ	3972.90	24	82	622	23	262	2	44	<2	281	3	5	1	22	9	<3	<3	
TM1.40	UCZ	4238.37	15	23	530	13	164	7	29	<1	2	391	1	6	2	42	17	<3	<3
TM1.40.1	UCZ	4274.20	13	2369		73	767	30	553	<2	47	<1	8	2	<7	69	<3	<3	
TM1.41	UCZ	4335.85	11	9	469	4	84	4	18	<1	<2	399	2	6	2	56	7	<3	<3
TM1.42	UCZ	4434.09	21	82	656	28	227	<4	42	<1	<2	280	3	7	1	25	17	<3	<3
TM1.43	UCZ	4532.20	19	97	968	50	352	7	55	<1	<2	218	2	8	1	24	16	<3	4
TM1.44	UCZ	4654.76	34	135	2253	98	556	<4	87	<1	<2	60	4	8	1	26	14	<3	<3
TM1.45	UCZ	4753.11	22	101	1813	59	398	8	65	<1	<2	176	2	9	1	29	14	<3	<3
TM1.46	UCZ	4826.62	17	113	6187	21	209	7	48	<1	<2	320	2	8	1	53	19	<3	<3
TM1.46.3	LCZ	4875.72	9	1942		82	884	41	607	<2	4	<1	7	1	<7	73	<3	<3	
TM1.47	LCZ	4924.39	28	111	2291	89	574	26	76	<1	5	38	5	21	2	81	8	<3	<3

Sample	Zone	Depth (m)	Sc	V	Cr	Co	Ni	Cu	Zn	As	Rb	Sr	Y	Zr	Nb	Ba	Pb	Th	U
TM1.47.1	LCZ	4942.93	16	1822		77	723	29	488		<2	4	<1	6	1	<7	65	<3	<3
TM1.47.2	LCZ	4968.64	8	1886		66	734	22	591		<2	6	<1	8	1	<7	86	<3	<3
TM1.47.4	LCZ	4982.25	10	1541		66	668	21	588		<2	8	<1	9	2	<7	77	<3	<3
TM1.48	LCZ	4991.09	29	125	8038	89	537	15	75	<1	<2	17	2	10	1	15	14	<3	<3

Appendix B: The major element composition of plagioclase per analysed spot in weight %, including the calculated anorthite content (An%) of plagioclase.

Depth	Sample	Zone	Plag													
			NO:	Point	SiO ₂	Al ₂ O ₃	CaO	MgO	FeO	MnO	Cr ₂ O ₃	TiO ₂	Na ₂ O	K ₂ O	Total	An%
65.66	TM 1.1	UZ	1	1	57.28	26.41	9.18	n.d	0.16	n.d	n.d	0.05	6.22	0.44	99.74	43.85
65.66		UZ	1	2	57.60	26.30	8.75	n.d	0.17	n.d	0.02	0.04	6.35	0.48	99.72	42.03
65.66		UZ	1	3	58.10	25.81	8.33	0.01	0.20	n.d	n.d	0.03	6.39	0.55	99.42	40.54
65.66		UZ	1	4	57.95	25.78	8.50	n.d	0.17	n.d	n.d	0.04	6.49	0.50	99.43	40.86
65.66		UZ	1	5	57.11	26.79	9.27	0.02	0.45	0.01	n.d	n.d	6.03	0.46	100.15	44.71
65.66		UZ	2	6	57.04	26.46	9.23	n.d	0.19	n.d	n.d	0.02	6.18	0.43	99.56	44.11
65.66		UZ	2	7	56.08	26.69	9.59	0.03	0.67	n.d	n.d	0.03	5.82	0.44	99.35	46.44
65.66		UZ	2	8	56.42	26.60	9.68	0.01	0.22	0.01	0.02	0.05	5.92	0.46	99.39	46.22
65.66		UZ	2	9	57.39	26.17	8.90	0.01	0.17	0.01	n.d	0.02	6.34	0.39	99.39	42.72
65.66		UZ	2	10	56.45	26.60	9.44	0.02	0.16	n.d	0.01	0.03	5.93	0.49	99.13	45.47
65.66		UZ	3	11	56.39	26.91	9.75	n.d	0.19	n.d	n.d	0.06	6.02	0.43	99.75	46.03
65.66		UZ	3	12	57.22	26.29	9.13	n.d	0.19	0.01	0.01	0.01	6.22	0.50	99.58	43.51
65.66		UZ	3	13	56.68	26.31	9.40	0.01	0.19	n.d	n.d	0.02	6.05	0.51	99.17	44.86
65.66		UZ	3	14	56.93	26.44	9.18	n.d	0.15	n.d	n.d	0.02	6.25	0.46	99.43	43.64
65.66		UZ	3	15	56.90	26.20	9.01	0.04	0.48	0.01	n.d	0.03	6.19	0.45	99.31	43.42
65.66		UZ	4	16	57.81	25.99	8.50	n.d	0.20	n.d	0.01	0.01	6.42	0.57	99.52	40.86
65.66		UZ	4	17	57.52	25.96	8.69	0.01	0.17	0.02	n.d	0.02	6.47	0.46	99.34	41.49
65.66		UZ	4	18	57.07	26.18	8.80	n.d	0.18	n.d	n.d	n.d	6.21	0.55	98.99	42.55
65.66		UZ	4	19	57.52	26.11	8.81	n.d	0.17	n.d	0.01	n.d	6.32	0.48	99.43	42.31
65.66		UZ	4	20	56.96	26.37	9.15	n.d	0.14	0.01	0.02	0.02	6.01	0.54	99.22	44.28
65.66		UZ	5	21	57.70	26.11	8.82	0.01	0.22	0.01	n.d	0.04	6.41	0.48	99.79	42.03
65.66		UZ	5	22	57.53	26.17	8.76	n.d	0.18	n.d	n.d	0.04	6.32	0.52	99.52	41.94
65.66		UZ	5	23	56.57	26.71	9.54	0.01	0.21	0.01	n.d	0.01	6.02	0.44	99.52	45.52
65.66		UZ	5	24	56.81	26.59	9.18	0.01	0.26	0.01	n.d	0.04	6.18	0.46	99.53	43.90

Plag																
Depth	Sample	Zone	NO:	Point	SiO ₂	Al ₂ O ₃	CaO	MgO	FeO	MnO	Cr ₂ O ₃	TiO ₂	Na ₂ O	K ₂ O	Total	An%
65.66		UZ	5	25	57.44	26.28	8.97	0.01	0.26	n.d	n.d	n.d	6.29	0.52	99.76	42.78
65.66		UZ	6	26	56.87	26.37	9.27	n.d	0.20	n.d	n.d	0.04	6.10	0.48	99.33	44.47
65.66		UZ	6	27	56.83	26.17	9.05	n.d	0.17	n.d	n.d	0.03	6.23	0.52	99.00	43.22
65.66		UZ	6	28	55.90	26.23	9.15	0.01	0.23	n.d	n.d	0.05	5.90	0.49	97.95	44.84
65.66		UZ	6	29	56.42	26.66	9.49	0.01	0.17	0.02	n.d	0.03	5.93	0.44	99.16	45.73
65.66		UZ	6	30	56.93	26.45	9.22	0.02	0.20	0.01	n.d	0.03	6.11	0.46	99.43	44.26
138.77	TM 1.2	UZ	9	151	55.22	27.68	10.41	n.d	0.19	n.d	n.d	0.05	5.62	0.36	99.52	49.47
138.77		UZ	9	152	56.41	27.26	8.06	n.d	0.28	0.01	n.d	0.03	5.87	1.15	99.06	40.20
138.77		UZ	9	153	55.73	27.57	10.20	0.01	0.17	n.d	n.d	0.04	5.71	0.38	99.83	48.62
138.77		UZ	10	154	55.52	27.76	10.24	0.02	0.18	n.d	n.d	0.04	5.53	0.42	99.70	49.35
138.77		UZ	10	155	55.57	27.62	10.17	0.01	0.19	n.d	n.d	0.02	5.63	0.49	99.71	48.56
138.77		UZ	10	156	55.63	27.53	10.22	n.d	0.20	n.d	0.01	0.04	5.63	0.48	99.74	48.72
138.77		UZ	12	157	55.20	27.82	10.33	n.d	0.20	n.d	n.d	0.04	5.51	0.42	99.51	49.65
138.77		UZ	12	158	56.06	27.37	9.82	0.02	0.14	n.d	n.d	0.01	5.86	0.40	99.67	47.01
138.77		UZ	12	159	56.49	27.15	9.61	0.03	0.14	n.d	0.03	0.02	5.85	0.53	99.83	46.15
226.74	TM 1.4	UZ	13	31	55.34	27.56	10.37	n.d	0.21	n.d	0.02	0.01	5.58	0.32	99.42	49.74
226.74		UZ	13	32	55.05	27.71	10.50	0.01	0.16	0.01	0.02	n.d	5.43	0.28	99.16	50.81
226.74		UZ	13	33	55.05	27.56	10.51	n.d	0.22	0.02	0.01	0.02	5.36	0.36	99.12	50.92
226.74		UZ	13	34	54.45	27.97	11.05	n.d	0.20	n.d	n.d	0.03	5.17	0.24	99.12	53.42
226.74		UZ	13	35	55.08	27.52	10.70	n.d	0.22	n.d	n.d	0.04	5.39	0.35	99.28	51.26
226.74		UZ	14	36	54.72	28.01	10.90	n.d	0.16	0.02	n.d	0.02	5.30	0.28	99.43	52.34
226.74		UZ	14	37	54.90	27.84	10.53	0.01	0.15	n.d	0.01	0.01	5.47	0.29	99.20	50.67
226.74		UZ	14	38	55.22	27.33	10.32	0.02	0.19	0.01	n.d	0.04	5.46	0.37	98.96	50.00
226.74		UZ	14	39	54.66	27.87	11.07	n.d	0.18	0.01	n.d	0.02	5.19	0.30	99.30	53.18
226.74		UZ	14	40	55.39	27.53	10.52	n.d	0.23	n.d	n.d	0.03	5.45	0.35	99.50	52.29
226.74		UZ	15	41	55.38	27.49	10.45	0.01	0.19	n.d	n.d	0.04	5.46	0.40	99.42	50.23
226.74		UZ	15	42	55.05	27.71	10.75	0.01	0.21	0.01	n.d	n.d	5.35	0.35	99.42	51.57
226.74		UZ	15	43	54.94	27.71	10.61	0.01	0.22	n.d	n.d	0.05	5.27	0.41	99.22	51.41

Plag																
Depth	Sample	Zone	NO:	Point	SiO ₂	Al ₂ O ₃	CaO	MgO	FeO	MnO	Cr ₂ O ₃	TiO ₂	Na ₂ O	K ₂ O	Total	An%
226.74		UZ	15	44	55.47	27.71	10.48	n.d	0.11	0.01	n.d	0.03	5.37	0.47	99.65	50.50
226.74		UZ	15	45	55.31	27.68	10.60	0.02	0.21	n.d	0.01	0.04	5.37	0.41	99.65	50.94
226.74		UZ	16	46	55.17	27.77	10.82	n.d	0.18	n.d	0.01	0.03	5.25	0.38	99.62	52.09
226.74		UZ	16	47	55.24	27.45	10.60	0.01	0.20	0.01	n.d	0.03	5.35	0.40	99.28	51.08
226.74		UZ	16	48	54.95	27.67	10.72	0.01	0.23	n.d	0.02	0.04	5.23	0.38	99.24	51.96
226.74		UZ	16	49	55.23	27.64	10.50	0.01	0.18	n.d	0.02	0.03	5.38	0.35	99.33	50.84
226.74		UZ	16	50	54.55	27.91	10.86	n.d	0.18	n.d	n.d	0.03	5.20	0.31	99.05	52.62
226.74		UZ	17	51	55.34	27.69	10.77	0.01	0.18	n.d	0.01	0.03	5.39	0.35	99.78	51.43
226.74		UZ	17	52	55.07	27.55	10.69	0.01	0.18	n.d	0.01	0.01	5.35	0.35	99.23	51.43
226.74		UZ	17	53	55.07	27.69	10.73	n.d	0.21	n.d	n.d	0.03	5.47	0.37	99.57	50.92
226.74		UZ	17	54	54.86	27.84	10.72	n.d	0.16	0.02	n.d	0.02	5.45	0.29	99.37	51.23
226.74		UZ	17	55	55.27	27.63	10.59	0.01	0.17	n.d	n.d	0.02	5.45	0.37	99.51	50.70
226.74		UZ	18	56	55.52	27.31	10.56	0.01	0.15	0.02	n.d	0.01	5.46	0.37	99.42	50.58
226.74		UZ	18	57	55.02	27.59	10.60	n.d	0.20	n.d	0.02	0.03	5.39	0.40	99.26	50.89
226.74		UZ	18	58	55.23	27.56	10.55	n.d	0.18	n.d	0.01	0.01	5.41	0.37	99.33	50.77
226.74		UZ	18	59	55.50	27.57	10.48	n.d	0.18	n.d	n.d	0.02	5.43	0.36	99.54	50.55
226.74		UZ	18	60	55.25	27.76	10.78	0.02	0.28	0.02	0.01	0.05	5.29	0.40	99.85	51.75
318.47	TM 1.5	UZ	19	121	56.43	26.90	9.49	0.01	0.16	0.03	n.d	0.05	5.96	0.45	99.48	45.58
318.47		UZ	19	122	56.66	26.80	9.35	0.01	0.16	0.01	n.d	0.03	6.01	0.42	99.44	45.09
318.47		UZ	19	123	56.29	26.85	9.48	n.d	0.17	n.d	n.d	0.14	6.19	0.46	99.57	44.64
318.47		UZ	19	124	55.87	27.39	9.96	0.01	0.15	0.01	n.d	0.04	5.79	0.37	99.59	47.70
318.47		UZ	19	125	55.98	27.30	9.92	n.d	0.16	n.d	n.d	0.02	5.80	0.38	99.55	47.54
318.47		UZ	20	126	55.90	27.32	9.98	0.01	0.13	0.01	n.d	0.03	5.77	0.37	99.52	47.85
318.47		UZ	20	127	56.10	27.01	9.72	0.01	0.15	0.01	n.d	0.04	5.91	0.34	99.29	46.69
318.47		UZ	20	128	56.45	26.99	9.42	n.d	0.15	0.01	0.01	0.04	6.10	0.40	99.58	45.02
318.47		UZ	20	129	56.77	26.69	9.31	n.d	0.17	n.d	n.d	0.06	6.28	0.37	99.66	44.10
318.47		UZ	20	130	55.06	27.71	10.50	0.04	0.24	n.d	n.d	0.03	5.54	0.27	99.40	50.35
318.47		UZ	21	131	55.92	27.22	9.87	0.02	0.18	n.d	n.d	0.04	5.79	0.45	99.49	47.26

Plag																
Depth	Sample	Zone	NO:	Point	SiO ₂	Al ₂ O ₃	CaO	MgO	FeO	MnO	Cr ₂ O ₃	TiO ₂	Na ₂ O	K ₂ O	Total	An%
318.47		UZ	21	132	55.77	27.36	9.99	0.01	0.19	n.d	0.01	0.05	5.74	0.48	99.60	47.68
318.47		UZ	21	133	56.00	27.18	10.06	0.02	0.14	0.01	0.01	0.03	5.85	0.40	99.68	47.64
318.47		UZ	21	134	55.20	27.45	10.19	0.02	0.18	n.d	n.d	0.05	5.71	0.37	99.18	48.62
318.47		UZ	21	135	55.93	27.19	9.89	0.01	0.15	0.01	0.01	0.01	5.81	0.42	99.43	47.32
318.47		UZ	22	136	56.80	26.64	9.24	0.01	0.17	0.01	n.d	0.04	6.09	0.47	99.45	44.37
318.47		UZ	22	137	55.77	27.41	9.94	0.01	0.14	n.d	0.01	0.03	5.75	0.39	99.45	47.77
318.47		UZ	22	138	54.54	28.29	11.29	0.02	0.17	n.d	0.01	n.d	5.13	0.37	99.83	53.73
318.47		UZ	22	139	55.69	27.35	9.97	0.02	0.15	n.d	0.01	0.07	5.81	0.36	99.43	47.69
318.47		UZ	22	140	55.81	27.31	10.04	n.d	0.14	0.03	0.01	n.d	5.71	0.38	99.43	48.22
318.47		UZ	23	141	56.46	26.84	9.56	n.d	0.15	n.d	n.d	0.04	6.08	0.44	99.57	45.33
318.47		UZ	23	142	56.67	26.92	9.49	0.01	0.19	n.d	n.d	0.04	6.07	0.48	99.85	45.10
318.47		UZ	23	143	55.58	27.22	10.13	0.01	0.14	n.d	n.d	0.04	5.72	0.36	99.20	48.44
318.47		UZ	23	144	55.11	26.32	8.90	0.12	2.18	n.d	n.d	0.03	5.81	0.40	98.86	44.77
318.47		UZ	23	145	55.59	27.44	10.10	n.d	0.13	n.d	0.01	0.03	5.62	0.40	99.33	48.69
318.47		UZ	24	146	56.65	26.58	9.14	0.02	0.15	0.01	n.d	0.03	6.25	0.45	99.26	43.56
318.47		UZ	24	147	57.09	26.54	9.13	n.d	0.14	0.02	n.d	0.02	6.21	0.43	99.59	43.72
318.47		UZ	24	148	56.72	26.64	9.34	n.d	0.12	n.d	n.d	0.04	6.20	0.45	99.51	44.27
318.47		UZ	24	149	56.49	26.60	9.30	0.01	0.12	n.d	n.d	n.d	6.25	0.42	99.18	44.05
318.47		UZ	24	150	56.02	27.07	9.79	n.d	0.14	n.d	n.d	0.01	6.04	0.36	99.43	46.29
418.31	TM 1.6	UZ	25	91	56.58	26.64	9.17	0.01	0.16	n.d	n.d	0.01	6.15	0.43	99.16	44.06
418.31		UZ	25	92	56.23	27.02	9.69	0.01	0.16	n.d	n.d	0.02	5.98	0.38	99.49	46.23
418.31		UZ	25	93	57.09	26.70	9.13	0.04	0.34	n.d	0.01	0.04	6.34	0.38	100.07	43.37
418.31		UZ	25	94	55.89	27.36	9.98	0.01	0.15	n.d	0.01	0.04	5.88	0.34	99.67	47.47
418.31		UZ	25	95	56.04	27.10	9.69	0.01	0.17	n.d	0.01	0.06	6.01	0.34	99.43	46.20
418.31		UZ	26	96	56.26	26.84	9.42	0.02	0.20	n.d	n.d	0.06	6.05	0.39	99.23	45.23
418.31		UZ	26	97	56.10	26.94	9.65	n.d	0.22	0.01	n.d	0.05	6.01	0.40	99.37	45.95
418.31		UZ	26	98	56.31	26.81	9.46	0.01	0.16	0.01	n.d	0.05	6.09	0.41	99.32	45.09
418.31		UZ	26	99	56.34	26.74	9.30	0.01	0.19	n.d	0.02	0.02	6.14	0.38	99.13	44.57

Plag																
Depth	Sample	Zone	NO:	Point	SiO ₂	Al ₂ O ₃	CaO	MgO	FeO	MnO	Cr ₂ O ₃	TiO ₂	Na ₂ O	K ₂ O	Total	An%
418.31		UZ	26	100	55.98	26.82	9.52	n.d	0.15	n.d	0.01	0.06	6.08	0.44	99.06	45.23
418.31		UZ	27	101	55.98	27.15	9.76	0.03	0.15	n.d	0.01	0.02	6.00	0.37	99.46	46.35
418.31		UZ	27	102	56.44	26.85	9.55	0.01	0.15	0.02	0.01	0.05	6.08	0.38	99.55	45.47
418.31		UZ	27	103	56.35	26.81	9.41	0.01	0.13	0.02	0.01	0.03	6.03	0.40	99.19	45.25
418.31		UZ	27	104	56.26	26.88	9.38	n.d	0.23	n.d	n.d	0.03	6.13	0.39	99.32	44.82
418.31		UZ	27	105	56.34	26.85	9.54	0.01	0.14	0.01	n.d	0.04	6.01	0.42	99.36	45.59
418.31		UZ	28	106	56.57	26.58	9.29	0.01	0.18	0.02	n.d	n.d	6.16	0.52	99.32	44.13
418.31		UZ	28	107	55.72	26.95	9.59	n.d	0.15	n.d	0.01	0.05	5.95	0.38	98.80	46.09
418.31		UZ	28	108	55.93	26.89	9.73	n.d	0.15	0.01	0.01	0.05	5.92	0.48	99.17	46.30
418.31		UZ	28	109	56.06	26.99	9.50	0.03	0.21	0.03	0.02	0.02	5.96	0.43	99.24	45.66
418.31		UZ	28	110	56.25	26.67	9.55	n.d	0.18	n.d	0.02	0.05	5.98	0.47	99.19	45.62
418.31		UZ	29	111	56.35	26.85	9.41	0.02	0.14	n.d	0.01	n.d	6.03	0.36	99.18	45.35
418.31		UZ	29	112	56.08	26.87	9.54	n.d	0.18	0.01	n.d	0.04	6.10	0.40	99.21	45.32
418.31		UZ	29	113	55.74	27.14	9.86	0.02	0.15	n.d	n.d	0.04	5.91	0.36	99.20	46.98
418.31		UZ	29	114	55.71	27.12	9.78	0.01	0.20	n.d	n.d	0.04	5.94	0.37	99.15	46.66
418.31		UZ	29	115	55.95	26.85	9.66	0.02	0.13	n.d	0.02	0.03	6.01	0.36	99.04	46.08
418.31		UZ	30	116	56.07	27.04	9.77	n.d	0.18	0.02	0.03	0.02	5.88	0.44	99.46	46.65
418.31		UZ	30	117	56.16	26.92	9.48	0.02	0.17	n.d	0.01	0.05	5.99	0.48	99.28	45.38
418.31		UZ	30	118	53.66	25.33	10.90	0.15	0.21	n.d	0.01	0.03	5.88	0.44	96.61	49.39
418.31		UZ	30	119	57.02	26.33	9.04	0.02	0.15	n.d	n.d	0.04	6.23	0.50	99.33	43.24
418.31		UZ	30	120	56.14	27.00	9.64	0.02	0.18	0.02	n.d	0.04	6.04	0.46	99.54	45.63
524.44	TM 1.7	UZ	31	61	55.65	27.39	10.08	0.01	0.20	n.d	n.d	0.01	5.78	0.38	99.50	48.01
524.44		UZ	31	62	55.73	27.43	10.19	0.02	0.16	n.d	n.d	0.06	5.68	0.44	99.70	48.54
524.44		UZ	31	63	54.93	27.76	10.49	0.01	0.18	0.01	n.d	n.d	5.57	0.37	99.33	49.93
524.44		UZ	31	64	55.56	27.47	10.24	0.01	0.15	n.d	0.01	n.d	5.63	0.38	99.45	49.06
524.44		UZ	31	65	55.16	27.93	10.38	0.01	0.15	n.d	n.d	0.01	5.50	0.36	99.50	50.01
524.44	UZ	32	66	55.75	27.93	10.25	n.d	0.19	n.d	n.d	0.02	5.65	0.32	100.11	49.14	
524.44		UZ	32	67	54.91	27.80	10.50	n.d	0.20	0.01	n.d	0.02	5.52	0.40	99.37	50.08

Plag																
Depth	Sample	Zone	NO:	Point	SiO ₂	Al ₂ O ₃	CaO	MgO	FeO	MnO	Cr ₂ O ₃	TiO ₂	Na ₂ O	K ₂ O	Total	An%
524.44		UZ	32	68	55.58	27.42	10.18	0.02	0.18	n.d	0.02	0.01	5.66	0.42	99.49	48.66
524.44		UZ	32	69	54.93	27.78	10.66	n.d	0.19	0.02	0.02	0.04	5.40	0.37	99.40	51.09
524.44		UZ	32	70	55.31	27.43	10.12	n.d	0.15	n.d	0.01	0.03	5.69	0.42	99.15	48.38
524.44		UZ	33	71	55.64	27.34	10.02	0.02	0.25	n.d	n.d	0.05	5.77	0.41	99.50	47.82
524.44		UZ	33	72	54.70	28.11	10.82	n.d	0.17	0.02	n.d	n.d	5.48	0.27	99.58	51.37
524.44		UZ	33	73	55.26	27.57	10.26	n.d	0.16	n.d	0.01	0.02	5.62	0.40	99.32	49.09
524.44		UZ	33	74	55.82	27.33	10.01	n.d	0.20	n.d	0.02	0.03	5.67	0.41	99.50	48.20
524.44		UZ	33	75	54.59	28.11	11.09	0.01	0.20	n.d	n.d	0.01	5.30	0.27	99.57	52.80
524.44		UZ	34	76	55.11	27.68	10.41	0.02	0.17	0.02	n.d	0.05	5.47	0.44	99.37	49.95
524.44		UZ	34	77	54.90	27.49	10.50	n.d	0.20	0.01	0.01	0.01	5.49	0.38	98.99	50.27
524.44		UZ	34	78	55.40	27.60	10.39	0.01	0.17	n.d	0.01	0.05	5.44	0.42	99.49	50.09
524.44		UZ	34	79	55.01	27.96	10.52	0.01	0.16	0.02	n.d	n.d	5.37	0.40	99.43	50.81
524.44		UZ	34	80	55.09	27.86	10.52	n.d	0.17	n.d	0.01	n.d	5.44	0.37	99.47	50.57
524.44		UZ	35	81	55.28	27.81	10.41	0.02	0.18	n.d	0.01	n.d	5.57	0.41	99.68	49.60
524.44		UZ	35	82	53.48	26.25	9.30	0.31	2.21	0.02	0.01	n.d	5.36	0.35	97.28	47.89
524.44		UZ	35	83	55.22	27.65	10.33	n.d	0.20	0.01	n.d	0.02	5.59	0.40	99.41	49.37
524.44		UZ	35	84	55.51	27.49	10.05	n.d	0.13	n.d	n.d	n.d	5.74	0.43	99.35	47.97
524.44		UZ	35	85	55.03	27.84	10.54	0.01	0.19	0.01	0.01	0.02	5.34	0.37	99.36	51.05
524.44		UZ	36	86	54.96	27.73	10.43	0.01	0.17	0.01	0.02	0.02	5.47	0.37	99.20	50.22
524.44		UZ	36	87	55.85	27.16	9.70	0.01	0.12	0.02	n.d	0.03	5.79	0.41	99.08	46.93
524.44		UZ	36	88	54.98	27.80	10.66	0.01	0.17	n.d	n.d	0.02	5.45	0.39	99.49	50.82
524.44		UZ	36	89	55.36	27.61	10.34	n.d	0.20	n.d	0.01	0.02	5.67	0.41	99.62	49.02
524.44		UZ	36	90	54.53	27.86	10.80	0.03	0.16	0.02	n.d	0.04	5.36	0.36	99.17	51.61
603.78	TM 1.8	UZ	38	160	54.58	28.22	11.03	0.03	0.17	0.01	0.01	0.04	5.30	0.26	99.65	52.69
603.78		UZ	38	161	54.50	28.14	10.83	0.04	0.26	0.01	0.01	0.01	5.48	0.24	99.53	51.51
603.78		UZ	38	162	53.54	28.81	11.58	0.02	0.13	n.d	n.d	0.06	5.01	0.24	99.39	55.35
603.78		UZ	39	163	54.31	28.30	11.18	0.01	0.13	0.03	n.d	0.06	5.19	0.26	99.46	53.54
603.78		UZ	39	164	54.02	28.46	11.23	0.02	0.17	n.d	n.d	0.05	5.12	0.29	99.36	53.88

Plag																
Depth	Sample	Zone	NO:	Point	SiO ₂	Al ₂ O ₃	CaO	MgO	FeO	MnO	Cr ₂ O ₃	TiO ₂	Na ₂ O	K ₂ O	Total	An%
603.78		UZ	39	165	53.53	28.63	11.77	0.01	0.16	n.d	n.d	0.04	4.94	0.28	99.37	55.93
603.78		UZ	42	166	53.63	28.63	11.62	n.d	0.16	n.d	0.02	0.05	5.08	0.23	99.42	55.11
603.78		UZ	42	167	53.86	28.55	11.35	n.d	0.13	0.01	0.02	0.02	5.24	0.21	99.39	53.86
603.78		UZ	42	168	53.76	28.74	11.58	0.01	0.14	0.03	n.d	0.06	4.84	0.21	99.37	56.25
711.43	TM 1.9	UZ	43	169	54.26	28.06	11.00	0.02	0.16	0.01	0.01	0.04	5.34	0.24	99.14	52.50
711.43		UZ	43	170	54.85	27.94	10.96	0.01	0.19	0.01	n.d	n.d	5.31	0.34	99.60	52.25
711.43		UZ	43	171	53.71	28.47	11.42	0.02	0.21	n.d	n.d	0.02	5.00	0.27	99.14	54.91
711.43		UZ	43	172	53.96	28.15	11.18	0.02	0.21	0.02	n.d	0.03	5.21	0.23	99.01	53.54
711.43		UZ	45	173	53.94	28.32	11.39	0.02	0.21	n.d	0.01	0.02	4.98	0.27	99.17	54.97
711.43		UZ	45	174	53.82	28.56	11.68	0.02	0.21	n.d	n.d	0.01	4.95	0.23	99.49	55.86
711.43		UZ	45	175	53.44	28.56	11.76	0.01	0.24	n.d	0.02	0.03	4.84	0.25	99.14	56.48
711.43		UZ	48	176	53.95	28.62	11.61	0.03	0.21	n.d	0.02	n.d	4.85	0.27	99.57	56.04
711.43		UZ	48	177	53.79	28.69	11.71	0.01	0.15	n.d	n.d	0.01	4.82	0.25	99.43	56.46
711.43		UZ	48	178	53.72	28.76	11.81	0.01	0.21	n.d	0.02	0.04	4.84	0.29	99.70	56.46
812.53	TM 1.10	UZ	50	179	53.68	28.95	11.85	0.01	0.23	n.d	n.d	0.02	4.86	0.22	99.83	56.69
			50	180	53.64	28.80	11.70	0.01	0.19	0.01	n.d	0.01	4.82	0.23	99.40	56.53
			50	181	53.65	28.72	11.64	0.01	0.15	0.01	0.01	0.02	4.98	0.20	99.38	55.75
			51	182	54.01	28.58	11.62	n.d	0.18	n.d	0.02	n.d	5.08	0.15	99.65	55.34
			51	183	53.79	28.48	11.46	0.01	0.19	0.01	n.d	0.01	4.97	0.25	99.18	55.21
			51	184	53.64	28.82	11.77	n.d	0.16	n.d	0.01	0.02	4.79	0.17	99.39	57.02
			53	185	53.88	28.70	11.63	0.01	0.10	n.d	n.d	n.d	5.05	0.21	99.58	55.34
			53	186	53.65	28.68	11.75	0.03	0.20	0.03	n.d	0.03	4.88	0.22	99.47	56.39
			53	187	54.01	28.49	11.30	0.01	0.21	n.d	n.d	0.07	5.02	0.22	99.32	54.74
911.78	TM 1.11	UZ	56	188	54.19	28.26	11.16	0.01	0.16	n.d	n.d	0.02	5.32	0.26	99.38	52.90
			56	189	54.07	28.33	11.34	0.01	0.13	0.01	n.d	0.04	5.19	0.28	99.41	53.83
			56	190	53.75	28.30	11.26	0.02	0.15	n.d	n.d	0.04	5.22	0.29	99.02	53.49

Depth	Sample	Zone	Plag													
			NO:	Point	SiO ₂	Al ₂ O ₃	CaO	MgO	FeO	MnO	Cr ₂ O ₃	TiO ₂	Na ₂ O	K ₂ O	Total	An%
911.78		UZ	58	191	54.02	28.28	11.06	0.01	0.18	0.01	n.d	0.02	5.25	0.16	99.00	53.30
911.78		UZ	58	192	54.32	28.38	11.09	0.01	0.15	n.d	n.d	0.06	5.44	0.15	99.62	52.52
911.78		UZ	58	193	53.82	28.32	11.37	0.1	0.25	n.d	n.d	0.02	5.16	0.14	99.17	54.45
911.78		UZ	59	194	53.94	28.45	11.38	0.02	0.16	n.d	n.d	0.06	5.20	0.26	99.47	53.92
911.78		UZ	59	195	54.18	28.30	11.08	0.02	0.18	0.01	0.02	0.04	5.27	0.30	99.40	52.83
911.78		UZ	59	196	54.36	28.06	11.05	n.d	0.14	n.d	n.d	0.05	5.29	0.28	99.23	52.70
911.78		UZ	59	197	53.89	28.20	11.16	0.02	0.16	0.01	n.d	0.04	5.21	0.25	98.95	53.41
911.78		UZ	59	198	54.48	28.07	10.97	n.d	0.16	n.d	0.01	0.04	5.30	0.30	99.33	52.44
		TM														
1005.31	1.12	UZ	61	199	53.95	28.48	11.52	0.01	0.22	0.01	0.02	0.05	4.92	0.36	99.55	55.24
1005.31		UZ	61	200	53.73	28.59	11.67	0.03	0.21	n.d	n.d	0.05	4.85	0.38	99.51	55.84
1005.31		UZ	61	201	53.89	28.46	11.35	0.02	0.24	0.01	n.d	0.05	5.02	0.36	99.39	54.41
1005.31		UZ	61	202	53.83	28.40	11.51	0.01	0.23	0.02	n.d	0.02	4.99	0.36	99.37	54.90
1005.31		UZ	61	203	53.78	28.41	11.47	0.01	0.25	n.d	0.03	0.07	4.93	0.39	99.34	55.02
1005.31		UZ	64	204	53.86	28.64	11.51	0.02	0.22	n.d	0.01	0.04	4.81	0.34	99.46	55.82
1005.31		UZ	64	205	53.90	28.49	11.58	n.d	0.21	n.d	0.01	0.01	4.93	0.35	99.48	55.36
1005.31		UZ	64	206	53.55	28.74	11.77	0.01	0.24	n.d	0.02	0.03	4.73	0.36	99.44	56.71
1005.31		UZ	65	207	53.64	28.66	11.64	0.01	0.22	n.d	n.d	n.d	4.76	0.33	99.27	56.38
1005.31		UZ	65	208	53.51	28.58	11.66	n.d	0.23	n.d	0.01	0.05	4.84	0.34	99.23	56.02
1005.31		UZ	65	209	53.65	28.59	11.65	0.02	0.23	n.d	n.d	0.02	4.79	0.35	99.30	56.18
		TM														
1104.46	1.13	UZ	68	210	52.26	29.71	12.65	0.01	0.16	n.d	n.d	0.01	4.46	0.10	99.37	60.68
1104.46		UZ	68	211	52.63	29.30	12.43	0.03	0.17	n.d	n.d	0.02	4.65	0.12	99.34	59.22
1104.46		UZ	68	212	51.89	29.60	12.67	0.02	0.16	n.d	n.d	0.03	4.32	0.13	98.82	61.37
1104.46		UZ	69	213	51.85	29.67	12.79	0.03	0.17	n.d	0.02	n.d	4.36	0.11	99.00	61.47
1104.46		UZ	69	214	52.69	29.27	12.22	0.01	0.16	n.d	n.d	0.02	4.69	0.14	99.20	58.53
1104.46		UZ	69	215	53.18	29.17	11.93	0.01	0.14	n.d	n.d	0.03	4.85	0.12	99.42	57.19
1104.46		UZ	72	216	49.11	31.33	15.08	0.01	0.12	n.d	0.01	n.d	3.04	0.08	98.78	72.97

Plag																
Depth	Sample	Zone	NO:	Point	SiO ₂	Al ₂ O ₃	CaO	MgO	FeO	MnO	Cr ₂ O ₃	TiO ₂	Na ₂ O	K ₂ O	Total	An%
1104.46		UZ	72	217	52.07	29.66	12.77	0.02	0.17	0.02	n.d	0.04	4.40	0.13	99.26	61.13
1104.46		UZ	72	218	52.48	29.50	12.50	0.01	0.15	n.d	0.01	0.02	4.52	0.14	99.32	59.97
		TM														
1201.54	1.13.1	UMZ	73	219	52.69	29.14	12.51	0.02	0.25	n.d	n.d	0.03	4.43	0.30	99.37	59.89
1201.54		UMZ	73	220	51.64	29.46	12.95	0.02	0.26	n.d	n.d	0.02	4.16	0.27	98.80	62.25
1201.54		UMZ	73	221	52.55	29.27	12.66	0.02	0.27	0.02	0.01	0.06	4.37	0.30	99.53	60.49
1201.54		UMZ	73	222	52.48	29.22	12.44	0.02	0.27	n.d	n.d	0.04	4.51	0.30	99.28	59.34
1201.54		UMZ	75	223	52.40	29.38	12.54	0.02	0.28	0.01	n.d	0.05	4.45	0.23	99.36	60.11
1201.54		UMZ	75	224	52.51	29.36	12.64	0.01	0.30	0.01	n.d	0.04	4.38	0.26	99.52	60.53
1201.54		UMZ	75	225	52.52	29.26	12.59	0.02	0.28	n.d	n.d	0.05	4.35	0.28	99.35	60.53
1201.54		UMZ	78	226	52.75	29.42	12.43	0.01	0.25	0.01	0.01	0.04	4.41	0.30	99.64	59.83
1201.54		UMZ	78	227	52.40	29.45	12.64	0.02	0.29	0.01	n.d	0.04	4.36	0.25	99.46	60.69
1201.54		UMZ	78	228	49.70	27.54	11.12	1.79	3.80	0.04	n.d	0.01	3.86	0.23	98.07	60.51
		TM														
1299.49	1.13.2	UMZ	79	229	49.79	31.18	14.82	0.03	0.27	n.d	0.02	n.d	3.12	0.17	99.39	71.72
1299.49		UMZ	79	230	49.47	31.45	14.88	0.01	0.24	0.01	n.d	0.03	3.11	0.13	99.32	71.99
1299.49		UMZ	79	231	50.57	30.74	14.20	0.02	0.30	0.01	n.d	0.01	3.52	0.22	99.58	68.17
1299.49		UMZ	82	232	49.73	31.17	14.64	0.01	0.27	n.d	n.d	0.06	3.15	0.16	99.18	71.32
1299.49		UMZ	82	233	49.99	31.14	14.83	0.01	0.28	n.d	n.d	0.06	3.26	0.15	99.72	70.92
1299.49		UMZ	82	234	49.71	31.22	14.77	0.01	0.31	n.d	n.d	0.01	3.14	0.16	99.34	71.54
1299.49		UMZ	84	235	49.41	31.32	15.21	0.01	0.29	n.d	n.d	0.01	3.09	0.17	99.51	72.40
1299.49		UMZ	84	236	50.54	30.78	14.14	0.01	0.28	n.d	n.d	0.01	3.56	0.20	99.53	67.93
1299.49		UMZ	84	237	50.84	30.53	13.93	0.02	0.22	0.01	n.d	0.04	3.70	0.16	99.47	66.92
		TM														
1349.35	1.13.3	UMZ	295	238	51.80	29.74	13.04	0.02	0.35	0.01	n.d	n.d	4.21	0.20	99.36	62.42
1349.35		UMZ	295	239	50.92	30.23	13.73	0.02	0.37	n.d	n.d	0.05	3.71	0.20	99.24	66.38
1349.35		UMZ	295	240	51.16	30.26	13.75	0.02	0.36	n.d	n.d	0.01	3.74	0.23	99.54	66.16
1349.35		UMZ	297	241	51.38	30.29	14.03	0.03	0.40	n.d	0.02	0.03	3.65	0.20	100.03	67.22

Plag																
Depth	Sample	Zone	NO:	Point	SiO ₂	Al ₂ O ₃	CaO	MgO	FeO	MnO	Cr ₂ O ₃	TiO ₂	Na ₂ O	K ₂ O	Total	An%
1349.35		UMZ	297	242	51.17	30.31	13.77	0.01	0.34	0.01	n.d	0.04	3.70	0.22	99.58	66.44
1349.35		UMZ	297	243	52.08	29.71	13.22	0.01	0.40	n.d	0.01	0.07	4.08	0.26	99.83	63.21
1349.35		UMZ	298	244	51.48	30.38	13.65	0.01	0.31	n.d	n.d	0.03	3.83	0.18	99.87	65.64
1349.35		UMZ	298	245	51.95	29.87	13.19	0.02	0.31	n.d	0.02	0.05	4.07	0.29	99.75	63.09
1349.35		UMZ	298	246	51.39	30.13	13.65	0.01	0.30	n.d	n.d	0.02	3.80	0.24	99.57	65.61
TM																
1519.05	1.14	UMZ	85	247	50.42	30.90	14.46	0.01	0.35	n.d	n.d	0.02	3.47	0.15	99.77	69.12
1519.05		UMZ	85	248	51.23	30.26	13.88	0.02	0.29	n.d	n.d	0.01	3.89	0.17	99.75	65.70
1519.05		UMZ	85	249	50.27	31.19	14.70	0.01	0.38	0.02	n.d	n.d	3.20	0.17	99.94	71.05
1519.05		UMZ	89	250	51.02	30.53	14.04	0.02	0.35	0.02	0.02	0.04	3.63	0.20	99.88	67.35
1519.05		UMZ	89	251	51.55	30.33	13.57	n.d	0.36	0.03	n.d	0.02	3.88	0.18	99.92	65.23
1519.05		UMZ	89	252	50.97	30.74	14.06	0.01	0.41	n.d	n.d	0.06	3.50	0.17	99.93	68.25
1519.05		UMZ	90	253	50.67	30.55	14.11	0.08	0.44	n.d	0.03	0.01	3.44	0.16	99.49	68.74
1519.05		UMZ	90	254	51.28	30.17	13.72	0.02	0.31	n.d	0.01	0.02	3.85	0.15	99.54	65.76
1519.05		UMZ	90	255	50.50	30.85	14.29	0.02	0.35	n.d	n.d	0.04	3.56	0.18	99.78	68.24
TM																
1616.47	1.15	UMZ	91	256	50.43	30.73	14.13	0.01	0.32	n.d	n.d	0.04	3.54	0.17	99.37	68.14
1616.47		UMZ	91	257	49.24	31.54	15.29	0.01	0.31	0.01	0.01	0.01	2.86	0.17	99.45	74.00
1616.47		UMZ	91	258	48.73	31.68	15.63	0.03	0.33	0.02	n.d	0.02	2.81	0.16	99.42	74.78
1616.47		UMZ	93	259	49.09	31.55	15.17	0.02	0.32	0.01	n.d	0.02	2.81	0.17	99.15	74.17
1616.47		UMZ	93	260	49.47	31.38	15.28	0.02	0.35	n.d	0.01	0.03	2.96	0.16	99.66	73.35
1616.47		UMZ	93	261	49.21	31.55	15.07	0.03	0.33	n.d	n.d	0.02	2.98	0.18	99.38	72.88
1616.47		UMZ	96	262	50.64	30.51	13.86	0.02	0.36	n.d	n.d	0.03	3.56	0.21	99.18	67.46
1616.47		UMZ	96	263	50.11	30.97	14.47	0.01	0.28	0.01	0.01	n.d	3.27	0.14	99.26	70.38
1616.47		UMZ	96	264	49.08	31.47	15.31	0.02	0.32	n.d	0.01	0.02	2.91	0.16	99.31	73.70
1616.47		UMZ	96	265	49.02	31.57	15.24	0.02	0.35	n.d	0.02	0.04	2.85	0.16	99.26	74.02
TM																
1695.81	1.16	UMZ	97	266	49.98	31.16	14.74	0.02	0.28	0.01	0.01	0.01	3.13	0.29	99.64	71.03

Plag																
Depth	Sample	Zone	NO:	Point	SiO ₂	Al ₂ O ₃	CaO	MgO	FeO	MnO	Cr ₂ O ₃	TiO ₂	Na ₂ O	K ₂ O	Total	An%
1695.81		UMZ	97	267	50.24	30.78	14.30	0.01	0.31	n.d	n.d	0.05	3.29	0.25	99.23	69.56
1695.81		UMZ	97	268	49.26	31.49	15.14	0.01	0.28	n.d	0.01	0.02	2.96	0.23	99.40	72.89
1695.81		UMZ	102	272	49.58	31.30	15.04	0.02	0.35	0.02	n.d	0.05	2.99	0.23	99.59	72.60
1695.81		UMZ	102	273	50.14	30.80	14.26	0.02	0.24	n.d	n.d	0.03	3.40	0.25	99.14	68.82
1695.81		UMZ	102	274	51.13	30.02	13.47	n.d	0.25	n.d	n.d	0.04	3.34	1.12	99.37	64.60
		TM														
1757.02	1.16.1	UMZ	311	275	51.65	29.94	13.27	0.01	0.23	0.01	0.01	0.03	3.88	0.27	99.30	64.36
1757.02		UMZ	311	276	51.19	30.13	13.42	0.03	0.24	n.d	n.d	0.02	3.75	0.28	99.06	65.33
1757.02		UMZ	311	277	51.49	30.57	13.70	0.01	0.25	n.d	n.d	0.04	3.11	0.24	99.42	69.86
1757.02		UMZ	309	278	52.17	29.71	12.91	0.01	0.24	n.d	n.d	0.05	4.13	0.26	99.48	62.38
1757.02		UMZ	309	279	52.12	29.73	12.98	0.03	0.25	0.02	0.01	0.03	4.13	0.29	99.58	62.42
1757.02		UMZ	309	280	51.95	29.80	12.89	0.01	0.22	0.01	n.d	0.07	4.15	0.29	99.41	62.12
1757.02		UMZ	309	281	51.90	30.16	13.49	0.03	0.22	n.d	n.d	0.03	3.90	0.24	99.97	64.77
1757.02		UMZ	307	282	51.99	29.29	12.78	0.02	0.21	n.d	n.d	0.02	4.21	0.37	98.89	61.35
1757.02		UMZ	307	283	51.30	30.25	13.55	0.03	0.24	0.03	n.d	0.06	3.78	0.29	99.53	65.33
1757.02		UMZ	307	284	52.22	29.60	12.89	0.01	0.23	n.d	0.01	0.02	4.12	0.35	99.47	62.08
		TM														
1782.05	1.17	LMZ	103	285	49.42	31.59	15.17	0.02	0.26	n.d	0.01	0.03	2.87	0.18	99.55	73.73
1782.05		LMZ	103	286	49.25	31.53	15.08	0.03	0.26	n.d	0.01	0.05	3.01	0.19	99.40	72.66
1782.05		LMZ	103	287	49.15	31.70	15.38	0.03	0.26	0.03	n.d	0.03	2.82	0.17	99.57	74.36
1782.05		LMZ	105	288	49.49	31.29	15.03	0.05	0.31	n.d	n.d	0.03	3.04	0.22	99.46	72.32
1782.05		LMZ	105	289	49.30	31.79	15.41	0.03	0.30	0.01	n.d	0.04	2.78	0.16	99.81	74.67
1782.05		LMZ	105	290	49.08	31.34	15.22	0.02	0.31	n.d	n.d	0.05	3.07	0.21	99.30	72.41
1782.05		LMZ	107	291	50.59	30.80	14.16	0.03	0.32	n.d	n.d	0.01	3.43	0.25	99.60	68.52
1782.05		LMZ	107	292	49.26	31.51	15.23	0.03	0.28	n.d	n.d	0.02	2.86	0.18	99.36	73.88
1782.05		LMZ	107	293	50.97	30.47	13.97	0.02	0.29	n.d	0.04	0.05	3.58	0.17	99.56	67.64
		TM														
1879.26	1.18	LMZ	111	294	52.56	29.27	12.66	0.03	0.31	n.d	n.d	0.01	4.30	0.28	99.43	60.92

Plag																
Depth	Sample	Zone	NO:	Point	SiO ₂	Al ₂ O ₃	CaO	MgO	FeO	MnO	Cr ₂ O ₃	TiO ₂	Na ₂ O	K ₂ O	Total	An%
1879.26		LMZ	111	295	53.61	28.59	11.70	0.01	0.25	n.d	n.d	0.05	4.80	0.36	99.37	56.21
1879.26		LMZ	111	296	53.17	28.82	12.01	0.01	0.31	n.d	n.d	0.01	4.61	0.32	99.25	57.92
1879.26		LMZ	112	297	52.37	29.69	12.95	0.01	0.50	n.d	n.d	0.06	4.27	0.16	100.03	62.05
1879.26		LMZ	112	298	53.13	29.21	12.38	0.02	0.32	0.01	n.d	0.04	4.52	0.23	99.87	59.45
1879.26		LMZ	112	299	52.49	29.52	12.88	0.01	0.29	n.d	n.d	0.04	4.27	0.29	99.78	61.47
1879.26		LMZ	114	300	52.91	29.44	12.38	n.d	0.28	0.02	0.01	0.05	4.45	0.25	99.78	59.71
1879.26		LMZ	114	301	52.80	29.42	12.68	0.01	0.29	n.d	n.d	0.04	4.33	0.33	99.90	60.63
1879.26		LMZ	114	302	52.51	29.48	12.75	0.02	0.28	0.01	0.01	0.03	4.27	0.31	99.67	61.16
		TM														
1978.02	1.19	LMZ	115	303	52.77	29.19	12.46	0.01	0.27	0.01	0.01	0.01	4.41	0.27	99.41	59.99
1978.02		LMZ	115	304	52.69	29.46	12.54	0.01	0.28	0.01	n.d	0.05	4.35	0.27	99.66	60.47
1978.02		LMZ	115	305	52.83	28.98	12.59	0.03	0.29	n.d	0.01	0.01	4.36	0.28	99.38	60.50
1978.02		LMZ	117	306	52.39	29.32	12.73	n.d	0.28	n.d	n.d	n.d	4.33	0.27	99.33	60.92
1978.02		LMZ	117	307	52.42	29.28	12.63	0.02	0.32	0.02	n.d	0.01	4.24	0.27	99.22	61.23
1978.02		LMZ	117	308	52.55	29.11	12.45	0.01	0.30	0.01	n.d	0.02	4.36	0.29	99.11	60.20
1978.02		LMZ	120	309	52.34	29.58	12.79	n.d	0.26	n.d	0.02	0.02	4.25	0.28	99.54	61.43
1978.02		LMZ	120	310	53.47	28.77	11.98	0.03	0.25	0.01	n.d	0.02	4.61	0.29	99.44	57.95
1978.02		LMZ	120	311	52.90	29.07	12.16	0.01	0.37	0.01	n.d	0.03	4.53	0.31	99.41	58.66
		TM														
2076.38	1.20	LMZ	122	312	53.05	28.97	12.27	0.01	0.28	0.01	n.d	0.02	4.60	0.31	99.53	58.53
2076.38		LMZ	122	313	52.89	29.31	12.35	0.02	0.28	n.d	n.d	n.d	4.53	0.30	99.68	59.07
2076.38		LMZ	122	314	52.27	29.24	12.68	0.01	0.34	0.01	0.01	0.03	4.35	0.29	99.25	60.67
2076.38		LMZ	125	315	52.99	29.22	12.54	0.01	0.28	n.d	n.d	n.d	4.41	0.26	99.72	60.17
2076.38		LMZ	125	316	52.84	29.22	12.45	0.02	0.27	0.03	n.d	0.05	4.48	0.30	99.67	59.52
2076.38		LMZ	125	317	52.25	29.44	12.93	0.02	0.29	0.01	0.01	n.d	4.22	0.25	99.43	61.96
		TM														
2274.98	1.22	LMZ	136	318	52.28	29.63	12.84	0.03	0.33	0.01	0.01	0.06	4.14	0.30	99.62	62.06
2274.98		LMZ	136	319	52.34	29.90	13.02	0.02	0.32	n.d	n.d	0.05	4.09	0.29	100.03	62.69

Plag																
Depth	Sample	Zone	NO:	Point	SiO ₂	Al ₂ O ₃	CaO	MgO	FeO	MnO	Cr ₂ O ₃	TiO ₂	Na ₂ O	K ₂ O	Total	An%
2274.98		LMZ	136	320	52.25	29.39	12.81	0.02	0.29	n.d	n.d	0.01	4.23	0.27	99.28	61.63
2274.98		LMZ	138	321	51.92	29.63	13.11	0.01	0.29	0.02	n.d	0.05	3.98	0.30	99.30	63.43
2274.98		LMZ	138	322	52.18	29.47	12.69	0.02	0.28	0.01	0.02	0.06	4.21	0.31	99.25	61.38
2274.98		LMZ	138	323	52.28	29.41	12.77	0.03	0.30	n.d	n.d	0.01	4.20	0.31	99.31	61.56
		TM														
2448.40	1.24	LMZ	145	324	51.95	29.60	12.88	0.03	0.33	n.d	n.d	0.03	4.19	0.31	99.31	61.83
2448.40		LMZ	145	325	50.96	27.90	11.85	1.47	1.61	0.01	n.d	0.06	4.05	0.29	98.20	60.70
2448.40		LMZ	145	326	51.96	29.89	13.03	0.02	0.27	0.03	n.d	0.02	4.18	0.26	99.65	62.33
2448.40		LMZ	149	327	50.68	28.11	11.68	1.17	1.97	0.02	n.d	0.02	3.92	0.30	97.87	61.07
2448.40		LMZ	149	328	51.86	29.66	12.91	0.01	0.33	0.01	0.01	0.03	4.15	0.30	99.28	62.12
2448.40		LMZ	149	329	51.78	29.87	13.06	0.02	0.30	0.01	n.d	0.04	4.04	0.26	99.39	63.13
2448.40		LMZ	149	330	51.92	29.73	13.13	0.03	0.29	n.d	n.d	0.03	4.13	0.27	99.52	62.74
		TM														
2639.06	1.26	LMZ	158	331	51.41	30.08	13.47	0.01	0.31	0.02	n.d	0.04	3.83	0.25	99.40	65.06
2639.06		LMZ	158	332	52.26	29.26	12.72	0.02	0.32	0.02	0.01	0.05	4.28	0.33	99.27	60.97
2639.06		LMZ	158	333	52.40	29.39	12.57	0.01	0.29	n.d	n.d	0.08	4.22	0.28	99.25	61.18
2639.06		LMZ	161	334	52.24	29.70	12.95	0.02	0.26	n.d	n.d	0.02	4.15	0.26	99.59	62.32
2639.06		LMZ	161	335	52.13	29.66	12.77	0.01	0.27	0.01	n.d	0.02	4.25	0.26	99.39	61.46
2639.06		LMZ	161	336	51.59	30.03	13.24	0.02	0.25	n.d	n.d	0.04	4.06	0.24	99.48	63.45
		TM														
2841.74	1.28	LMZ	171	337	50.57	30.61	14.04	0.02	0.26	0.01	n.d	0.04	3.64	0.19	99.37	67.35
2841.74		LMZ	171	338	50.86	30.48	13.98	0.03	0.30	0.01	n.d	0.01	3.58	0.26	99.51	67.29
2841.74		LMZ	171	339	50.61	30.44	13.91	0.02	0.26	n.d	0.01	0.03	3.60	0.22	99.11	67.25
2841.74		LMZ	174	340	50.84	30.57	14.01	0.02	0.31	n.d	n.d	n.d	3.61	0.23	99.59	67.33
2841.74		LMZ	174	341	50.96	30.26	13.55	0.02	0.30	0.01	n.d	0.03	3.72	0.27	99.11	65.76
2841.74		LMZ	174	342	50.40	30.68	14.05	0.01	0.29	n.d	0.03	0.02	3.59	0.22	99.29	67.54
		TM														
3035.77	1.30	LMZ	183	343	50.51	30.99	14.30	0.02	0.26	0.01	n.d	0.02	3.42	0.23	99.74	68.88
3035.77		LMZ	183	344	51.38	30.04	13.18	0.01	0.30	0.01	n.d	0.05	3.84	0.29	99.10	64.35

Plag																
Depth	Sample	Zone	NO:	Point	SiO ₂	Al ₂ O ₃	CaO	MgO	FeO	MnO	Cr ₂ O ₃	TiO ₂	Na ₂ O	K ₂ O	Total	An%
3035.77		LMZ	183	345	49.74	31.06	14.63	0.02	0.27	0.02	0.02	0.01	3.14	0.19	99.11	71.23
3035.77		LMZ	185	346	50.21	31.11	14.55	0.01	0.32	0.01	n.d	0.02	3.25	0.23	99.72	70.31
3035.77		LMZ	185	347	49.88	31.09	14.70	0.01	0.26	0.01	n.d	0.03	3.27	0.21	99.47	67.85
3035.77		LMZ	185	348	49.93	30.93	14.57	0.02	0.28	n.d	n.d	0.01	3.30	0.21	99.27	70.10
		TM														
3230.89	1.32	LMZ	196	349	49.59	31.29	15.02	0.02	0.33	n.d	n.d	n.d	3.09	0.14	99.49	72.26
3230.89		LMZ	196	350	51.03	30.45	13.85	0.02	0.24	n.d	0.01	0.03	3.67	0.21	99.50	66.79
3230.89		LMZ	196	351	49.89	31.10	14.68	0.02	0.27	n.d	0.02	0.02	3.25	0.18	99.44	70.68
3230.89		LMZ	197	352	51.18	30.09	13.58	0.02	0.27	0.01	n.d	0.03	3.84	0.31	99.34	64.97
3230.89		LMZ	197	353	51.69	30.08	13.41	0.01	0.31	n.d	n.d	0.03	3.94	0.22	99.70	64.46
3230.89		LMZ	197	354	51.36	30.07	13.56	0.03	0.32	0.01	0.01	0.02	3.89	0.29	99.55	64.72
		TM														
3427.93	1.34	LMZ	206	355	49.98	31.12	14.74	0.01	0.26	n.d	n.d	0.05	3.20	0.21	99.57	70.95
3427.93		LMZ	206	356	50.31	30.91	14.43	0.01	0.21	n.d	n.d	0.03	3.37	0.23	99.49	69.37
3427.93		LMZ	206	357	50.29	31.07	14.46	n.d	0.21	n.d	0.01	0.03	3.33	0.18	99.58	69.86
3427.93		LMZ	210	358	50.36	31.01	14.49	0.01	0.26	0.02	0.01	0.04	3.32	0.18	99.69	69.95
3427.93		LMZ	210	359	50.30	31.00	14.36	0.01	0.24	n.d	0.02	0.04	3.39	0.19	99.55	69.31
3427.93		LMZ	210	360	50.02	31.08	14.62	0.03	0.28	n.d	n.d	0.02	3.30	0.21	99.55	70.17
		TM														
3618.98	1.36	LMZ	219	361	50.92	30.42	13.90	0.03	0.27	n.d	n.d	0.02	3.60	0.28	99.44	66.98
3618.98		LMZ	219	362	50.06	30.82	14.45	0.02	0.28	n.d	n.d	0.04	3.44	0.23	99.34	69.00
3618.98		LMZ	219	363	51.05	30.35	13.83	0.03	0.31	n.d	n.d	0.03	3.70	0.29	99.58	66.25
3618.98		LMZ	221	364	51.34	30.21	13.75	0.01	0.27	n.d	n.d	0.03	3.81	0.21	99.62	65.81
3618.98		LMZ	221	365	51.19	30.30	13.84	0.02	0.31	n.d	0.02	0.06	3.69	0.26	99.70	66.45
3618.98		LMZ	221	366	51.48	30.06	13.28	0.01	0.27	n.d	n.d	0.02	3.84	0.24	99.21	64.73
		TM														
3710.10	1.37	LMZ	226	430	50.72	31.00	14.24	0.03	0.25	n.d	0.01	0.02	3.51	0.17	99.96	68.49
3710.10		LMZ	226	431	50.55	30.63	14.14	0.02	0.32	0.01	0.01	0.02	3.60	0.21	99.50	67.64
3710.10		LMZ	226	432	49.30	31.66	15.20	0.01	0.28	n.d	n.d	n.d	2.97	0.13	99.56	73.32

Plag																
Depth	Sample	Zone	NO:	Point	SiO ₂	Al ₂ O ₃	CaO	MgO	FeO	MnO	Cr ₂ O ₃	TiO ₂	Na ₂ O	K ₂ O	Total	An%
3710.10		LMZ	228	433	51.30	30.33	13.52	0.01	0.21	0.03	0.01	n.d	3.82	0.26	99.48	65.18
3710.10		LMZ	228	434	51.28	30.29	13.78	0.02	0.27	n.d	n.d	0.04	3.66	0.25	99.58	66.53
3710.10		LMZ	228	435	50.52	30.42	13.85	0.01	0.28	n.d	n.d	0.02	3.58	0.23	98.91	67.23
		TM														
3795.28	1.38	LMZ	229	367	50.58	30.35	13.86	0.01	0.26	0.03	n.d	0.02	3.56	0.22	98.90	67.42
3795.28		LMZ	229	368	50.93	30.57	14.15	0.01	0.23	n.d	n.d	0.02	3.51	0.22	99.63	68.17
3795.28		LMZ	229	369	50.09	30.40	14.40	0.02	0.32	n.d	0.01	0.05	3.46	0.22	98.97	68.85
3795.28		LMZ	232	370	51.19	30.14	13.57	0.03	0.26	n.d	n.d	0.05	3.80	0.27	99.31	65.33
3795.28		LMZ	232	371	50.51	30.75	14.36	0.04	0.27	n.d	n.d	0.02	3.42	0.22	99.57	69.01
3795.28		LMZ	232	372	50.47	30.79	14.27	0.02	0.25	n.d	0.01	0.02	3.45	0.23	99.50	68.65
		TM														
3893.44	1.39	UCZ	236	436	49.42	31.40	15.03	0.02	0.33	n.d	n.d	0.02	3.04	0.19	99.46	72.43
3893.44		UCZ	236	437	49.19	31.56	15.31	0.02	0.28	0.02	0.02	0.04	2.87	0.18	99.48	73.90
3893.44		UCZ	236	438	48.81	31.51	15.39	0.03	0.29	0.02	0.01	0.02	2.80	0.18	99.07	74.44
3893.44		UCZ	238	439	49.20	31.95	15.49	0.01	0.30	n.d	0.01	0.09	2.70	0.15	99.91	75.34
3893.44		UCZ	238	440	49.00	31.91	15.49	0.03	0.30	0.01	n.d	n.d	2.80	0.17	99.71	74.61
3893.44		UCZ	238	441	49.09	31.86	15.47	n.d	0.25	n.d	0.01	0.02	2.84	0.15	99.68	74.43
		TM														
3972.90	1.39.1	UCZ	312	373	50.56	30.82	14.58	0.03	0.22	n.d	n.d	0.01	3.29	0.14	99.65	70.42
3972.90		UCZ	312	374	50.64	30.92	14.62	0.01	0.23	0.01	n.d	0.01	3.29	0.15	99.89	70.44
3972.90		UCZ	312	375	50.81	30.73	14.29	0.02	0.25	0.02	n.d	n.d	3.44	0.17	99.72	68.98
3972.90		UCZ	315	376	51.00	30.04	13.98	0.03	0.21	n.d	n.d	0.01	3.72	0.17	99.17	66.85
3972.90		UCZ	315	377	50.58	30.71	14.27	0.03	0.17	0.01	0.01	0.02	3.38	0.14	99.33	69.44
3972.90		UCZ	315	378	50.29	30.85	14.46	0.04	0.24	n.d	0.02	0.03	3.28	0.15	99.35	70.28
		TM														
4238.37	1.40	UCZ	243	424	49.26	31.30	15.36	0.05	0.36	n.d	n.d	0.04	2.77	0.18	99.32	74.61
4238.37		UCZ	243	425	49.19	31.49	15.38	0.03	0.30	n.d	0.01	0.01	2.78	0.17	99.37	74.60
4238.37		UCZ	243	426	49.46	31.32	15.10	0.04	0.39	0.01	0.01	0.04	2.92	0.18	99.47	73.32
4238.37		UCZ	244	421	49.24	31.56	15.42	0.05	0.30	n.d	n.d	0.03	2.81	0.17	99.58	74.49

Plag																
Depth	Sample	Zone	NO:	Point	SiO ₂	Al ₂ O ₃	CaO	MgO	FeO	MnO	Cr ₂ O ₃	TiO ₂	Na ₂ O	K ₂ O	Total	An%
4238.37		UCZ	244	422	49.55	31.64	15.43	0.05	0.34	0.02	0.01	0.04	2.68	0.17	99.93	75.35
4238.37		UCZ	244	423	49.24	31.29	15.36	0.04	0.32	0.01	n.d	0.04	2.89	0.18	99.36	73.85
	TM 1.41	UCZ	248	379	49.17	31.68	15.66	0.04	0.43	0.01	0.01	n.d	2.65	0.18	99.83	75.75
4335.85		UCZ	248	380	49.10	31.67	15.59	0.03	0.36	0.02	n.d	0.02	2.66	0.18	99.63	75.63
4335.85		UCZ	248	381	48.84	31.60	15.65	0.04	0.44	0.02	0.01	0.02	2.68	0.17	99.46	75.62
4335.85		UCZ	251	382	48.97	31.74	15.70	0.03	0.35	n.d	n.d	0.01	2.63	0.13	99.57	76.17
4335.85		UCZ	251	383	48.40	31.92	15.88	0.05	0.31	n.d	n.d	0.05	2.51	0.17	99.28	77.00
4335.85		UCZ	251	384	49.05	31.60	15.53	0.04	0.33	0.01	n.d	0.02	2.72	0.16	99.46	75.22
		UCZ	256	424	51.20	30.47	14.03	0.04	0.22	0.01	n.d	0.04	3.51	0.21	99.73	68.03
4434.09		UCZ	256	425	51.47	30.10	13.71	0.04	0.27	n.d	0.01	0.02	3.77	0.21	99.60	65.99
4434.09		UCZ	256	426	50.91	30.66	14.21	0.03	0.29	0.02	0.01	0.04	3.50	0.19	99.86	68.41
4434.09		UCZ	258	427	50.56	30.89	14.51	0.01	0.22	n.d	n.d	0.03	3.26	0.18	99.66	70.36
4434.09		UCZ	258	428	50.67	30.56	14.36	0.04	0.28	0.02	n.d	n.d	3.37	0.19	99.49	69.42
4434.09		UCZ	258	429	50.46	30.71	14.43	0.02	0.29	0.01	n.d	0.01	3.13	0.19	99.24	71.02
	TM 1.43	UCZ	259	385	50.13	31.36	15.06	0.04	0.29	0.02	n.d	n.d	3.05	0.18	100.13	72.43
4532.20		UCZ	259	386	49.73	31.44	15.20	0.05	0.24	n.d	0.01	0.04	2.93	0.18	99.82	73.36
4532.20		UCZ	259	387	50.18	31.22	14.75	0.03	0.24	n.d	0.02	n.d	3.11	0.16	99.71	71.70
4532.20		UCZ	262	388	50.28	31.49	14.90	0.02	0.25	0.01	n.d	n.d	3.09	0.17	100.21	71.99
4532.20		UCZ	262	389	49.75	30.96	15.23	0.62	0.44	0.02	0.03	0.04	2.90	0.15	100.15	73.72
4532.20		UCZ	262	390	50.16	31.33	15.06	0.03	0.23	n.d	n.d	0.02	3.05	0.18	100.05	72.43
	TM 1.44	UCZ	266	409	49.94	31.33	14.90	0.02	0.24	n.d	n.d	0.01	3.15	0.23	99.83	71.41
4654.76		UCZ	266	410	49.90	31.08	14.50	0.03	0.21	n.d	n.d	0.03	3.26	0.25	99.26	70.04
4654.76		UCZ	266	411	51.28	30.63	13.76	0.02	0.19	n.d	n.d	0.04	3.61	0.28	99.81	66.72
4654.76		UCZ	267	412	50.33	31.26	14.63	0.03	0.24	0.01	n.d	0.03	3.25	0.23	100.01	70.42
4654.76		UCZ	267	413	51.60	30.42	13.59	0.02	0.19	n.d	0.02	0.04	3.68	0.27	99.83	66.04

Depth	Sample	Zone	Plag													
			NO:	Point	SiO ₂	Al ₂ O ₃	CaO	MgO	FeO	MnO	Cr ₂ O ₃	TiO ₂	Na ₂ O	K ₂ O	Total	An%
4654.76		UCZ	267	414	51.32	30.25	13.61	0.01	0.12	n.d	0.02	0.03	3.71	0.28	99.36	65.86
	TM															
4753.11	1.45	UCZ	272	391	49.74	31.48	15.12	0.01	0.23	n.d	n.d	0.01	2.96	0.22	99.77	72.90
4753.11		UCZ	272	392	49.52	31.84	15.46	0.02	0.27	0.02	0.01	0.02	2.75	0.21	100.11	74.74
4753.11		UCZ	272	393	49.90	31.46	15.09	0.04	0.29	n.d	0.02	0.01	3.02	0.24	100.05	72.44
4753.11		UCZ	275	394	49.23	31.64	15.35	0.02	0.27	0.02	0.01	0.03	2.82	0.22	99.61	74.11
4753.11		UCZ	275	395	49.83	31.56	15.18	0.02	0.27	n.d	n.d	0.03	2.96	0.22	100.07	72.98
4753.11		UCZ	275	396	49.89	31.51	15.32	0.02	0.29	n.d	n.d	0.03	2.99	0.18	100.24	73.17
	TM															
4826.62	1.46	UCZ	279	415	48.80	32.04	15.68	0.04	0.17	0.01	n.d	0.02	2.63	0.17	99.56	75.98
4826.62		UCZ	279	416	49.24	31.86	15.48	0.02	0.21	n.d	n.d	0.01	2.71	0.18	99.70	75.16
4826.62		UCZ	279	417	49.04	32.00	15.75	0.03	0.19	0.03	0.01	0.01	2.72	0.17	99.94	75.44
4826.62		UCZ	282	418	49.14	31.97	15.63	0.03	0.20	n.d	n.d	0.03	2.68	0.18	99.87	75.55
4826.62		UCZ	282	419	49.31	31.74	15.58	0.02	0.21	0.01	0.02	0.02	2.77	0.19	99.86	74.84
4826.62		UCZ	282	420	49.13	31.84	15.54	0.04	0.19	n.d	0.02	0.04	2.61	0.15	99.56	76.02
	TM															
4924.39	1.47	LCZ	285	397	57.84	26.23	8.53	0.01	0.14	n.d	n.d	0.02	6.74	0.44	99.96	40.14
4924.39		LCZ	285	398	58.38	26.09	8.15	n.d	0.10	n.d	n.d	0.02	6.92	0.39	100.05	38.57
4924.39		LCZ	285	399	58.35	26.22	8.30	0.01	0.10	0.01	n.d	0.02	7.00	0.32	100.33	38.89
4924.39		LCZ	287	400	55.29	27.96	10.50	n.d	0.12	n.d	n.d	0.03	5.66	0.38	99.93	49.55
4924.39		LCZ	287	401	54.81	28.26	10.80	0.01	0.09	n.d	n.d	0.05	5.54	0.30	99.87	50.98
4924.39		LCZ	287	402	54.90	28.16	10.85	n.d	0.11	n.d	n.d	0.04	5.41	0.33	99.79	51.59
	TM															
4991.09	1.48	LCZ	289	403	53.65	29.02	11.76	0.02	0.08	n.d	0.01	0.03	4.87	0.28	99.72	56.23
4991.09		LCZ	289	404	54.04	29.00	11.56	0.02	0.13	0.02	0.02	0.03	5.08	0.13	100.02	55.27
4991.09		LCZ	289	405	53.89	29.05	11.69	0.01	0.17	0.02	n.d	0.03	5.10	0.07	100.02	55.67
4991.09		LCZ	293	406	53.32	29.20	12.19	n.d	0.08	0.02	0.01	0.01	4.69	0.20	99.71	58.28
4991.09		LCZ	293	407	53.05	29.19	12.15	0.02	0.09	n.d	n.d	0.01	4.82	0.15	99.48	57.71
4991.09		LCZ	293	408	52.66	29.56	12.45	0.02	0.08	0.01	n.d	n.d	4.54	0.18	99.51	59.65

Appendix C: The Sr-isotopic composition of plagioclase per analysed point, with depths reported in metres (m) from the Lower Critical Zone to the Upper Zone.

Depth	Sample	Plag#	Point	Zone	$^{87}\text{Sr}/^{86}\text{Sr}$	SE ($^{87}\text{Sr}/^{86}\text{Sr}$)	$^{87}\text{Rb}/^{86}\text{Sr}$	SE ($^{87}\text{Rb}/^{86}\text{Sr}$)	$^{87}\text{Sr}/^{86}\text{Sr}_i$	2SE	Rim/Core
65,66	TM 1.1	1	1	UZ	0,7089	2,76E-04	0,0404	2,99E-03	0,7077	5,79E-04	Core
65,66		1	5	UZ	0,7070	2,36E-04	0,0036	9,18E-05	0,7069	4,72E-04	Rim
65,66		1	3	UZ	0,7071	1,94E-04	0,0029	6,16E-05	0,7070	3,88E-04	Rim
65,66		2	8	UZ	0,7082	2,31E-04	0,0090	5,38E-04	0,7080	4,63E-04	Rim
65,66		2	10	UZ	0,7076	2,23E-04	0,0081	4,27E-04	0,7073	4,47E-04	Core
65,66		2	7	UZ	0,7079	1,97E-04	0,0045	1,06E-04	0,7078	3,94E-04	Rim
65,66		5	22	UZ	0,7065	2,34E-04	0,0029	7,47E-05	0,7064	4,68E-04	Core
65,66		5	25	UZ	0,7072	2,81E-04	0,0030	1,89E-04	0,7071	5,62E-04	Rim
65,66		5	441	UZ	0,7075	2,04E-04	0,0027	2,04E-04	0,7074	4,08E-04	Rim
65,66		5	22	UZ	0,7073	2,33E-04	0,0033	7,68E-05	0,7072	4,66E-04	Core
318,47	TM 1.5	21	131	UZ	0,7080	2,76E-04	0,0028	7,64E-05	0,7080	5,52E-04	Core
318,47		21	132	UZ	0,7074	2,77E-04	0,0043	9,06E-05	0,7073	5,54E-04	Rim
318,47		21	133	UZ	0,7071	2,80E-04	0,0016	8,09E-05	0,7070	5,60E-04	Rim
318,47		23	144	UZ	0,7072	2,77E-04	0,0018	6,63E-05	0,7071	5,54E-04	Rim
318,47		23	143	UZ	0,7070	2,87E-04	0,0011	6,72E-05	0,7070	5,74E-04	Rim
318,47		23	141	UZ	0,7069	2,34E-04	0,0019	6,82E-05	0,7069	4,68E-04	Core
318,47		24	147	UZ	0,7073	3,41E-04	0,0036	9,08E-05	0,7072	6,82E-04	Rim
318,47		24	150	UZ	0,7079	2,88E-04	0,0020	9,09E-05	0,7079	5,76E-04	Rim
318,47		24	146	UZ	0,7073	2,74E-04	0,0015	7,60E-05	0,7073	5,48E-04	Core
418,31	TM 1.6	26	99	UZ	0,7072	2,04E-04	0,0043	6,00E-05	0,7071	4,08E-04	Rim
418,31		26	97	UZ	0,7075	1,96E-04	0,0020	5,56E-05	0,7075	3,92E-04	Rim
418,31		26	100	UZ	0,7072	2,22E-04	0,0026	6,01E-05	0,7071	4,44E-04	Core
418,31		28	106	UZ	0,7076	2,26E-04	0,0057	6,51E-05	0,7075	4,52E-04	Core
418,31		28	109	UZ	0,7067	2,13E-04	0,0028	5,81E-05	0,7066	4,26E-04	Rim

Depth	Sample	Plag#	Point	Zone	$^{87}\text{Sr}/^{86}\text{Sr}$	SE ($^{87}\text{Sr}/^{86}\text{Sr}$)	$^{87}\text{Rb}/^{86}\text{Sr}$	SE ($^{87}\text{Rb}/^{86}\text{Sr}$)	$^{87}\text{Sr}/^{86}\text{Sr}_i$	2SE	Rim/Core
418,31		28	110	UZ	0,7083	2,37E-04	0,0052	1,22E-04	0,7081	4,74E-04	Rim
418,31		30	118	UZ	0,7086	1,96E-04	0,0023	4,60E-05	0,7086	3,92E-04	Rim
418,31		30	120	UZ	0,7074	2,03E-04	0,0032	6,52E-05	0,7073	4,06E-04	Core
418,31		30	117	UZ	0,7074	2,05E-04	0,0028	5,95E-05	0,7073	4,10E-04	Core
603,78	TM 1.8	38	162	UZ	0,7069	3,22E-04	0,0021	1,13E-04	0,7068	6,44E-04	Rim
603,78		38	160	UZ	0,7076	3,43E-04	0,0065	1,28E-04	0,7074	6,86E-04	Rim
603,78		38	161	UZ	0,7063	3,46E-04	0,0042	1,11E-04	0,7062	6,92E-04	Core
603,78		39	164	UZ	0,7070	4,39E-04	0,0014	1,21E-04	0,7069	8,78E-04	Rim
603,78		39	163	UZ	0,7066	4,07E-04	0,0008	1,05E-04	0,7065	8,14E-04	Rim
603,78		39	165	UZ	0,7070	3,66E-04	0,0012	1,07E-04	0,7069	7,32E-04	Core
603,78		42	167	UZ	0,7075	3,12E-04	0,0005	8,60E-05	0,7074	6,24E-04	Rim
603,78		42	166	UZ	0,7080	2,95E-04	0,0014	9,70E-05	0,7080	5,90E-04	Rim
603,78		42	168	UZ	0,7069	3,08E-04	0,0009	9,47E-05	0,7069	6,16E-04	Core
911,78	TM 1.11	56	188	UZ	0,7077	4,28E-04	0,0003	1,02E-04	0,7077	8,56E-04	Rim
911,78		56	189	UZ	0,7071	4,95E-04	0,0317	1,81E-03	0,7062	9,96E-04	Rim
911,78		56	190	UZ	0,7070	3,05E-04	0,0004	9,50E-05	0,7069	6,10E-04	Core
911,78		58	193	UZ	0,7072	1,93E-04	0,0338	2,82E-03	0,7063	4,19E-04	Rim
911,78		58	191	UZ	0,7077	1,92E-04	0,0507	3,43E-03	0,7062	4,32E-04	Rim
911,78		58	192	UZ	0,7074	1,58E-04	0,0029	1,54E-04	0,7073	3,16E-04	Core
911,78		59	196	UZ	0,7068	2,12E-04	0,0009	5,58E-05	0,7068	4,24E-04	Rim
911,78		59	195	UZ	0,7071	2,06E-04	0,0015	5,96E-05	0,7070	4,12E-04	Core
911,78		59	197	UZ	0,7075	2,33E-04	0,0008	5,55E-05	0,7074	4,66E-04	Rim
1104,46	TM 1.13	68	211	UZ	0,7066	2,97E-04	0,0004	7,63E-05	0,7066	5,94E-04	Core
1104,46		68	210	UZ	0,7074	2,39E-04	-0,0001	6,74E-05	0,7074	4,78E-04	Rim
1104,46		68	212	UZ	0,7065	2,53E-04	0,0003	7,18E-05	0,7065	5,06E-04	Rim
1104,46		69	213	UZ	0,7076	2,39E-04	0,0002	7,15E-05	0,7076	4,78E-04	Rim
1104,46		69	214	UZ	0,7068	2,50E-04	0,0003	7,53E-05	0,7068	5,00E-04	Core
1104,46		69	215	UZ	0,7068	2,62E-04	0,0004	7,34E-05	0,7067	5,24E-04	Core

Depth	Sample	Plag#	Point	Zone	$^{87}\text{Sr}/^{86}\text{Sr}$	SE ($^{87}\text{Sr}/^{86}\text{Sr}$)	$^{87}\text{Rb}/^{86}\text{Sr}$	SE ($^{87}\text{Rb}/^{86}\text{Sr}$)	$^{87}\text{Sr}/^{86}\text{Sr}_i$	2SE	Rim/Core
1104,46		72	217	UZ	0,7064	3,75E-04	0,0002	1,10E-04	0,7064	7,50E-04	Core
1104,46		72	218	UZ	0,7077	0,000296	0,0002	0,000096	0,7077	5,92E-04	Rim
1104,46		72	216	UZ	0,7077	0,003880	0,0012	0,001350	0,7076	7,76E-03	Rim
1201,54	TM 1.13.1	73	220	UMZ	0,7077	2,26E-04	0,0099	3,70E-04	0,7074	4,53E-04	Rim
1201,54		73	222	UMZ	0,7063	3,61E-04	0,0033	7,76E-05	0,7062	7,22E-04	Core
1201,54		73	221	UMZ	0,7084	2,33E-04	0,0692	8,98E-04	0,7064	4,69E-04	Core
1201,54		78	226	UMZ	0,7082	2,59E-04	0,0127	4,24E-04	0,7078	5,19E-04	Rim
1201,54		78	227	UMZ	0,7085	2,33E-04	0,0066	8,98E-05	0,7083	4,66E-04	Core
1201,54		78	228	UMZ	0,7076	2,60E-04	0,0049	9,74E-05	0,7074	5,20E-04	Rim
1201,54		75	225	UMZ	0,7073	7,32E-04	0,0114	6,37E-04	0,7069	1,46E-03	Rim
1201,54		75	223	UMZ	0,7074	3,26E-04	0,0140	5,99E-04	0,7070	6,53E-04	Rim
1201,54		75	224	UMZ	0,7076	3,32E-04	0,0052	8,91E-05	0,7075	6,64E-04	Core
1299,49	TM 1.13.2	79	229	UMZ	0,7075	3,07E-04	0,0010	7,98E-05	0,7075	6,14E-04	Rim
1299,49		79	230	UMZ	0,7064	2,92E-04	0,0037	1,32E-04	0,7063	5,84E-04	Rim
1299,49		79	231	UMZ	0,7082	2,69E-04	0,0017	7,72E-05	0,7082	5,38E-04	Core
1299,49		82	232	UMZ	0,7078	2,64E-04	0,0022	8,20E-05	0,7077	5,28E-04	Rim
1299,49		82	233	UMZ	0,7077	2,99E-04	0,0011	8,29E-05	0,7077	5,98E-04	Core
1299,49		82	234	UMZ	0,7077	2,99E-04	0,0010	8,07E-05	0,7077	5,98E-04	Rim
1299,49		84	236	UMZ	0,7082	2,99E-04	0,0075	2,65E-04	0,7080	5,98E-04	Core
1299,49		84	237	UMZ	0,7067	2,89E-04	0,0006	8,10E-05	0,7067	5,78E-04	Rim
1299,49		84	235	UMZ	0,7080	2,93E-04	0,0023	7,86E-05	0,7079	5,86E-04	Rim
1349,35	TM 1.13.3	295	240	UMZ	0,7070	4,73E-04	0,0021	1,14E-04	0,7069	9,46E-04	Rim
1349,35		295	238	UMZ	0,7069	4,31E-04	0,0032	1,00E-04	0,7068	8,62E-04	Core
1349,35		298	245	UMZ	0,7071	3,01E-04	0,0087	3,81E-04	0,7069	6,02E-04	Rim
1349,35		298	246	UMZ	0,7074	3,25E-04	0,0072	1,71E-04	0,7071	6,50E-04	Rim
1349,35		298	244	UMZ	0,7080	4,02E-04	0,0034	1,08E-04	0,7079	8,04E-04	Core
1349,35		297	243	UMZ	0,7069	3,72E-04	0,0032	1,13E-04	0,7068	7,44E-04	Rim
1349,35		297	242	UMZ	0,7084	3,78E-04	0,0015	1,38E-04	0,7083	7,56E-04	Rim

Depth	Sample	Plag#	Point	Zone	$^{87}\text{Sr}/^{86}\text{Sr}$	SE ($^{87}\text{Sr}/^{86}\text{Sr}$)	$^{87}\text{Rb}/^{86}\text{Sr}$	SE ($^{87}\text{Rb}/^{86}\text{Sr}$)	$^{87}\text{Sr}/^{86}\text{Sr}_i$	2SE	Rim/Core
1349,35		297	241	UMZ	0,7073	4,34E-04	0,0013	1,12E-04	0,7073	8,68E-04	Core
1519,05	TM 1.14	85	248	UMZ	0,7077	2,67E-04	0,0380	1,32E-03	0,7066	5,39E-04	Core
1519,05		85	249	UMZ	0,7074	2,66E-04	0,0095	4,15E-04	0,7071	5,33E-04	Rim
1519,05		85	247	UMZ	0,7068	2,88E-04	0,0087	1,87E-04	0,7066	5,76E-04	Rim
1519,05		89	251	UMZ	0,7072	3,65E-04	0,0103	3,07E-04	0,7069	7,30E-04	Core
1519,05		89	250	UMZ	0,7081	3,13E-04	0,0197	2,42E-04	0,7075	6,26E-04	Rim
1519,05		89	252	UMZ	0,7069	2,77E-04	0,0123	3,51E-04	0,7066	5,54E-04	Rim
1519,05		90	255	UMZ	0,7073	3,20E-04	0,0019	9,26E-05	0,7073	6,40E-04	Core
1519,05		90	254	UMZ	0,7086	3,98E-04	0,0023	1,31E-04	0,7085	7,96E-04	Rim
1519,05		90	253	UMZ	0,7076	3,34E-04	0,0048	9,92E-05	0,7075	6,68E-04	Rim
1616,47	TM 1.15	91	256	UMZ	0,7074	3,29E-04	0,0012	1,20E-04	0,7074	6,58E-04	Rim
1616,47		91	258	UMZ	0,7076	3,78E-04	0,0013	1,01E-04	0,7076	7,56E-04	Rim
1616,47		91	257	UMZ	0,7070	4,75E-04	0,0024	1,12E-04	0,7069	9,50E-04	Core
1616,47		93	260	UMZ	0,7075	3,58E-04	0,0012	9,13E-05	0,7075	7,16E-04	Rim
1616,47		93	261	UMZ	0,7077	2,87E-04	0,0007	7,37E-05	0,7077	5,74E-04	Rim
1616,47		93	259	UMZ	0,7072	3,21E-04	0,0012	8,65E-05	0,7071	6,42E-04	Core
1616,47		96	263	UMZ	0,7074	3,08E-04	0,0009	8,42E-05	0,7073	6,16E-04	Rim
1616,47		96	264	UMZ	0,7074	2,64E-04	0,0014	7,23E-05	0,7074	5,28E-04	Rim
1616,47		96	265	UMZ	0,7079	2,77E-04	0,0020	8,66E-05	0,7078	5,54E-04	Core
1757,02	TM 1.16.1	307	282	UMZ	0,7073	3,26E-04	0,0008	8,78E-05	0,7072	6,52E-04	Rim
1757,02		307	283	UMZ	0,7077	2,95E-04	0,0009	7,87E-05	0,7077	5,90E-04	Core
1757,02		307	284	UMZ	0,7068	2,41E-04	0,0013	6,27E-05	0,7068	4,82E-04	Rim
1757,02		308	442	UMZ	0,7079	2,51E-04	0,0010	7,39E-05	0,7079	5,02E-04	Rim
1757,02		308	443	UMZ	0,7078	2,53E-04	0,0011	6,57E-05	0,7078	5,06E-04	Core
1757,02		308	444	UMZ	0,7078	2,15E-04	0,0011	6,38E-05	0,7078	4,30E-04	Rim
1782,05	TM 1.17	103	287	LMZ	0,7080	3,11E-04	0,0027	9,49E-05	0,7079	6,22E-04	Rim
1782,05		103	286	LMZ	0,7085	2,73E-04	0,0185	5,74E-04	0,7079	5,47E-04	Rim
1782,05		103	286	LMZ	0,7080	2,91E-04	0,0119	4,16E-04	0,7077	5,82E-04	Rim

Depth	Sample	Plag#	Point	Zone	$^{87}\text{Sr}/^{86}\text{Sr}$	SE ($^{87}\text{Sr}/^{86}\text{Sr}$)	$^{87}\text{Rb}/^{86}\text{Sr}$	SE ($^{87}\text{Rb}/^{86}\text{Sr}$)	$^{87}\text{Sr}/^{86}\text{Sr}_i$	2SE	Rim/Core
1782,05		103	285	LMZ	0,7091	2,63E-04	0,0141	6,38E-04	0,7087	5,27E-04	Core
1782,05		105	290	LMZ	0,7087	2,96E-04	0,0042	8,11E-05	0,7086	5,92E-04	Rim
1782,05		105	289	LMZ	0,7085	2,91E-04	0,0026	8,82E-05	0,7084	5,82E-04	Core
1782,05		105	288	LMZ	0,7070	2,65E-04	0,0033	7,90E-05	0,7069	5,30E-04	Rim
1782,05		107	291	LMZ	0,7083	2,74E-04	0,0033	8,66E-05	0,7082	5,48E-04	Rim
1782,05		107	292	LMZ	0,7078	2,73E-04	0,0030	9,61E-05	0,7077	5,46E-04	Rim
1782,05		107	293	LMZ	0,7108	2,74E-04	0,1252	3,17E-03	0,7072	5,78E-04	Rim
1782,05		107	445	LMZ	0,7081	2,71E-04	0,0040	7,50E-05	0,7080	5,42E-04	Core
1978,02	TM 1.19	115	304	LMZ	0,7081	4,70E-04	0,0051	1,09E-04	0,7080	9,40E-04	Rim
1978,02		115	303	LMZ	0,7094	4,94E-04	0,0062	1,46E-04	0,7093	9,88E-04	Core
1978,02		115	305	LMZ	0,7090	4,97E-04	0,0173	3,01E-04	0,7085	9,94E-04	Rim
1978,02		117	308	LMZ	0,7081	3,62E-04	0,0060	8,94E-05	0,7079	7,24E-04	Core
1978,02		117	306	LMZ	0,7090	3,38E-04	0,0063	1,21E-04	0,7088	6,76E-04	Rim
1978,02		117	307	LMZ	0,7095	3,65E-04	0,0074	8,32E-05	0,7093	7,30E-04	Rim
1978,02		120	309	LMZ	0,7090	3,44E-04	0,0047	9,55E-05	0,7088	6,88E-04	Rim
1978,02		120	310	LMZ	0,7085	3,41E-04	0,0047	1,07E-04	0,7084	6,82E-04	Rim
1978,02		120	311	LMZ	0,7085	3,50E-04	0,0039	8,94E-05	0,7083	7,00E-04	Rim
2274,98	TM 1.22	133	446	LMZ	0,7065	3,64E-04	0,0060	1,01E-04	0,7063	7,28E-04	Core
2274,98		133	447	LMZ	0,7069	3,47E-04	0,0028	1,03E-04	0,7069	6,94E-04	Rim
2274,98		133	448	LMZ	0,7095	3,79E-04	0,0058	1,12E-04	0,7094	7,58E-04	Rim
2274,98		136	320	LMZ	0,7082	3,84E-04	0,0055	1,12E-04	0,7080	7,68E-04	Rim
2274,98		136	319	LMZ	0,7080	3,50E-04	0,0065	2,23E-04	0,7078	7,00E-04	Core
2274,98		136	318	LMZ	0,7073	3,87E-04	0,0046	1,11E-04	0,7071	7,74E-04	Rim
2274,98		138	323	LMZ	0,7086	2,42E-04	0,0058	7,95E-05	0,7084	4,84E-04	Rim
2274,98		138	322	LMZ	0,7087	2,21E-04	0,0054	7,38E-05	0,7086	4,42E-04	Core
2274,98		138	321	LMZ	0,7078	2,58E-04	0,0037	1,03E-04	0,7077	5,16E-04	Rim
2448,40	TM 1.24	150	449	LMZ	0,7082	2,35E-04	0,0023	8,04E-05	0,7081	4,70E-04	Rim
2448,40		150	450	LMZ	0,7081	2,22E-04	0,0033	5,50E-05	0,7080	4,44E-04	Core

Depth	Sample	Plag#	Point	Zone	$^{87}\text{Sr}/^{86}\text{Sr}$	SE ($^{87}\text{Sr}/^{86}\text{Sr}$)	$^{87}\text{Rb}/^{86}\text{Sr}$	SE ($^{87}\text{Rb}/^{86}\text{Sr}$)	$^{87}\text{Sr}/^{86}\text{Sr}_i$	2SE	Rim/Core
2448,40		150	451	LMZ	0,7091	2,23E-04	0,0032	7,44E-05	0,7090	4,46E-04	Rim
2448,40		149	330	LMZ	0,7088	2,48E-04	0,0033	6,23E-05	0,7087	4,96E-04	Rim
2448,40		149	329	LMZ	0,7089	2,41E-04	0,0033	6,95E-05	0,7088	4,82E-04	Rim
2448,40		149	327	LMZ	0,7083	2,39E-04	0,0041	6,15E-05	0,7082	4,78E-04	Core
2448,40		145	326	LMZ	0,7076	3,69E-04	0,0055	2,24E-04	0,7075	7,38E-04	Rim
2448,40		145	324	LMZ	0,7086	2,55E-04	0,0039	7,63E-05	0,7085	5,10E-04	Core
2448,40		145	325	LMZ	0,7085	3,23E-04	0,0038	1,10E-04	0,7084	6,46E-04	Rim
2639,06	TM 1.26	158	333	LMZ	0,7087	2,74E-04	0,0148	1,42E-03	0,7082	5,54E-04	Rim
2639,06		158	332	LMZ	0,7080	2,54E-04	0,0042	1,03E-04	0,7079	5,08E-04	Rim
2639,06		158	331	LMZ	0,7088	2,79E-04	0,0032	7,43E-05	0,7087	5,58E-04	Rim
2639,06		159	452	LMZ	0,7085	2,86E-04	0,0060	1,25E-04	0,7083	5,72E-04	Rim
2639,06		159	453	LMZ	0,7089	2,56E-04	0,0027	8,26E-05	0,7089	5,12E-04	Rim
2639,06		159	454	LMZ	0,7094	2,89E-04	0,0358	3,65E-04	0,7084	5,78E-04	Core
2639,06		161	336	LMZ	0,7074	2,89E-04	0,0015	8,07E-05	0,7074	5,78E-04	Rim
2639,06		161	334	LMZ	0,7083	2,81E-04	0,0031	8,06E-05	0,7082	5,62E-04	Core
2639,06		161	335	LMZ	0,7084	2,78E-04	0,0023	7,73E-05	0,7084	5,56E-04	Rim
2841,74	TM 1.28	174	340	LMZ	0,7091	2,52E-04	0,0046	6,52E-05	0,7090	5,04E-04	Core
2841,74		174	341	LMZ	0,7089	2,65E-04	0,0047	7,34E-05	0,7088	5,30E-04	Core
2841,74		174	342	LMZ	0,7084	2,23E-04	0,0023	7,00E-05	0,7083	4,46E-04	Rim
2841,74		171	339	LMZ	0,7089	2,43E-04	0,0015	7,79E-05	0,7088	4,86E-04	Rim
2841,74		171	338	LMZ	0,7084	2,44E-04	0,0033	7,62E-05	0,7083	4,88E-04	Core
2841,74		171	337	LMZ	0,7086	2,42E-04	0,0014	6,68E-05	0,7086	4,84E-04	Rim
2841,74		169	455	LMZ	0,7094	2,50E-04	0,0035	6,96E-05	0,7093	5,00E-04	Core
2841,74		169	456	LMZ	0,7082	2,15E-04	0,0022	6,95E-05	0,7082	4,30E-04	Rim
2841,74		169	457	LMZ	0,7087	2,37E-04	0,0010	7,63E-05	0,7087	4,74E-04	Rim
3035,77	TM 1.30	181	458	LMZ	0,7072	2,90E-04	0,0023	9,35E-05	0,7071	5,80E-04	Rim
3035,77		181	459	LMZ	0,7088	3,45E-04	0,0141	9,53E-04	0,7084	6,92E-04	Core
3035,77		181	460	LMZ	0,7082	2,97E-04	0,0016	8,54E-05	0,7082	5,94E-04	Rim

Depth	Sample	Plag#	Point	Zone	$^{87}\text{Sr}/^{86}\text{Sr}$	SE ($^{87}\text{Sr}/^{86}\text{Sr}$)	$^{87}\text{Rb}/^{86}\text{Sr}$	SE ($^{87}\text{Rb}/^{86}\text{Sr}$)	$^{87}\text{Sr}/^{86}\text{Sr}_i$	2SE	Rim/Core
3035,77		183	343	LMZ	0,7084	2,91E-04	0,0017	7,84E-05	0,7083	5,82E-04	Rim
3035,77		183	344	LMZ	0,7090	2,53E-04	0,0047	1,37E-04	0,7089	5,06E-04	Core
3035,77		183	345	LMZ	0,7088	2,52E-04	0,0077	1,65E-04	0,7086	5,04E-04	Rim
3035,77		185	346	LMZ	0,7087	2,94E-04	0,0017	8,28E-05	0,7087	5,88E-04	Core
3035,77		185	347	LMZ	0,7086	2,57E-04	0,0027	1,05E-04	0,7085	5,14E-04	Rim
3035,77		185	348	LMZ	0,7090	2,63E-04	0,0035	1,00E-04	0,7089	5,26E-04	Rim
3230,89	TM 1.32	195	461	LMZ	0,7096	2,87E-04	0,0018	7,34E-05	0,7096	5,74E-04	Rim
3230,89		195	462	LMZ	0,7093	3,05E-04	0,0022	8,57E-05	0,7092	6,10E-04	Core
3230,89		195	463	LMZ	0,7150	3,02E-04	0,2887	4,68E-03	0,7067	6,62E-04	Rim
3230,89		196	350	LMZ	0,7100	2,99E-04	0,0019	1,27E-04	0,7100	5,98E-04	Rim
3230,89		196	351	LMZ	0,7090	2,98E-04	0,0019	7,58E-05	0,7090	5,96E-04	Core
3230,89		196	349	LMZ	0,7096	2,67E-04	0,0090	4,20E-04	0,7093	5,35E-04	Rim
3230,89		197	354	LMZ	0,7099	3,99E-04	0,0156	1,92E-04	0,7095	7,98E-04	Core
3230,89		197	353	LMZ	0,7085	3,44E-04	0,0056	1,31E-04	0,7083	6,88E-04	Rim
3230,89		197	352	LMZ	0,7082	3,74E-04	0,0036	1,01E-04	0,7081	7,48E-04	Rim
3427,93	TM 1.34	206	357	LMZ	0,7091	2,75E-04	0,0033	1,38E-04	0,7090	5,50E-04	Rim
3427,93		206	356	LMZ	0,7089	2,93E-04	0,0022	8,47E-05	0,7088	5,86E-04	Core
3427,93		206	355	LMZ	0,7087	2,45E-04	0,0032	7,60E-05	0,7086	4,90E-04	Rim
3427,93		207	464	LMZ	0,7083	3,61E-04	0,0045	1,26E-04	0,7082	7,22E-04	Rim
3427,93		207	465	LMZ	0,7080	3,27E-04	0,0064	1,14E-04	0,7078	6,54E-04	Rim
3427,93		207	466	LMZ	0,7090	3,99E-04	0,0184	1,47E-03	0,7085	8,03E-04	Core
3427,93		210	359	LMZ	0,7081	2,77E-04	0,0024	7,85E-05	0,7081	5,54E-04	Rim
3427,93		210	358	LMZ	0,7089	2,89E-04	0,0022	8,45E-05	0,7088	5,78E-04	Rim
3427,93		210	360	LMZ	0,7083	2,30E-04	0,0025	8,20E-05	0,7083	4,60E-04	Rim
3618,98	TM 1.36	218	467	LMZ	0,7091	2,89E-04	0,0013	9,71E-05	0,7090	5,78E-04	Rim
3618,98		218	468	LMZ	0,7091	2,50E-04	0,0018	7,74E-05	0,7091	5,00E-04	Rim
3618,98		218	469	LMZ	0,7090	2,59E-04	0,0038	7,85E-05	0,7089	5,18E-04	Core
3618,98		219	362	LMZ	0,7093	2,87E-04	0,0029	7,53E-05	0,7092	5,74E-04	Rim

Depth	Sample	Plag#	Point	Zone	$^{87}\text{Sr}/^{86}\text{Sr}$	SE ($^{87}\text{Sr}/^{86}\text{Sr}$)	$^{87}\text{Rb}/^{86}\text{Sr}$	SE ($^{87}\text{Rb}/^{86}\text{Sr}$)	$^{87}\text{Sr}/^{86}\text{Sr}_i$	2SE	Rim/Core
3618,98		219	361	LMZ	0,7092	2,61E-04	0,0039	8,23E-05	0,7091	5,22E-04	Core
3618,98		219	363	LMZ	0,7099	3,19E-04	0,0041	1,02E-04	0,7097	6,38E-04	Core
3618,98		221	365	LMZ	0,7082	3,20E-04	0,0019	9,42E-05	0,7082	6,40E-04	Core
3618,98		221	364	LMZ	0,7074	4,12E-04	0,0054	1,39E-04	0,7072	8,24E-04	Rim
3618,98		221	366	LMZ	0,7083	2,82E-04	0,0026	8,08E-05	0,7082	5,64E-04	Rim
3795,28	TM 1.38	229	367	LMZ	0,7082	3,99E-04	0,0065	2,33E-04	0,7080	7,98E-04	Rim
3795,28		229	368	LMZ	0,7079	3,07E-04	0,0031	9,93E-05	0,7078	6,14E-04	Rim
3795,28		229	369	LMZ	0,7091	3,93E-04	0,0255	5,87E-04	0,7084	7,87E-04	Core
3795,28		232	370	LMZ	0,7086	2,97E-04	0,0026	8,77E-05	0,7085	5,94E-04	Rim
3795,28		232	371	LMZ	0,7081	2,71E-04	0,0027	8,08E-05	0,7080	5,42E-04	Core
3795,28		232	372	LMZ	0,7075	2,79E-04	0,0031	1,09E-04	0,7074	5,58E-04	Rim
3795,28		234	470	LMZ	0,7082	2,75E-04	0,0021	8,17E-05	0,7081	5,50E-04	Rim
3795,28		234	471	LMZ	0,7072	2,73E-04	0,0018	8,18E-05	0,7072	5,46E-04	Core
3795,28		234	472	LMZ	0,7086	2,60E-04	0,0023	1,59E-04	0,7085	5,20E-04	Rim
3893,44	TM 1.39	236	436	UCZ	0,7080	2,96E-04	0,0023	8,49E-05	0,7079	5,92E-04	Rim
3893,44		236	437	UCZ	0,7078	2,83E-04	0,0015	8,52E-05	0,7077	5,66E-04	Core
3893,44		236	438	UCZ	0,7080	2,83E-04	0,0020	9,01E-05	0,7080	5,66E-04	Rim
3893,44		238	441	UCZ	0,7076	2,88E-04	0,0018	9,90E-05	0,7076	5,76E-04	Rim
3893,44		238	439	UCZ	0,7069	3,04E-04	0,0025	9,61E-05	0,7068	6,08E-04	Core
3893,44		238	440	UCZ	0,7085	2,65E-04	0,0015	8,22E-05	0,7085	5,30E-04	Rim
3893,44		240	473	UCZ	0,7083	2,96E-04	0,0017	1,16E-04	0,7083	5,92E-04	Core
3893,44		240	474	UCZ	0,7086	2,87E-04	0,0050	2,84E-04	0,7085	5,74E-04	Rim
3893,44		240	475	UCZ	0,7078	2,82E-04	0,0015	1,03E-04	0,7078	5,64E-04	Rim
3972,90	TM 1.39.1	312	375	UCZ	0,7066	1,98E-04	0,0048	6,26E-05	0,7065	3,96E-04	Rim
3972,90		312	374	UCZ	0,7073	2,02E-04	0,0050	5,57E-05	0,7071	4,04E-04	Core
3972,90		312	373	UCZ	0,7067	2,08E-04	0,0050	5,48E-05	0,7066	4,16E-04	Rim
3972,90		315	377	UCZ	0,7063	2,08E-04	0,0048	5,68E-05	0,7062	4,16E-04	Core
3972,90		315	378	UCZ	0,7064	2,09E-04	0,0048	6,01E-05	0,7063	4,18E-04	Rim

Depth	Sample	Plag#	Point	Zone	$^{87}\text{Sr}/^{86}\text{Sr}$	SE ($^{87}\text{Sr}/^{86}\text{Sr}$)	$^{87}\text{Rb}/^{86}\text{Sr}$	SE ($^{87}\text{Rb}/^{86}\text{Sr}$)	$^{87}\text{Sr}/^{86}\text{Sr}_i$	2SE	Rim/Core
3972,90		315	376	UCZ	0,7066	1,99E-04	0,0049	5,85E-05	0,7065	3,98E-04	Rim
3972,90		316	476	UCZ	0,7070	1,99E-04	0,0049	5,63E-05	0,7068	3,98E-04	Core
3972,90		316	477	UCZ	0,7065	2,07E-04	0,0045	6,04E-05	0,7064	4,14E-04	Rim
3972,90		316	478	UCZ	0,7063	1,99E-04	0,0049	5,31E-05	0,7061	3,98E-04	Rim
4238,37	TM 1.40	243	424	UCZ	0,7068	2,31E-04	0,0111	6,99E-05	0,7065	4,62E-04	Rim
4238,37		243	425	UCZ	0,7061	2,31E-04	0,0079	6,02E-05	0,7059	4,62E-04	Rim
4238,37		243	426	UCZ	0,7058	1,99E-04	0,0099	6,88E-05	0,7055	3,98E-04	Rim
4238,37		244	422	UCZ	0,7063	2,30E-04	0,0068	6,78E-05	0,7061	4,60E-04	Rim
4238,37		244	421	UCZ	0,7063	2,03E-04	0,0082	6,39E-05	0,7061	4,06E-04	Rim
4238,37		244	423	UCZ	0,7063	2,16E-04	0,0079	6,80E-05	0,7061	4,32E-04	Core
4238,37		246	479	UCZ	0,7072	3,65E-04	0,0077	1,05E-04	0,7070	7,30E-04	Rim
4238,37		246	480	UCZ	0,7059	3,18E-04	0,0066	8,22E-05	0,7057	6,36E-04	Core
4238,37		246	481	UCZ	0,7066	2,72E-04	0,0081	9,14E-05	0,7063	5,44E-04	Rim
4335,85	TM 1.41	248	381	UCZ	0,7070	3,95E-04	0,0089	2,23E-04	0,7067	7,90E-04	Core
4335,85		248	380	UCZ	0,7065	3,86E-04	0,0133	3,50E-04	0,7061	7,72E-04	Core
4335,85		248	379	UCZ	0,7058	3,48E-04	0,0055	1,64E-04	0,7057	6,96E-04	Rim
4335,85		251	383	UCZ	0,7070	2,44E-04	0,0050	8,53E-05	0,7068	4,88E-04	Rim
4335,85		251	384	UCZ	0,7068	2,39E-04	0,0074	7,68E-05	0,7066	4,78E-04	Core
4335,85		251	382	UCZ	0,7066	2,16E-04	0,0060	2,36E-04	0,7064	4,32E-04	Rim
4335,85		252	482	UCZ	0,7076	2,45E-04	0,0050	7,12E-05	0,7075	4,90E-04	Rim
4335,85		252	483	UCZ	0,7061	2,33E-04	0,0049	9,19E-05	0,7059	4,66E-04	Core
4335,85		252	484	UCZ	0,7073	2,35E-04	0,0061	7,36E-05	0,7071	4,70E-04	Rim
4434,09	TM 1.42	254	485	UCZ	0,7065	2,98E-04	0,0092	7,58E-05	0,7062	5,96E-04	Rim
4434,09		254	486	UCZ	0,7046	9,87E-04	0,0109	8,55E-04	0,7042	1,97E-03	Core
4434,09		256	425	UCZ	0,7061	2,21E-04	0,0099	6,56E-05	0,7058	4,42E-04	Rim
4434,09		256	426	UCZ	0,7070	2,02E-04	0,0110	6,66E-05	0,7067	4,04E-04	Rim
4434,09		256	424	UCZ	0,7063	2,10E-04	0,0106	6,64E-05	0,7060	4,20E-04	Core
4434,09		258	428	UCZ	0,7067	3,05E-04	0,0102	9,68E-05	0,7064	6,10E-04	Core

Depth	Sample	Plag#	Point	Zone	$^{87}\text{Sr}/^{86}\text{Sr}$	SE ($^{87}\text{Sr}/^{86}\text{Sr}$)	$^{87}\text{Rb}/^{86}\text{Sr}$	SE ($^{87}\text{Rb}/^{86}\text{Sr}$)	$^{87}\text{Sr}/^{86}\text{Sr}_i$	2SE	Rim/Core
4434,09		258	427	UCZ	0,7057	3,19E-04	0,0102	8,25E-05	0,7054	6,38E-04	Rim
4434,09		258	429	UCZ	0,7062	2,52E-04	0,0100	7,56E-05	0,7059	5,04E-04	Rim
4532,20	TM 1.43	259	387	UCZ	0,7066	1,97E-04	0,0048	6,81E-05	0,7065	3,94E-04	Rim
4532,20		259	386	UCZ	0,7069	2,62E-04	0,0046	6,82E-05	0,7068	5,24E-04	Core
4532,20		259	385	UCZ	0,7064	2,23E-04	0,0045	6,77E-05	0,7063	4,46E-04	Rim
4532,20		260	487	UCZ	0,7062	2,75E-04	0,0045	8,54E-05	0,7061	5,50E-04	Rim
4532,20		260	488	UCZ	0,7064	2,98E-04	0,0053	8,70E-05	0,7063	5,96E-04	Rim
4532,20		260	489	UCZ	0,7059	2,91E-04	0,0049	7,77E-05	0,7058	5,82E-04	Core
4532,20		262	390	UCZ	0,7060	3,20E-04	0,0054	8,34E-05	0,7058	6,40E-04	Rim
4532,20		262	388	UCZ	0,7066	4,97E-04	0,0526	4,04E-03	0,7051	1,02E-03	Rim
4532,20		262	389	UCZ	0,7066	3,41E-04	0,0089	1,62E-04	0,7063	6,82E-04	Core
4654,76	TM 1.44	266	409	UCZ	0,7059	2,34E-04	0,0093	6,73E-05	0,7057	4,68E-04	Rim
4654,76		266	411	UCZ	0,7061	2,37E-04	0,0104	6,59E-05	0,7058	4,74E-04	Rim
4654,76		266	410	UCZ	0,7062	2,27E-04	0,0108	7,30E-05	0,7059	4,54E-04	Rim
4654,76		267	414	UCZ	0,7062	2,02E-04	0,0120	6,74E-05	0,7059	4,04E-04	Rim
4654,76		267	413	UCZ	0,7061	1,85E-04	0,0102	5,66E-05	0,7058	3,70E-04	Rim
4654,76		267	412	UCZ	0,7060	1,95E-04	0,0103	5,71E-05	0,7057	3,90E-04	Rim
4654,76		268	490	UCZ	0,7063	2,49E-04	0,0123	8,31E-05	0,7059	4,98E-04	Core
4654,76		268	491	UCZ	0,7069	3,13E-04	0,0127	1,02E-04	0,7065	6,26E-04	Rim
4654,76		268	492	UCZ	0,7057	2,07E-04	0,0101	7,11E-05	0,7055	4,14E-04	Rim
4753,11	TM 1.45	271	493	UCZ	0,7051	2,25E-04	0,0032	6,32E-05	0,7050	4,50E-04	Core
4753,11		271	494	UCZ	0,7068	2,16E-04	0,0041	5,81E-05	0,7067	4,32E-04	Rim
4753,11		271	495	UCZ	0,7062	1,70E-04	0,0049	1,12E-04	0,7060	3,40E-04	Rim
4753,11		272	392	UCZ	0,7059	2,36E-04	0,0036	8,20E-05	0,7058	4,72E-04	Rim
4753,11		272	391	UCZ	0,7062	2,86E-04	0,0043	1,04E-04	0,7060	5,72E-04	Rim
4753,11		272	393	UCZ	0,7062	2,43E-04	0,0045	7,15E-05	0,7060	4,86E-04	Rim
4753,11		275	394	UCZ	0,7063	3,04E-04	0,0037	1,09E-04	0,7062	6,08E-04	Rim
4753,11		275	395	UCZ	0,7063	2,61E-04	0,0129	1,80E-04	0,7060	5,22E-04	Rim

Depth	Sample	Plag#	Point	Zone	$^{87}\text{Sr}/^{86}\text{Sr}$	SE ($^{87}\text{Sr}/^{86}\text{Sr}$)	$^{87}\text{Rb}/^{86}\text{Sr}$	SE ($^{87}\text{Rb}/^{86}\text{Sr}$)	$^{87}\text{Sr}/^{86}\text{Sr}_i$	2SE	Rim/Core
4753,11		275	396	UCZ	0,7061	2,31E-04	0,0045	6,07E-05	0,7060	4,62E-04	Rim
4753,11		275	496	UCZ	0,7063	2,24E-04	0,0049	6,08E-05	0,7062	4,48E-04	Core
4826,62	TM 1.46	277	497	UCZ	0,7061	2,65E-04	0,0054	7,41E-05	0,7059	5,30E-04	Core
4826,62		277	498	UCZ	0,7059	2,63E-04	0,0044	7,33E-05	0,7058	5,26E-04	Rim
4826,62		277	499	UCZ	0,7062	2,45E-04	0,0052	7,80E-05	0,7061	4,90E-04	Rim
4826,62		279	417	UCZ	0,7067	2,57E-04	0,0031	6,71E-05	0,7066	5,14E-04	Core
4826,62		279	416	UCZ	0,7061	2,25E-04	0,0034	6,99E-05	0,7060	4,50E-04	Rim
4826,62		279	415	UCZ	0,7064	2,06E-04	0,0035	6,51E-05	0,7063	4,12E-04	Rim
4826,62		282	418	UCZ	0,7063	2,43E-04	0,0044	6,83E-05	0,7061	4,86E-04	Rim
4826,62		282	419	UCZ	0,7062	2,39E-04	0,0050	6,49E-05	0,7060	4,78E-04	Core
4826,62		282	420	UCZ	0,7068	2,23E-04	0,0037	6,76E-05	0,7067	4,46E-04	Rim
4924,39	TM 1.47	285	398	LCZ	0,7061	4,09E-04	0,0077	2,31E-04	0,7058	8,18E-04	Rim
4924,39		285	399	LCZ	0,7053	3,65E-04	0,0050	1,36E-04	0,7052	7,30E-04	Rim
4924,39		285	397	LCZ	0,7050	4,85E-04	0,0888	1,47E-03	0,7024	9,74E-04	Rim
4924,39		285	500	LCZ	0,7067	3,39E-04	0,0084	1,01E-04	0,7065	6,78E-04	Core
4924,39		287	402	LCZ	0,7059	2,89E-04	0,0023	9,04E-05	0,7058	5,78E-04	Rim
4924,39		287	401	LCZ	0,7059	3,42E-04	0,0028	9,68E-05	0,7058	6,84E-04	Core
4924,39		287	400	LCZ	0,7067	2,97E-04	0,0029	8,29E-05	0,7066	5,94E-04	Rim
4991,09	TM 1.48	288	501	LCZ	0,7048	3,22E-04	0,0006	9,45E-05	0,7048	6,44E-04	Rim
4991,09		288	502	LCZ	0,7058	3,79E-04	0,0111	3,60E-04	0,7054	7,58E-04	Rim
4991,09		289	403	LCZ	0,7043	2,73E-04	0,0013	7,64E-05	0,7043	5,46E-04	Rim
4991,09		289	404	LCZ	0,7051	2,55E-04	0,0007	7,75E-05	0,7051	5,10E-04	Rim
4991,09		289	405	LCZ	0,7051	2,51E-04	0,0021	7,02E-05	0,7051	5,02E-04	Rim